

國立臺灣大學理學院物理學研究所

博士論文

Department of Physics

College of Science

National Taiwan University

Doctoral Dissertation



台大陣列七像素毫米波致冷接收機

A 7-pixel 80-116 GHz Cryogenic Front-end Receiver for
NTU-Array

陳彥麟

Yen-Lin Chen

指導教授：闕志鴻博士

Advisor: Tzihong Chiueh, Ph.D.

中華民國 110 年 1 月

Jan, 2021



國立臺灣大學博士學位論文
口試委員會審定書

台大陣列七像素毫米波致冷接收機
A 7-pixel 80-116 GHz Cryogenic Front-end Receiver
for NTU-Array

本論文係陳彥麟君 (D97222008) 在國立臺灣大學物理學系完成之博士學位論文，於民國 110 年 1 月 26 日承下列考試委員審查通過及口試及格，特此證明

口試委員：

關志遠

王明杰

胡樹霖

朱國瑞

賴詩萍

所長：





誌謝

能完成這本論文受到許多人的幫助。首先要感謝我的指導教授關志鴻老師，謝謝您的悉心教導，讓我可以一步步建立起這個天文接收機。儘管花了許多時間，這個艱辛的過程和經驗仍是無可取代的。感謝王明杰老師、朱國瑞老師、胡樹一老師、賴詩萍老師給我的論文提出了犀利寶貴的意見。感謝瞿大雄老師、蕭宇劭博士、章朝盛博士、牛道智博士、林凱揚博士在我量測上的協助與建議。感謝陳志良先生、齊場和夫先生、黃輝明先生、黃清化先生在我加工上的幫忙。感謝姚慧敏小姐、實驗室的同學、我的朋友、我的父母，阿公、與小檀。





摘要

近年因毫米波望遠鏡的接收器靈敏度逐漸接近量子極限，前級接收機的研究以寬頻、廣角、與能觀測天文極化為主。尤其是多像素 (multi-pixel)，這種將幾十甚至幾百顆接收器放置在一起以增加接收面積的方法，能大幅加快毫米波望遠鏡的巡天速度。配備多像素接收機的干涉陣列將能同時達成高空間解析度與廣角觀測。因此，我們設計了一座寬頻 (80-116GHz)、能觀測天文極化 (dual-polarization) 的七像素前級接收機。在接收機裡，墊片極化器 (septum polarizer) 的頻寬被提升到了 42% (77-118 GHz)，是以往的兩倍以上。極化器量測顯示其 Stokes I/Q Leakage 在 2% 以內，Stokes Q/U Leakage 在 1% 以內。因墊片極化器比正交極化轉換器 (orthomode transducer) 適合觀測線型極化，配備墊片極化器的天文望遠鏡將更具優勢。同時我們也設計了一個有 40 dB 增益的 75-110 GHz 低噪音放大器，以及有 15 dB 隔離度的法拉第隔離器。最後我們針對十九像素接收機及其光學元件做了詳細的熱學計算。此論文討論了建立多像素接收機的各项細節，以為將來毫米波陣列的巡天觀測做準備。





Abstract

While the current detectors in millimeter/sub-millimeter telescopes reach the quantum noise level, wide-band polarization measurement and fast mapping provide advantages. A telescope equipped with multi-pixel feeds directly increases its survey efficiency. We have developed a 7-pixel, coherent, wide-band (80-116 GHz), and polarization-capable front-end receiver, aiming for astrophysical observations. The critical receiver components include the septum polarizer and low noise amplifiers. The septum polarizer reported a 42% bandwidth without any resonances, at least twice as wide as the previous polarizer's bandwidth. Polarizer measurements show that I to Q/U leakage is below $\pm 2\%$ and the Q-U mutual leakage is below $\pm 1\%$. A single low noise amplifier provides a high gain of 40dB in 75-110GHz. We also estimate the thermal load of the 19-pixel cryostat and the receiver optics.



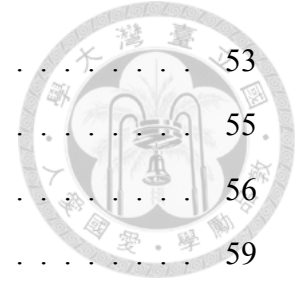


Contents

口試委員會審定書	iii
誌謝	v
摘要	vii
Abstract	ix
1 Introduction	1
1.1 Science	1
1.1.1 SZ-effect Galaxy Cluster Survey	1
1.1.2 CMB Polarization Measurement	2
1.1.3 CO Line and Intensity Mapping	3
1.2 Multi-Pixel Telescopes	3
1.2.1 Examples of the Focal Plane Array	4
1.2.2 Incoherent and Coherent detector	5
1.2.3 Phased array and Interferometer array	6
1.2.4 Multi-pixel Interferometer Array	7
1.3 The Front-end Receiver	8
1.3.1 Instrumental Challenge	9
1.4 NTU-Array	10
1.5 Outline of Thesis	10
2 7-pixel Front-end Receiver	13

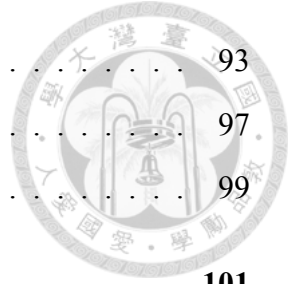


2.1	System Overview	13
2.2	Receiver Optics	15
2.2.1	Dish	15
2.2.2	Off-axis Horn in Multi-pixel Optics	16
2.2.3	Vacuum Window	19
2.2.4	IR Filter	22
2.2.5	Feedhorn	23
2.2.6	Circular Stainless Waveguide	26
2.3	Septum Polarizer	27
2.3.1	Septum Design	27
2.3.2	Polarizer Measurement	31
2.3.3	Measurement A	31
2.3.4	Measurement B	32
2.4	LNA	35
2.4.1	LNA Housing	38
2.4.2	Transition Probe Measurement	40
2.4.3	One-chip LNA Measurement	40
2.4.4	Two-chip LNA measurement	41
2.5	RF Components after LNA	44
2.5.1	Waveguide Bend	44
2.5.2	Stainless Waveguide	46
2.5.3	Faraday rotation Isolator	48
2.5.4	Faraday Rotation Isolator Measurement	49
2.5.5	High-Pass Filter	50
2.5.6	Waveguide Feed through	51
2.5.7	Mixer	51
2.6	Summary	52
3	Discussion of Critical RF Components	53
3.1	Resonance-Free Septum Polarizer	53



3.1.1	History	53
3.1.2	Summary of Historic Review	55
3.1.3	Comparison of Septum Polarizer and OMT	56
3.1.4	Polarization Leakage	59
3.1.5	Result of Polarization Leakage	62
3.1.6	Calibration for removing Stokes I	65
3.1.7	D-band and G-band Results	67
3.2	Discussion of Cryogenic LNA Housing	71
3.2.1	Comparison of Amplifiers and Bolometers	71
3.2.2	Waveguide to Microstrip line Transition	73
3.2.3	Simulation of Transition Probes	75
3.2.4	Silver adhesives	76
3.2.5	Impedance of Wire bonds	77
3.2.6	Simulation of Bond Wires	78
3.2.7	Cryogenic LNA Housing for Receivers	80
3.3	Development of Faraday Rotation Isolator	80
3.3.1	Introduction to Faraday Rotation	80
3.3.2	Dielectric components	82
3.3.3	Higher-mode suppression	83
3.3.4	Simulation of Faraday Rotation Isolator	84
3.3.5	Electrical property at Cryogenic temperature	85
4	Cryogenic	87
4.1	Introduction to Receiver Cryostat	87
4.2	Heat Transfer	88
4.2.1	Introduction	88
4.2.2	Thermal Conduction through Solids	90
4.2.3	Thermal Radiation	91
4.2.4	Heat Transfer in other ways	92
4.3	Thermal Load	93

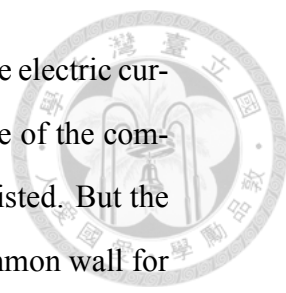
4.3.1	Thermal load of the First Stage	93
4.3.2	Thermal load of the Second Stage	97
4.3.3	Discussion of the Thermal Load	99
5	Conclusion	101
A	Polarization Leakage	103
B	Adhesives operation	107
	Bibliography	109





List of Figures

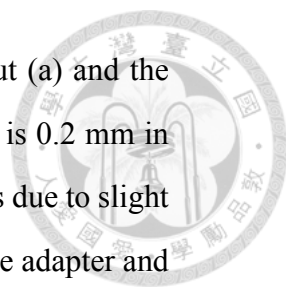
1.1	Schematic of a 19-pixel receiver.	4
1.2	(a) The adding interferometer. (b) The multiplying interferometer.	6
1.3	(a) The phased array (two-pixel). (b) The interferometer array (two-pixel).	7
2.1	The block diagram of the two-element NTU-array.	15
2.2	dish	16
2.3	airy disk	19
2.4	39degree	20
2.5	19degree	20
2.6	0degree	20
2.7	phasecenter	21
2.8	80GHz radiation pattern (45 degrees cut).	24
2.9	80GHz radiation pattern (0 degrees cut).	24
2.10	104GHz radiation pattern (45 degrees cut).	25
2.11	104GHz radiation pattern (0 degrees cut).	25
2.12	<A typical configuration of the stepped septum polarizer in a circular waveguide.>	28



2.13 Field distributions of an E^y input (a) and an E^x input (b). The electric current smoothly circulates in opposite directions on either side of the common wall (septum) for the E^x input as if no septum ever existed. But the current flows in the same direction on either side of the common wall for the E^y input, so that the septum top edge becomes a stagnation point for charge accumulation. Therefore, a virtual TM_{01} mode, which has primarily the radial electric field, is excited. A good septum is able to re-convert the virtual TM_{01} mode back to the TE_{11} mode on its exit to output ports. 28

2.14 Simulation results of the transmission S_{21} and the reflection S_{11} of the fundamental TE_{11} mode, and of the reflected TM_{01} (S_{31}) and TE_{21} (S_{41}) modes, for our optimized septum polarizer. These simulation results are for an ideal polarizer, where the left-right symmetry is obeyed. For the E^y input, the TM_{01} is seen to be well suppressed except near the TM_{01} cutoff frequency 93 GHz. But even near this frequency the suppression is still good at the -14dB level with an insertion loss 0.2dB. Most impressively, this polarizer design has been tuned to eliminate all resonances across the entire W-band and beyond 120 GHz. The even higher-order modes TE_{21} begins to be excited beyond 118GHz for both E^y and E^x inputs, and the transmission S_{21} for the E^y input deteriorates rapidly beyond 120 GHz. 29

2.15 Results of isolation S_{ij} and reflection S_{ii} for measurement A, and results of the simulation with an identical setup as the measurement. The overall agreement between the two is very good. The measured S_{12} turns out to be indistinguishable from the measured S_{21} . 32



2.16 The measurement B and simulation results for the E^x input (a) and the E^y input (b). The rectangular-to-circular transition adapter is 0.2 mm in length. The unexpected resonance at 95 GHz shown in (a) is due to slight axis misalignment of 1.8 degrees at the interface between the adapter and the polarizer. The agreement between measurement and simulation is considerably good; especially the measured resonances are all captured by simulations. Again, we find the measured S_{11} 's for both R and L outputs are almost identical. 34

2.17 LNA I-V curve. 37

2.18 LNA gain and noise measured on wafer. 37

2.19 Picture of a LNA housing. 39

2.20 Measurement of a Alumina B2B probe 42

2.21 Measurement of a one-chip LNA without absorbers. 42

2.22 LNA S11 measurement. 43

2.23 Two-chip LNA measurement without absorbers. 45

2.24 Two-chip LNA measurement added a absorber. 45

2.25 Picture of a stainless waveguide soldering on an aluminum flange. 47

2.26 Measurement of stainless waveguides. 47

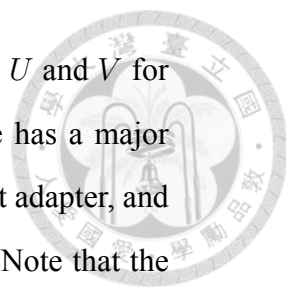
2.27 Measurement of Faraday rotation isolators. 50

3.1 Resonances measured in the septum polarizer. 56

3.2 Waveguide modes of a circular waveguide. 57

3.3 Example of the ortho-mode transducer. 58

3.4 The measured leakage from Stokes I to polarized components, $(\partial\tilde{Q}/\partial I, \partial\tilde{U}/\partial I, \partial\tilde{V}/\partial I)$ for the two modules (a) and (b). The partial differentiations are taken on Eqs. (5.4), (5.5) and (5.6). 63



3.5 The measured leakage among the polarized components Q , U and V for the two modules (a) and (b). The $Q - U$ mutual leakage has a major contribution from the axis misalignment of the measurement adapter, and the resulting phase error has been corrected in this figure. Note that the $V - U$ leakage is a few times larger than others. 64

3.6 Measurement A of 140-220GHz polarizer. 67

3.7 Measurement B(Ex) of 140-220GHz polarizer. 68

3.8 Measurement B(Ey) of 140-220GHz polarizer. 68

3.9 Measurement B(Ex) of 110-170GHz polarizer. 69

3.10 Measurement B(Ey) of 110-170GHz polarizer. 69

3.11 Phase diviation of 110-170GHz polarizer. 70

3.12 Sensitivity comparison of amplifiers and bolometers. 73

3.13 Schematic of the transition probe design. 75

3.14 Schematic of the bond wire. 79

3.15 Schematic of the Faraday rotation isolator. 82

4.1 Schematic of the receiver cryostat. 89

4.2 The thermal load of the first stage. 99

4.3 The thermal load of the second stage. 99

A.1 Leakage of 140-220GHz polarizer. 104

A.2 Mutual leakage of 140-220GHz polarizer. 104

A.3 Leakage of 110-170GHz polarizer. 105

A.4 Mutual leakage of 110-170GHz polarizer. 105

A.5 Phase of 110GHz polarizer. 106

A.6 Phase of 75GHz polarizer. 106

A.7 Phase of 140GHz polarizer. 106



List of Tables

1.1	Examples of Focal Plane Arrays	4
2.1	Dish parameters	17
2.2	Results of Wavefront Analysis	19
2.3	Vacuum window materials	22
2.4	Summay of receiver components	52
3.1	Summary of W-band Polarization Leakage	65
3.2	Summary of D-band Polarization Leakage	71
3.3	Summary of G-band Polarization Leakage	71





Chapter 1

Introduction

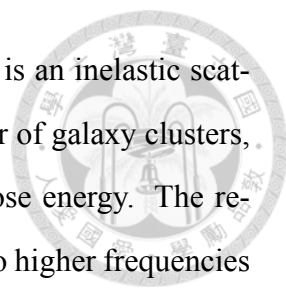
While the current detectors in millimeter/sub-millimeter telescopes are reaching the quantum noise level, wide-band polarization measurement and fast mapping speed provide advantages. A telescope equipped with multi-pixel feeds directly increases its survey efficiency. We have developed a 7-pixel, coherent, wide-band (80-116 GHz), and polarization-capable front-end receiver, aiming for astrophysical observations. Scientific goals include the Sunyaev-Zel'dovich effect (SZ-effect) galaxy cluster survey, the cosmic microwave background (CMB) polarization measurements, and carbon dioxide (CO) spectral line detections.

1.1 Science

1.1.1 SZ-effect Galaxy Cluster Survey

Galaxy clusters are the most massive object in the universe. Measuring the abundance of galaxy clusters as a function of mass and redshift improves current constraints on cosmological parameters, including the equation of state of dark energy and the sum of the neutrino masses [112] [43]. A galaxy cluster has the mass of $10^{14} - 10^{15}$ solar mass, the radius of 2-10 mega parsec (Mpc), and the center temperature of 10^{10} K. Components of a galaxy cluster include 10% baryon and 90% dark matter.

The SZ-effect, X-ray, and weak lensing are widely applied to detect galaxy clusters.

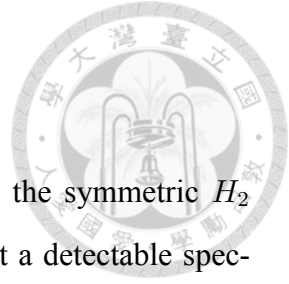


The SZ-effect resulting from the inverse Compton scattering, which is an inelastic scattering of cold CMB photons and the hot electron gas inside the center of galaxy clusters, where the photons gain energy, by several mK, and the electrons lose energy. The reheated photons distort the CMB power spectrum and shift it slightly to higher frequencies [13]. The SZ-effect is redshift (z) independent, compared to the X-ray observation that has $(1 + z)^{-4}$ dependence. The X-ray observation is suffering from the atmospheric absorption and hence used in the space telescope. Moreover, the weak lensing method is applied to detect mostly low- z galaxy clusters [105]. Therefore, the SZ-effect becomes an efficient tool for the ground-based telescopes to survey high- z galaxy cluster candidates.

1.1.2 CMB Polarization Measurement

CMB photons are linearly polarized at a 10% level [98]. In the early universe, photons and electrons are decoupling while the temperature of hot plasma is 3,000K. Then the Thomson scattering occurred at the last-scattering surface, where an elastic scattering of photons and electrons creates the CMB polarization. The CMB polarization patterns can be separated into E-mode and B-mode, depending on their orientation of polarization. E-mode is due to the density perturbation in the early universe, and B-mode is resulting from either gravitational waves from inflation or the gravitational lensing. B-mode detection provides a way to test the inflation theory and imprints of the primordial gravitation wave [47].

DASI detected E-mode at the South Pole in 2002 [61]. For B-mode detections, BICEP2 reported promising signals in 2014 [6]. However, the Planck results shown that galactic foregrounds, specifically dust, account for most or all of the detected B-modes [85]. B-mode is still too weak to be identified and covered by foreground noise. The polarization measurement is facing a challenge on how to determine signals in the early universe or locally [86].



1.1.3 CO Line and Intensity Mapping

The molecular hydrogen gas (H_2) fuels the star formation, but the symmetric H_2 molecule has no permanent dipole moment and hence does not emit a detectable spectral line at radio frequencies. The 21-cm indicates the neutral hydrogen atoms (HI) line, resulting from the transition between two hyperfine levels of the hydrogen 1st ground state. The frequency of the 21-cm line is 1,420 MHz. Mappings from the 21-cm radiation reveal the information of star formation in dusty molecular clouds, where the visible light is difficult to penetrate [64]. However, the 21-cm signal is still too weak while we attempt to observe the star-forming region of high- z galaxies. The detection of CO spectral lines provides another method. CO implies the molecular carbon monoxide gas, which is associated with H_2 in the star-forming region [76] [11]. The frequency of CO 1-0 is 115.34 GHz. An 80-116GHz telescope can determine the star-forming galaxy up to $z = 0.4$ via CO 1-0 detection.

1.2 Multi-Pixel Telescopes

A multi-pixel telescope improves either the mapping speed or the sensitivity. Traditional one-pixel radio telescopes have a receiver at the focal plane and hence obtain a one-pixel image size, depending on the diameter of dishes or the baseline of interferometers. N-pixel telescopes acquire n times of one-pixel image size. The survey speed of n-pixel is increased by a factor of n, making telescopes powerful survey instruments. On the other hand, if the n-pixel are pointing to the same area, the sensitivity of telescopes improves. The ideal of multi-pixel refers to the focal plane array (FPA) that contains an array of receivers at the focus of the optical system. A single-dish telescope equipped with FPAs has advantages such as the multi-band detection, large field of view (FoV), and high sensitivity.

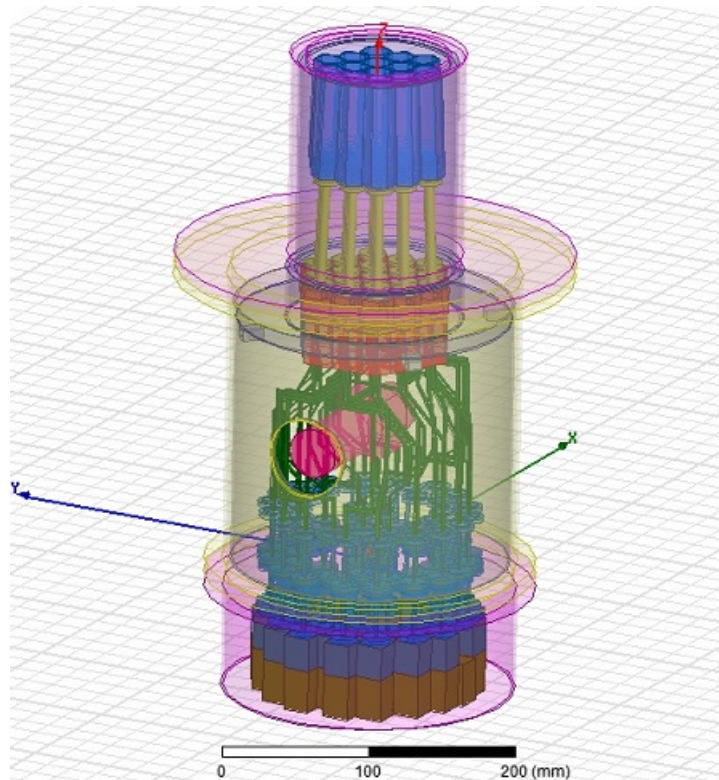


Figure 1.1: Schematic of a 19-pixel receiver.

Table 1.1: Examples of Focal Plane Arrays

Examples of FPAs	Type of Detectors	Type of Telescopes
Multi-beam Array	Coherent	Single-Dish
Bolometer Array	Incoherent	Single-Dish
Phased Array	Coherent	Interferometer (add)
Interferometer Array	Coherent	Interferometer (multiply)

1.2.1 Examples of the Focal Plane Array

Table 1.1 lists examples of the FPA, which contains either incoherent or coherent detector, and installed on the single-dish telescope or the interferometer. A single-dish telescope with one feedhorn has large gain but a small FoV, due to the diffraction limit of its aperture size. A single beam must be pointed to different directions to make a full image. Hence, the purpose of FPAs is to increase the FoV of single-dish telescopes. The first example is the multi-beam feed array, in which an array of feedhorns with physical separations are installed on the focal plane, providing non-overlapping beams. The multi-

beam feed can increase survey speed and maximize antenna efficiency. Equipped with the FPA, it is possible to build a telescope with both excellent spatial resolution and wide FoV [36] [41].

However, a telescope always optimizes the central beam to its focus, and the off-axis beam suffers from optical distortions and tapered optical efficiency. The following two examples are aiming to solve the off-axis issue in distinct ways. One is the bolometer array which employs the incoherent detectors, and the other one is the phased array that modulates the phase of each beam by electronics.

1.2.2 Incoherent and Coherent detector

Compared to the multi-beam array, bolometer arrays have a minor concern with optical degradation. The bolometer array contains a lot of incoherent detectors which directly measure the energy of each photon, instead of the square of electric fields. Hence the bolometer array can reach remarkable sensitivity. Examples include the silicon wafer-based, microwave inductance detectors (MKID) [101] [45]. The incoherent system relies upon synchronous modulation/demodulation of the incident power in front of detectors, but cannot modulate the phase, frequency, incident angle, and intensity of the signal. On the other hand, coherent detectors can measure the electric field, involving the signal phases and their processing, and hence have well control of systematic errors. Bolometer arrays are currently the essential CMB experiments, and also applied to infrared, optical, X-ray, and gamma-ray detectors.

The second method for solving the off-axis issue is the phased array, which consists of close-spaced antenna elements, recording an incident plane wave in different locations, and then modulate its phase using electronics [110] [99] [92]. This modulation method named the post-correlation beamforming. The electronic is a beamformer that constructively adds the phase of output signals and aligns each off-axis beam to coherent beams. The phased array is equivalent to the interferometer using addition, and can be regarded as a single-dish telescope with missing metals but having more coherent beams. In comparison, the interferometer array is using multiplication. In the next section, we compare

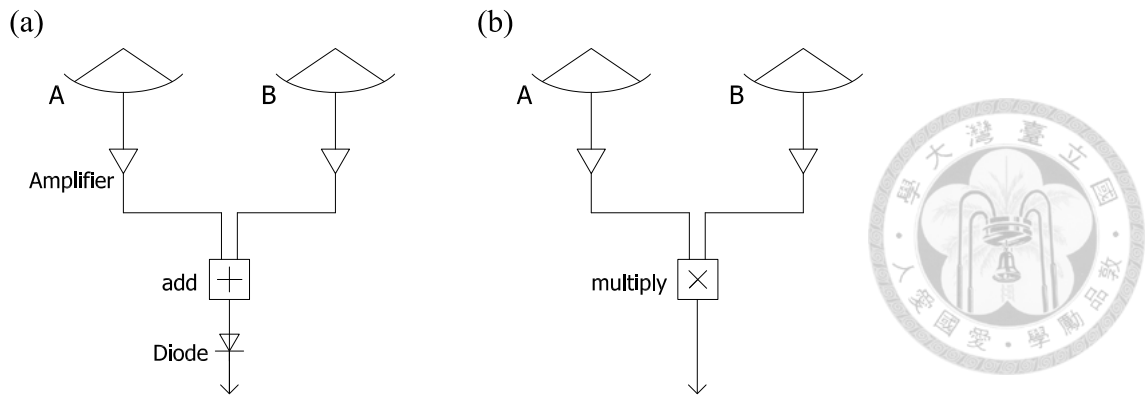


Figure 1.2: (a) The adding interferometer. (b) The multiplying interferometer.

these two examples of FPA.

1.2.3 Phased array and Interferometer array

Figure 1.2 illustrates the comparison of adding and multiplying interferometers. If there are two antenna elements, A and B , then S_A and S_B denoted the voltage of signals at each antenna. N_A and N_B denoted the voltage of receiver noise, including background noise, antenna noise, and amplifier noise. We assume the gain of amplifiers is unity. For the adding interferometer, the output after diodes is $((S_A + N_A) + (S_B + N_B))^2$, the square of output electric voltage. Because the time-averaged value of uncorrelated quantities tends to zero, the result is $\langle S_A^2 \rangle + \langle S_B^2 \rangle + \langle N_A^2 \rangle + \langle N_B^2 \rangle + 2\langle (S_A S_B)^2 \rangle$, $\langle \dots \rangle$ denotes the time average. The receiver noise thus affects the output of adding interferometers. On the contrary, the output of the multiplying interferometer is $(S_A + N_A)(S_B + N_B)$. After the time-averaged multiplication, known as the correlation, the result is only $\langle S_A S_B \rangle$, independent from the noise contribution [29]. (However, by observing a time-varying source or adding a phase modulator, an adding interferometer can further distinguish the receiver noise.)

We further compare the multiplying interferometer with the single-dish telescope. The single dish has a high spatial frequency cut-off, defined by its diameter. In comparison, the multiplying interferometer has a low spatial frequency cut-off set by its minimum antenna separation. The single-dish telescope is hence suitable for observing large-scale structures. But, equipped with a multi-pixel feed, the interferometer can have more advantage of the

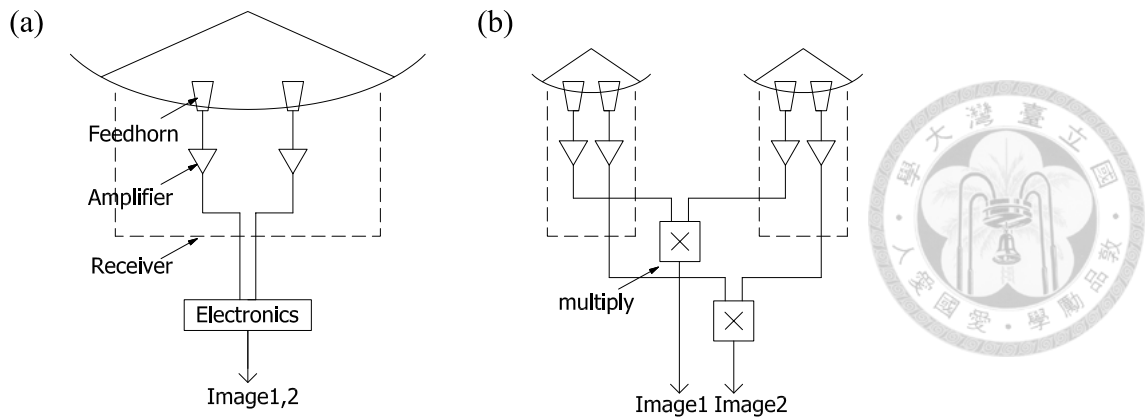


Figure 1.3: (a) The phased array (two-pixel). (b) The interferometer array (two-pixel).

sky survey.

The interferometer array is the fourth example of FPAs that has excellent spatial resolution due to long base-line, and thus distinct from the single-dish telescope. Without the beam former or phase modulators, off-axis beams in interferometer arrays suffer from optical degradation. However, interferometer arrays using multiplication can eliminate the contribution from the receiver noise and the background noise, making them better than the phased array using addition.

1.2.4 Multi-pixel Interferometer Array

Figure 1.3 illustrates the schematic of a two-pixel phased array and a two-pixel interferometer array with one receiver pair. The two-pixel phased array equipped with two feedhorns on a single-dish telescope and the backend electronics employs the beamforming. The two-pixel interferometer array has tens of receiver pairs, in which each receiver has two feedhorns. Traditional interferometer arrays construct a one-pixel image from the correlated fringe pattern of each receiver pair. For example, ALMA provides excellent u-v coverage, wide-band, and sensitive observation. However, it is still a one-pixel telescope and requiring more integration time to perform the sky survey.

Though the implementation of multi-pixel interferometer arrays looks straightforward, it is still challenging due to instrumental issues. For example, the receiver components require smaller size and compactness to allow more feed horns in the focal plane. The cryogenic systems need sufficient cooling power for the multi-pixel telescope that contains

more active devices and amplifiers. The design of back-end electronics is more critical due to a lot of signal outputs, bias circuits, connectors, and wires. Moreover, practical problems such as the cartridge, storage, communication, and funds increase the difficulty. In recent years, several instruments such as the intensive integrated feed horns [32], the high cooling power refrigerator systems [54], and the multi-layer routing PCB design [99] are developed to solve instrumental issues.

In conclusion, the bolometer array and the phased array contain more pixels, but the former uses incoherent detectors, and the latter is affected by the receiver noise. The interferometer array suffers from off-axis degradation but has well-controlled system noise. In this thesis, we develop a 7-pixel front-end receiver for the interferometer array with one receiver pair. Note that the close-integrated feedhorns do not correlate to each other.

1.3 The Front-end Receiver

Receivers control the system noise temperature of radio telescopes. In millimeter-wave observations, signals from radio sources are very weak and covered by unwanted noises, such as dust emission in the foreground dust and the infrared radiation from the surroundings. The output power consists of signal power and noise power. A sensitive front-end receiver is required to maintain the receiver noise as low as possible and give a pre-amplification of 20-40 dB. Therefore, the low noise amplifier in radio-band (RF LNA) is an essential device, which provides the pre-amplification and determines the receiver noise.

For example, while the weak astrophysical signal with 10Jy is detected by a 100GHz telescope with 30GHz bandwidth, from the antenna temperature equation [22]

$$W = \int A(\theta, \phi) B(\theta, \phi) d\Omega df \simeq A_0 \Delta f S_0 \quad (1.1)$$

W , A_0 , Δf , and S_0 denoted the input power, the effective aperture area, the bandwidth, and the flux density, respectively. Equation 1.1 indicates that an antenna system with an aperture area converts the flux density into the total input power. Thus, an antenna

with 1.2m diameter obtains the signal power around 10^{-15} W, 10^{-3} K level, which is still too weak to be measured by the electronics, especially in the noisy environment. Hence, the front-end receiver requires cryogenic cooling to eliminate 300K noisy surroundings. A series of active devices, such as LNAs, Mixers, and the back-end systems provide amplifications until the signal power is reaching 10^{-3} W level. The total amplification will be 120dB.

Sensitivity is another essential issue for telescopes. From the radiometer equation:

$$\Delta T_{min} = \frac{T_{sys}}{\sqrt{N\beta\tau}} \quad (1.2)$$

T_{sys} means the system noise temperature, β means the bandwidth, and τ means the integration time. N indicates the number of identical elements or detectors. If there is a one-pixel, single-polarization interferometer array with n antennas, the number of receiver pairs is $n(n-1)/2$, and hence $N = n(n-1)/2$. If the array has dual-polarization, $N = n(n-1)$. ΔT_{min} gives the fluctuation of the root-mean-square (rms) output power, the sensitivity of a telescope, which means the minimum detectable signal in the integration time. For example, a cooled 100GHz front-end receiver provides a noise temperature of 110K. If the bandwidth is 36GHz, the number of polarization is 2, and integration time is 3600s, the resulting sensitivity is about 6.8 uK, suitable for the signal power of mK level.

1.3.1 Instrumental Challenge

From equation (1.2), an extremely sensitive telescope can be achieved by either increasing bandwidth, number of identical elements, integration time, or reducing the system noise temperature. Therefore, studies of the front-end receiver have focused on the wide-bandwidth, low-noise, and dual-polarization. First, critical active devices such as the LNA limits the bandwidth of receivers. An LNA requires a compromise between the impedance match of the gain and noise, in which the response has to be flat and stable. Hence, it is challenging to design an LNA covered wide-bandwidth. Furthermore, the bandwidth of the back-end system is narrow compared to the receivers. For exam-

ple, ALMA correlator provides the bandwidth of 8GHz per antenna in both polarizations, compared to the optical and RF components that have relatively wide-bandwidth, such as a standard WR10 waveguide providing the bandwidth of 35GHz.

Second, the noise performance of active devices in the first place determines the receiver noise temperature, and the passive devices put ahead of the LNA must be almost lossless. Third, millimeter/sub-millimeter telescopes are capable of measuring polarization by equipping with either septum polarizers or ortho-mode transducers (OMT).

Recently, the bandwidth of receivers and the LNA are both improved. For example, ALMA is building a band 2+3 receiver covered 67-116 GHz [117]. The advanced LNA applied the 35nm gate InP HEMT technologies reaches the noise temperature of 20K at 84GHz [17]. The amplifier-based detectors are always competing with the bolometers that have extremely low noise. The choice of these two distinct detectors determines the type of telescopes. We will discuss the concern in section 3.2.

1.4 NTU-Array

The initial stage of the NTU-array operated in 78-113 GHz consists of six dishes with a diameter of 0.6 m. In 2008, the NTU-Array detected the first light with single-polarization, which is the interference fringe from the passing of Jupiter. In 2010, the NTU-Array moved to Nevada, where the dry atmosphere helps radio-band observations. Meanwhile, two critical instruments are both upgraded, including the prototype of a 1-bit digital spectrometer for the spectral line detections, published in 2015 [107], and the 7-pixel front-end receiver aiming for fast mapping. This thesis focus on the 7-pixel receiver.

1.5 Outline of Thesis

This thesis is organized as follows. Chapter 2 introduces the NTU-array receiver system, the receiver optics, and RF components. Chapter 3 contains details of three critical instruments: the septum polarizer, LNAs, and isolators. The polarization leakage is given here. Chapter 4 introduces the receiver cryostat. The thermal load calculation of receivers

is provided here, including the loading of receiver optics. Chapter 5 is the conclusion.







Chapter 2

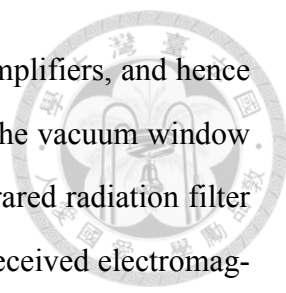
7-pixel Front-end Receiver

In this chapter, we discuss the design of a 7-pixel front-end receiver. Section 2.1 gives the overview of NTU-array system. Section 2.2 provides the receiver with optics, including dishes, windows, infrared radiation filters, and feedhorns. Notably, in section 2.2.5, we discuss the result of multi-pixel optics and the off-axis problem, from the ray-tracing simulation. The septum polarizer and the LNA are presented in 2.3 and 2.4. In section 2.5, we give receiver components behind LNAs, including waveguide bends, stainless waveguides, isolators, high-pass filters, feed-throughs, and mixers. Here we refer the front-end to the position closed to optics, and the back-end closed to the control rooms.

2.1 System Overview

Figure 2.1 illustrates the block diagram of the two-element NTU-array. Each element includes the antenna system, the front-end receiver, the IF/LO system, and the back-end system. To test the prototype of a multi-pixel receiver, NTU-array is designed as a simple two-element system, giving one receiver pair. We can further increase receiver pairs by adding more identical elements for future upgrades.

The antenna system, based on the Cassegrain reflector design, has a primary dish and a secondary dish. The diameter of a primary dish is 1.2m, and the diameter of a secondary dish is 0.18m. Dishes collect the incoming light and transmit it into the front-end receiver. The 19 feedhorns compactly installed in the receiver will provide 19-pixel dual-



polarization images. Currently, only seven feedhorns have the pre-amplifiers, and hence the two-element NTU-array is 7-pixel. On the top of the receiver, the vacuum window separates cold components under vacuum from ambient air. The infrared radiation filter (IR filter) rejects unwanted IR radiations. Feedhorns transform the received electromagnetic (EM) radiation from spherical waves to waveguide modes. Behind feedhorns, the septum polarizer separates the EM wave into right-hand polarization (RHP) and left-hand polarization (LHP), and the 1st LNAs, which has 40dB gain in 75-116GHz, providing the pre-amplification. The Faraday rotation isolator put behind LNAs transmits the amplified signals and forbids reflections from the back-end. The high-pass filter dissipates signals below 80GHz. Therefore, the frequencies of the receiver output are 80-116GHz. The front-end receiver requires two-stage cryogenic cooling, in which the first stage is 70K, and the second stage is 20K.

The IF/LO system employs the Heterodyne process, in which the mixer combines the local oscillator frequency (LO) and radio-band signals (RF), and then down-converts RF to the intermediate frequencies (IF). Based on a LO frequency fixed at 80GHz, the mixer transfers the 80-116GHz signal to the IF band, ranging from direct current (DC) to 36GHz. Subsequently, the second down-conversion, provided by power dividers, filters, mixers, and IF LNAs, separates the IF band into four sub-bands. For dual-polarizations, each pixel generates eight sub-bands in the IF module, and each sub-band has the identical bandwidth of DC to 9GHz. The equalizer compensates the IF spectrum slope, which is usually tiled down toward high frequencies, due to the cable loss. After the IF/LO system, the optical transmitter/receiver module and long optical fibers of 50m transmit IF signals to the control room.

The back-end system includes the analog to digital converter (ADC) and the one-bit digital correlator. The ADC measures the time-varying voltage of analog IF sub-band signals and converts it to digital numbers. Due to Nyquist sampling, the bandwidth of ADCs requires 18GHz. The ultra-wide bandwidth is accomplished by two interleaved ADC boards with different clock delays. One board has zero delays, and the other board has 55.5ps clock delays ($0.5 \times 9GHz^{-1} = 55.5ps$). Both boards provide one-bit sam-

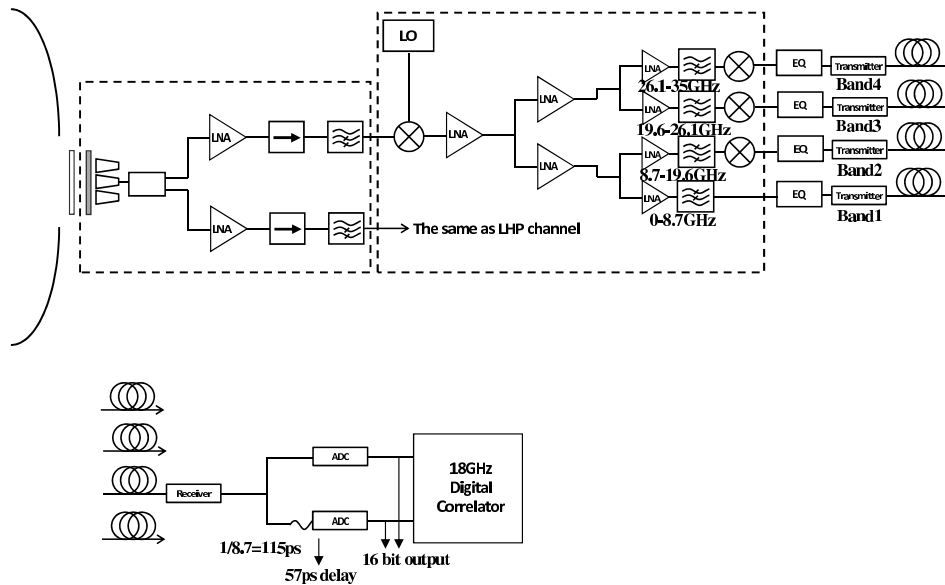


Figure 2.1: The block diagram of the two-element NTU-array.

pling in 9 gigabits per second (Gbps), and hence the interleaving technique combines them to 18Gbps sampling rate. The digitized signal is fed into the digital correlator. The 18Gbps one-bit digital correlator, applied the Field Programmable Gate Arrays (FPGAs), provides the time-averaged correlation of receiver pairs. For each IF sub-band, it requires six Fourier Transform (FT) boards, four correlation boards, and one clock board. The IF/LO system, optical link modules, ADCs, and the digital correlator are implemented by Hsiao-Feng Teng [106], Jing-Cheng Wu, Huan-Hsin Li, and Shing-Kwong Wong [116], respectively.

2.2 Receiver Optics

2.2.1 Dish

Figure 2.2 shows the antenna optics. A primary dish that has a parabolic concave shape brings the parallel rays of light to its focus. A secondary dish, with a hyperbolic convex shape and a smaller size than the primary, reflects the rays again toward the focal

point of telescopes. The hyperbolic convex shape has two focus, one coincides with the focus of the primary dish, and the other is at the telescope focal point. Moreover, the secondary dish increases the effective focal length, revealing the telephoto lens effect. There is a small hole placed at the center of the primary dish, and hence the focal point can be put behind the primary dish. These two dishes constitute the Cassegrain reflector. The reflector design sacrifices a few collecting areas due to the secondary dish, but allows the receiver mounted directly near the dish, therefore, has the minimum optical loss [37] [38].

Table 2.1 lists the information of the NTU-array dishes. These dishes are made of carbon fiber composites to reduce weight, and the reflector surface is coated with aluminum, in which the thickness is ten times a skin depth of aluminum, for ensuring $< 1\%$ reflection loss. To obtain antenna efficiency > 0.95 , the surface accuracy of dishes requires at least $50\mu\text{m}$, which is the root-mean-square of $\lambda/64$ [84].

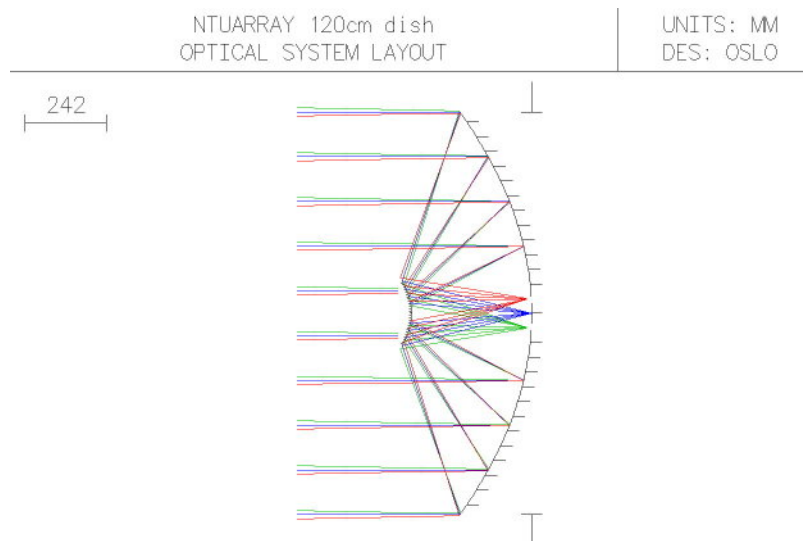


Figure 2.2: dish

2.2.2 Off-axis Horn in Multi-pixel Optics

The multi-pixel optics is suffered from the off-axis problem, where the off-axis feed horn obtains phase deviated signals. For this concern, we apply a ray-tracing simulator, named Optics Software for Layout and Optimization (OSLO), to simulate the optical sys-

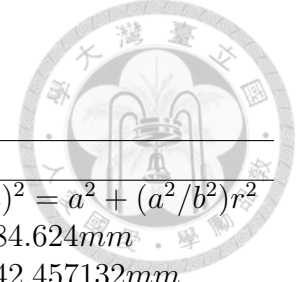


Table 2.1: Dish parameters

Primary dish		Secondary dish	
Equation	$z = r^2/4Fp$	Equation	$(z + a)^2 = a^2 + (a^2/b^2)r^2$
Diameter	$Dp = 1152.0mm$	Diameter	$d = 184.624mm$
Focal length	$Fp = 403.2mm$	Equation parameters	$a = 142.457132mm$ $b = 142.648258mm$
Primary f/ratio	$Fp/Dp = 0.35$	Final effective f/ raio	2.036087

tem. The optical results include the wavefront analysis and the spot diagram. The phase center is determined from the EM simulator.

In figure 2.2(a), the parallel rays of light, with different incident angles related to the primary dish's axis, are put in the dish optics. For the incident angle of 0 degrees, the dishes reflect light to the primary dish's center, the focus, where the feed horn is placed. More importantly, the focus must coincide with the phase center of the feed horn. Now we install 19 feed horns in the dish. The central horn is at the dish's focus, and the outer 18 horns will be off-axis. Each off-axis position is corresponding to different incident angles of rays. For instance, the five horns on the max cross-section line in the 19 horns array, in which the central, second, and third horn are related 0, 0.273, and 0.39 incident degrees. To get the minimum deviated phase, we move off-axis horns to each off-axis focus, and if the phase difference is tiny, the off-axis horn still works.

First, we employ the wavefront analysis in OSLO To find the off-axis focus. In figure 2.3, the color circle depicts the projected wavefront on the image plane, and a central small blank area means that the secondary dish blocks light. The analysis assumes a planar wavefront formed by spherical waves radiated from a far point source. While the wavefront transmits through optical mediums with different refractive indices, the mediums alter the light in the three-dimensional space. Hence, the wavefront analysis measures the optical aberration due to an imperfect lens. The P-V value, which implies the phase difference from the peak to valley, is in the unit of a working wavelength, 3mm. The zero of P-V value means an entirely planar wavefront.

Hereafter, we shift the image plane through the direction parallel to the primary dish's axis to find a minimum P-V value. The result shows that the 0 degrees require a small

displacement of 0.168mm, and P-V is only 0.00072, implying 0.07% of 3mm. The positive value means the direction toward the secondary dish. We define the criteria of phase deviation is 1.5%, which is the same as the surface accuracy of dishes, $\lambda/64$. Table 2.2 shows the summary of the analysis. In the worst case, 0.39 degrees requires -1.53mm displacement, where the phase difference is 1.4%, below the 1.5% criteria.

Second, for checking the diffraction limit of the off-axis focus, the spot diagram is used. In the figure, the black circle implies the first minimum of the point spread function, the Airy disk, where the radius is $r = 1.22(\lambda f/D)$ for a circular aperture. The spot diagram depicts the point distribution resulting from all the rays plotted on a finite region of the image plane, indicating how well the optics bring lights to the focus. If the spots are inside the circle, we consider the optics is under the diffraction limit. Here all the values are in the unit of mm. The effective f/D of a 1.2m dish is 2.036, and the radius of the Airy disk is therefore 7.456mm. The spot spreading size is 0.04938mm, which includes rays from an incident angle below 0.5 degrees. We conclude that the off-axis optics is far below the diffraction limit.

Finally, a 3D electromagnetic simulation software, the Ansoft High Frequency Structure Simulator (HFSS), is applied to verify the phase center in a feed horn. The figure shows the simulation of feed horns. While the wavefront of electric fields is concentrated to one point, the phase center is thus determined. The distance from the phase center to the horn output is 4mm. Furthermore, we tilt off-axis horns with a small angle, according to the primary dish's curvature. Each horn is facing the incoming light, and therefore the sensitivity is enhanced.

We summarize the optics results. The position of off-axis horns is decided from the wavefront analysis, where the phase difference is minimal. The spot diagram shows the off-axis focus is below the diffraction limit. The HFSS simulation gives the phase center of horns. All of these results imply that the off-axis issue in the 19-pixel design is very safe.

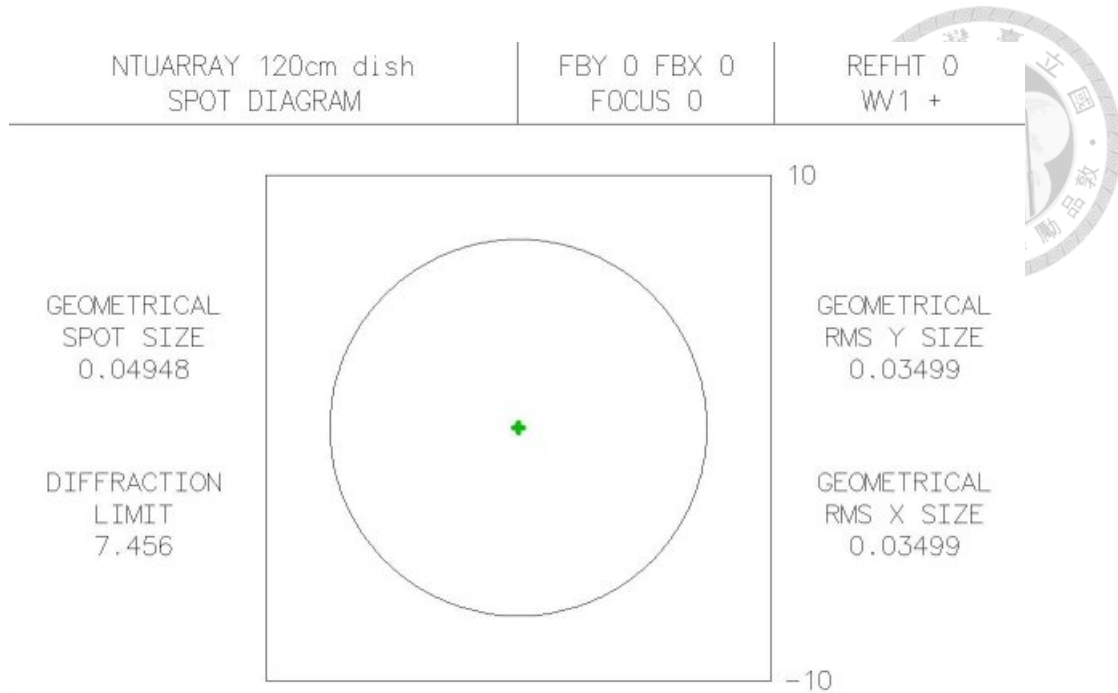


Figure 2.3: airy disk

Table 2.2: Results of Wavefront Analysis

Horn	Incident angle	Horn displacement (mm)	Phase difference (a wavelength)
Center	0 degrees	+0.168	0.07%
First circle	0.19 degrees	-0.18	0.63%
Second circle	0.39 degrees	-1.53 to -1.56	1.4%

2.2.3 Vacuum Window

The vacuum window maintains the vacuum of cryogenic chambers and provides maximum transmission for in-band radiation. Thus, materials of the vacuum window require low dielectric losses and robustness. Table 2.3 lists examples of window materials, including z-cut quartz [60] [59], high-density polyethylene (HDPE) [48], and Zotefoam [93]. The loss tangent ($\tan\delta$) determines the dissipation factor of materials. The refractive index (n) means the wave impedance of EM waves in a non-conductive medium, where $n = (\epsilon\mu/\epsilon_0\mu_0)^{1/2} = (\epsilon_r)^{1/2}$, assumed $\mu = \mu_0 = 1$. The thermal conductivity (k) is related to the heat conduction and the thermal gradient in a cooled window. A window, made of high refractive index materials, is unmatched to air; therefore, a single-layer

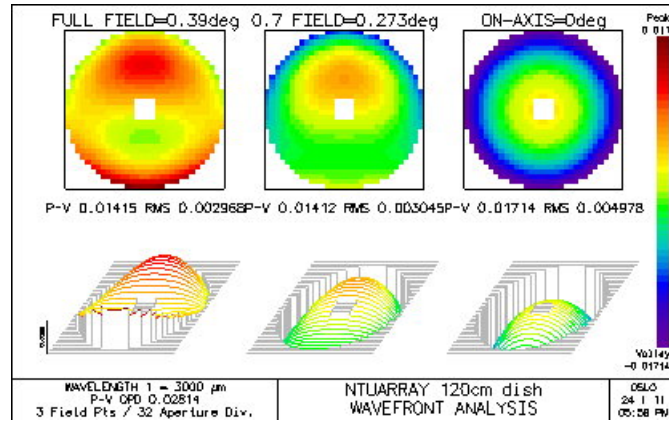


Figure 2.4: 39degree

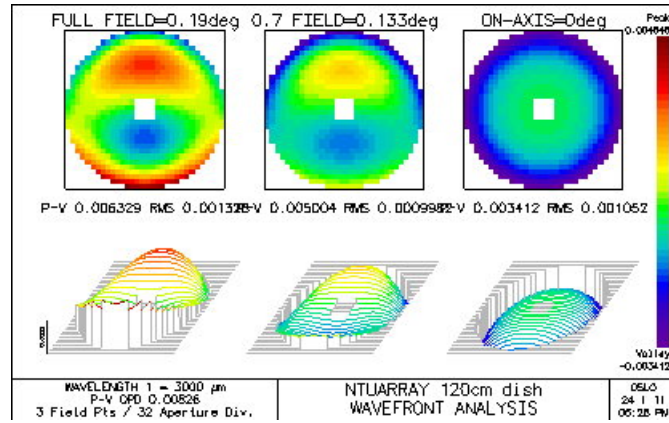


Figure 2.5: 19degree

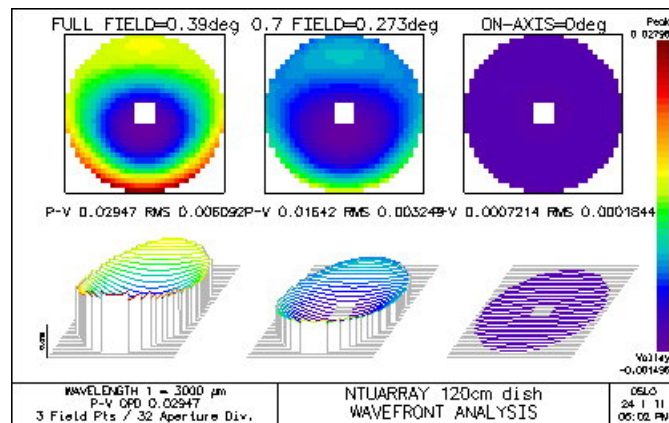


Figure 2.6: 0degree

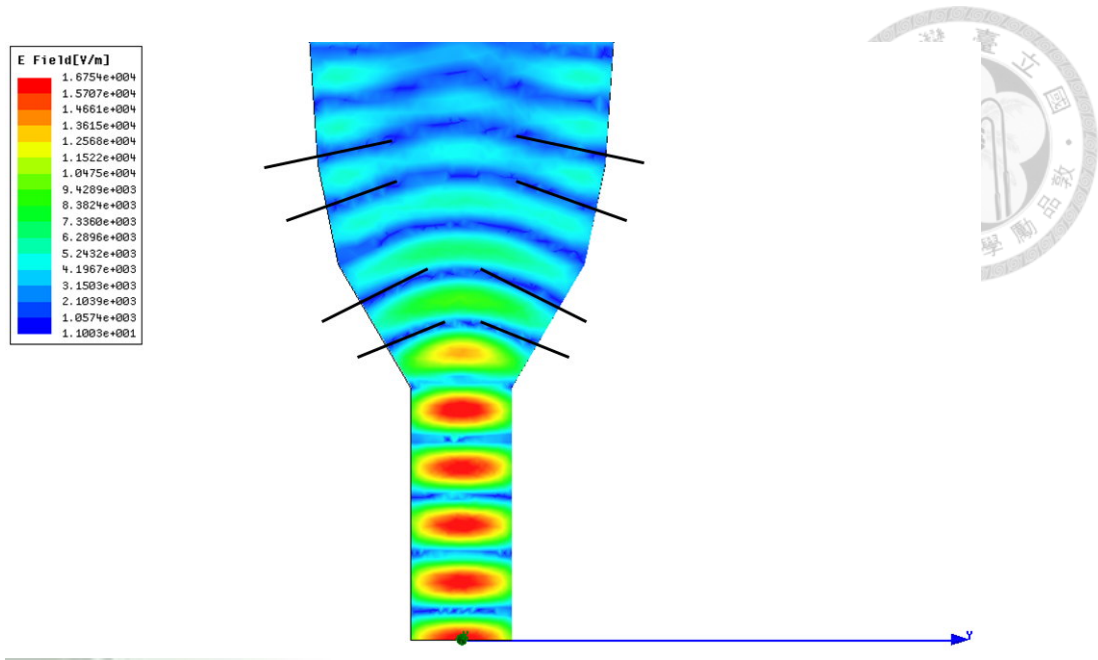


Figure 2.7: phasecenter

anti-reflection (AR) film coated on both sides of the window minimizes the reflections. From the multi-layer calculation in electrodynamics, which gives the single-layer coating condition:

$$n_{AR}^2 = n_{air} \times n_{window} \quad (2.1)$$

Where n_i demotes the refractive index of the material i . The thickness of the window is $n\lambda/2$, and the thickness of a film is $n\lambda/4$, where n is an integer of 1, 2, ..., and λ is the wavelength in windows [53].

The z-cut quartz is the traditional window material that is low-loss and rigid but highly refractive ($n=2.1$), indicating the AR coating is necessary. However, the large-diameter window made of quartz is usually having a gas leak problem and hence applied to small-aperture telescopes. The materials developed for large-aperture windows include HDPE and Zotefoam. The HDPE window, adopted in BICEP3 and QUIET [77], still needs the AR coating, but it has very high tensile strength. For instance, employed the ultra-high molecular weight polyethylene (HMPE), a material similar to HDPE but has a high molecular weight and a high degree of molecular chain alignment, the HMPE window can achieve 27 inches in diameter, with only 0.05 inches in thickness [10].

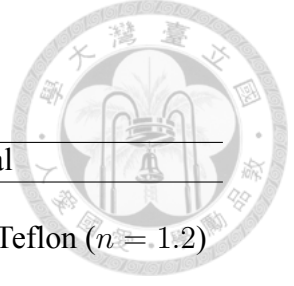


Table 2.3: Vacuum window materials

Window material	$\tan\delta$	n	k	AR coating material
Quartz	1.0×10^{-4}	2.1	1	Teflon ($n = 1.45$)
HDPE	2.5×10^{-4}	1.52	1	Zitex or expanded Teflon ($n = 1.2$)
Zotefoam	$\sim 2.5 \times 10^{-4}$	~ 1	1	none

The Zotefoam HD30, a polypropylene-based foam expanded with nitrogen gas (N_2), is used in ACBAR, BICEP2, Polarbear-1, and SPT [80] [51]. HD30 and its previous version, PPA-30, have very high transparency in mm-wave and low thermal conductivity. Moreover, HDPE has a near-unity of the refractive index, and hence there is no need for AR-coatings. However, the low modulus of elasticity and strength of the Zotefoam window will bend under pressure, limiting its diameter, and the thicker window gives more attenuation. For instance, the Polarbear-2 receiver uses laminated HD-30 with 500 mm in diameter and 200 mm in thickness [51]. Since NTU-array is not a very large-aperture telescope, we apply the HD30 window with 119mm in diameter and 17mm in thickness.

2.2.4 IR Filter

Detectors obtain not only the in-band photon loading but the infrared (IR) loading, which is from the sky, environments, and warm optical elements. Examples of warm optics include the vacuum window, lenses, and telescope structures. The IR noise power reduces the sensitivity of detectors, and it also contributes thermal radiation to the cold head, degrading the cryogenic efficiency. For telescopes that aim for extremely low noise, each cryogenic stage in receivers requires IR filters installed.

The IR filter design is similar to vacuum windows but has multilayer metal-meshes embedded in the dielectric to reject unwanted radiation, whereas the dielectric allows the in-band transmission. The metal-mesh has peculiar patterns, such as the inductive, capacitive, or resonant pattern, which provide high-pass, low-pass, and band-pass filtering. The position of the IR filter is in a vacuum, just above the feedhorns. Hence, there is no need to consider the strength of dielectrics [7] [5]. However, the IR filter is heated during

the infrared radiation, and it will become a new noise source if the heat conduction of dielectrics is too low [52].

We employ a quartz circular plate as the dielectric of IR filters. The diameter is 101.6mm (4 inches), and the plate's thickness is 3mm, two times a wavelength in quartz. From the EM simulation, the in-band transmission is >95%. The gold layers of metal meshes plated on both sides of the quartz, in which the cutoff frequency is 4THz to reject the near-IR radiation. The LDPE films with $\epsilon = 1.7-2.0$, attached on gold layers for anti-reflection.

2.2.5 Feedhorn

The smooth-wall feedhorn based on Potter horn design has three changing flare angles, which transfer incoming spherical wave to the TE_{11} circular waveguide modes [67] [40]. In comparison, the corrugated horns are traditionally applied to cm to sub-mm telescopes. A corrugated feedhorn contains many grooves azimuthally along with its interiors, and each groove depth is about a quarter-wavelength [39]. Though the corrugated feedhorn has excellent performance, it requires the electroforming process, which is time-consuming and high cost (another way is using many metal plates [16]). The Potter horn thus provides an alternative option to the corrugated feedhorn [87]. With a high-speed steel machine tool, It is simple to fabricate and duplicate the smooth-wall structure of feedhorns. In particular, the smooth-wall feedhorn is suitable for the multi-pixel telescope that demands lots of feedhorns.

We apply the Leech's 230GHz horn design [67] and scale it to 100GHz version, with modifications for the angle of edge taper. Typically, a feedhorn aims to receive total radiations from dishes, and hence its taper at the beam angle are corresponding to the edge of the reflector or illuminated targets. The normalized radiated power at tapers is defined in between -10dB and -18dB, depending on each antenna. If we apply a higher taper edge, such as -3dB, the rest beam angles will obtain more surrounding noise. On the other hand, -18dB taper can cover most of the reflector angle and avoid surroundings; however, the lower gain at edges will reduce the received power. Since our dish design is the same as

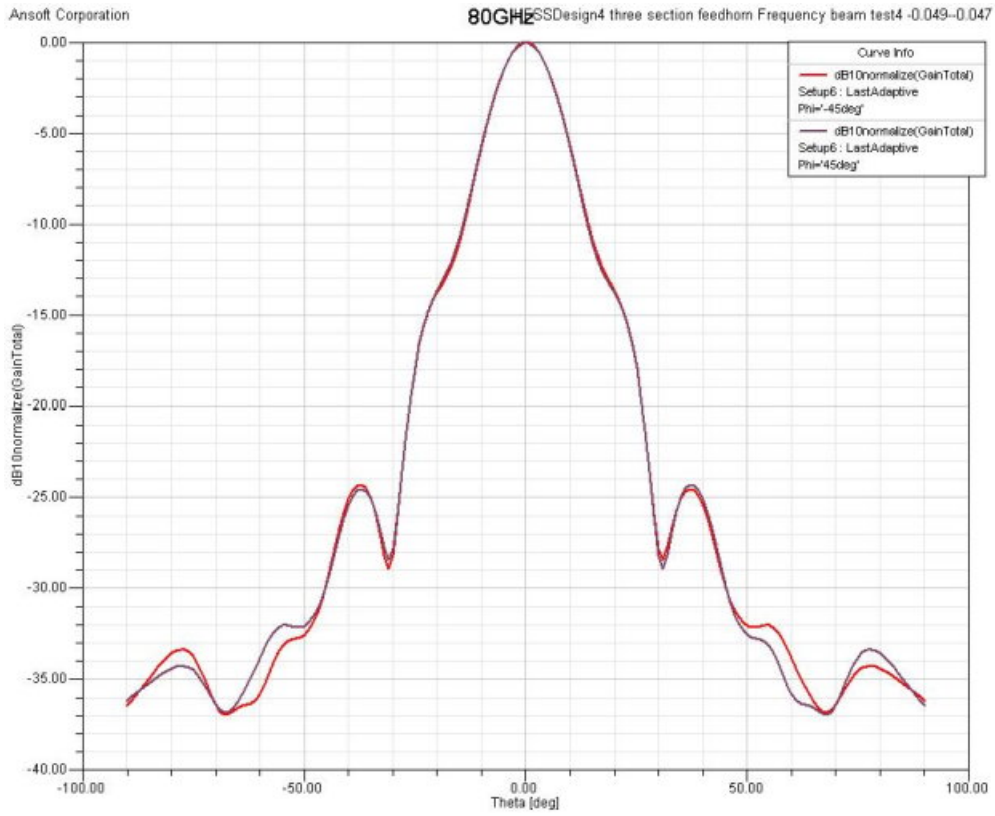


Figure 2.8: 80GHz radiation pattern (45 degrees cut).

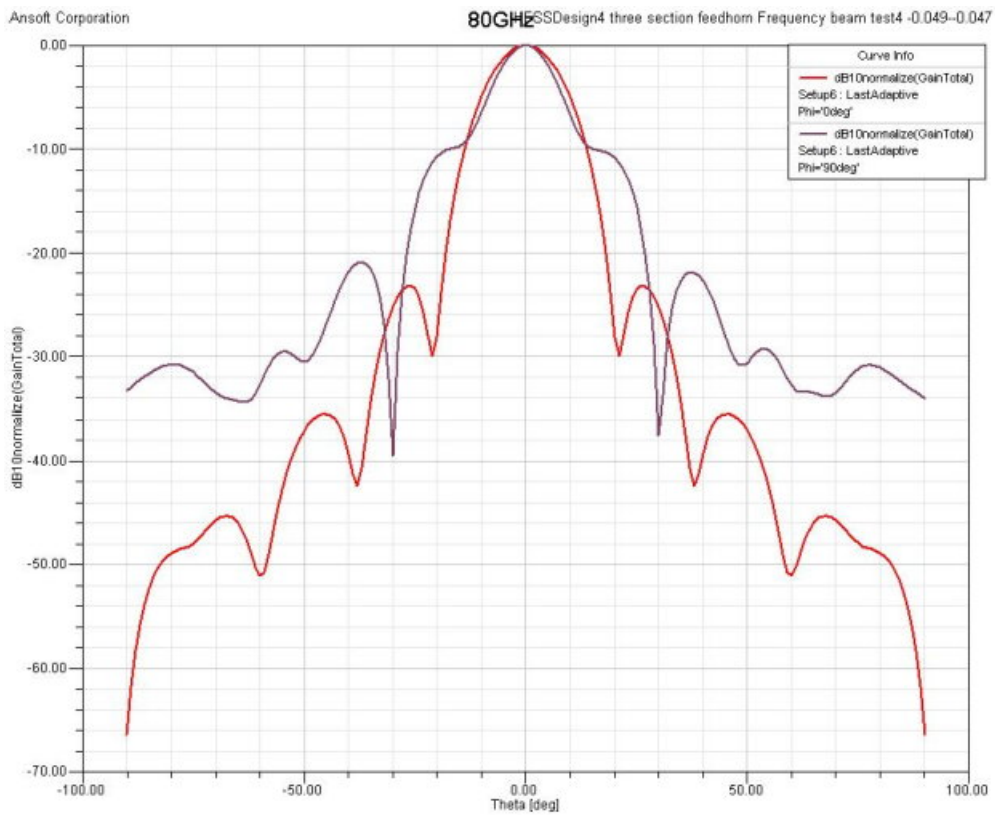


Figure 2.9: 80GHz radiation pattern (0 degrees cut).

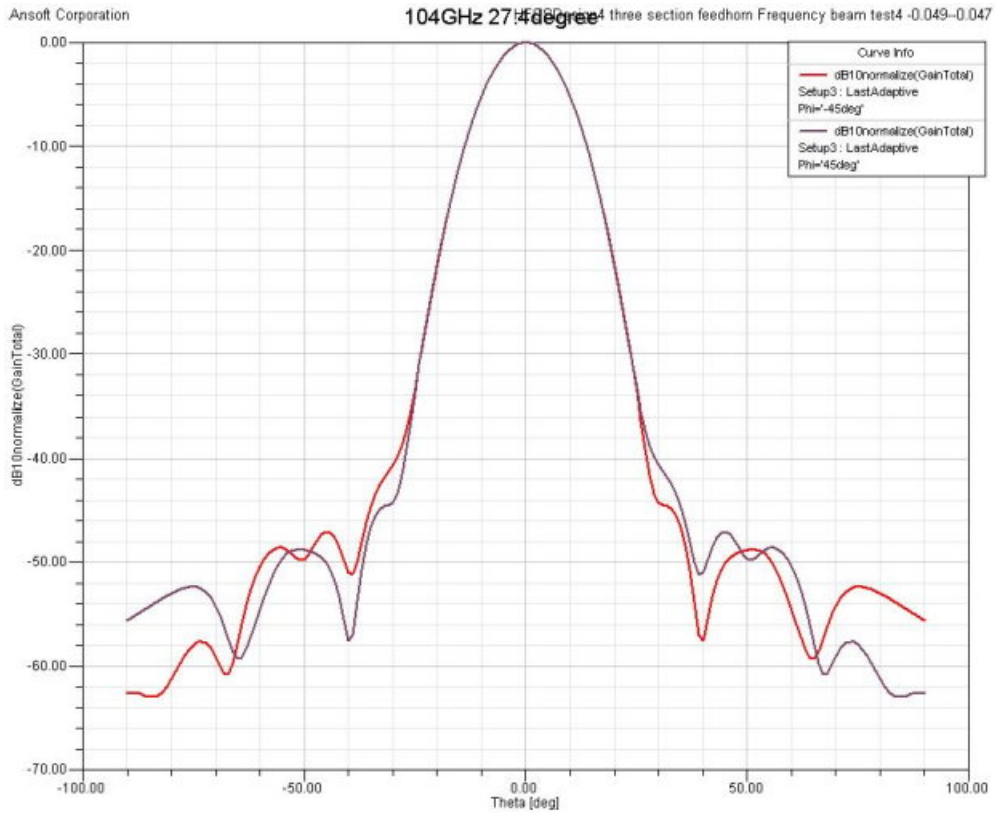


Figure 2.10: 104GHz radiation pattern (45 degrees cut).

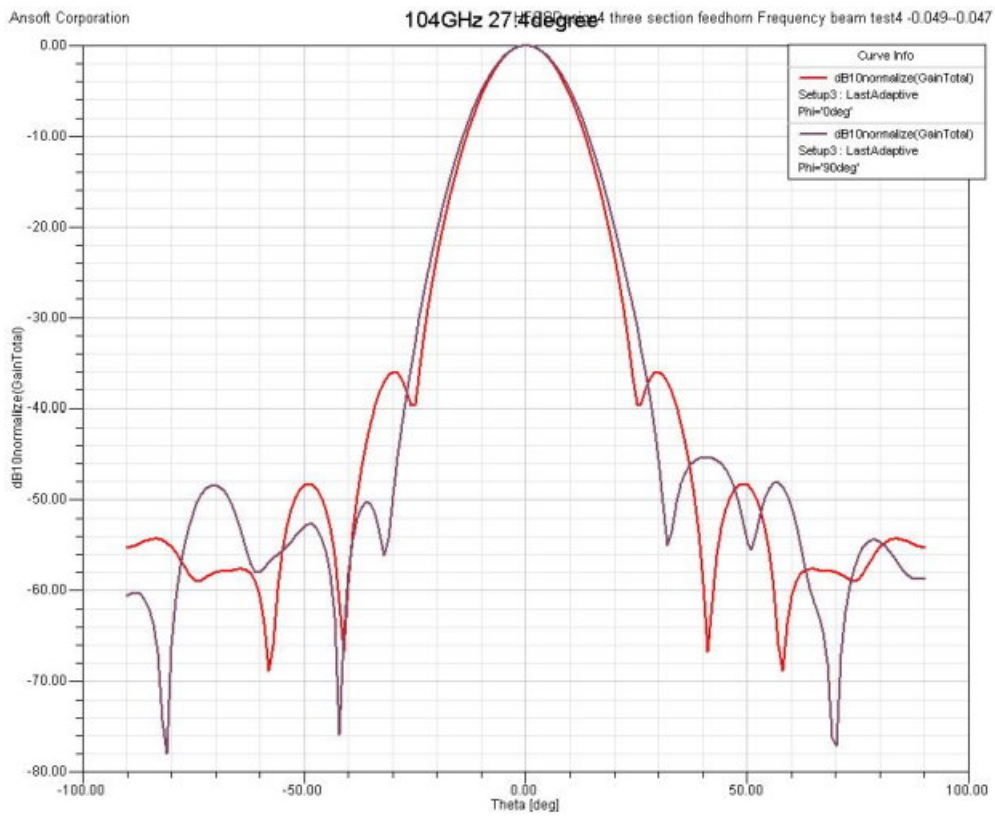


Figure 2.11: 104GHz radiation pattern (0 degrees cut).

AMIBA's dish, which uses a medium value, -10.5dB of horn taper edge at 14 degrees [84], we thus adopt -10dB at 14 degrees. For the horn design, the AMIBA corrugated horn has the semi-flare angle of 14 degrees, and the Leech's horn has a narrow one of 9 degrees, resulting in a broad radiation pattern [79]. Hence, we use HFSS to fine-tune the radiation pattern by adjusting each flare angle of the Potter feedhorn. EM simulations reveal that the increasing semi-flare angle gives the narrower radiation pattern.

The Leech's horn reported the 25% bandwidth. Exceeding the bandwidth limit will cause the E/H plane asymmetry of the radiation pattern. However, employed the -10dB taper edge criteria, we can exclude the asymmetry part outside 14 degrees, and hence extends the bandwidth. Figure 2.3 shows the radiation pattern of E-plane, H-plane and 45 degrees in 80, 95, 105, and 116GHz, in which the -10dB taper edge is between 12.5 and 14 degrees. Though 80GHz radiation pattern has high side-lobes in H-plane, resulting in the asymmetry, we can still utilize the central symmetric beam inside 14 degrees, which covers the reflector. For ensuring the tool machining, we made the gypsum mold from feedhorns, and the projection of molds, shown in the figure, indicates the inner surface and slopes is smooth and accurate.

2.2.6 Circular Stainless Waveguide

Despite the IR filter that blocks thermal radiation, the low-noise amplifier cooled at 20K suffers the thermal conduction from the feedhorn, which is under 70K. A commercial gold-plated circular waveguide, made of brass, contains 2.5mm thickness that gives a lot of thermal loads. Therefore, we employ a particular circular stainless steel waveguide, in which the thickness is only 0.2mm. The length is 80mm, and the inner diameter is 3mm. A gold of 1.0um thickness plated on the inner surface, using the specific brush plating technique without the nickel buffer, provides the electrical conduction. The measured insertion loss is 0.3dB. Compared to a stainless waveguide without plating, the gold layer only increases 3.24% of waveguide's thermal conductivity. Moreover, a gold-plated stainless circular waveguide's thermal conduction is only 0.064% of a gold plated brass waveguide with the same dimensions. See 4.1 for the discussion of the heat transfer.

2.3 Septum Polarizer

Millimeter/sub-millimeter telescopes equipped with the septum polarizer provide dual-polarization observations. An ideal septum polarizer converts an input linear polarization wave into right-hand polarization (RHP) and left-hand polarization (LHP), with equal power at two output ports. In a specific arrangement, if the input is a circularly polarized wave, it will pass through only one output port and leaving the other output port null. This novel feature of the septum polarizer makes it distinct from the other device, the ortho-mode transducer (OMT), which separates an input linearly polarized wave into two components of the electric field, parallel and perpendicular to the device symmetry axis at two output ports [115].

The septum polarizer is known for the relatively narrow frequency range, limited to the appearance of resonances. On the contrary, the OMT covers a wide bandwidth and has installed in modern telescopes such as ALMA. It will be a great leap forward in the polarimetry instrumentation if we move this weakness of the septum polarizer. In our study, we report a resonance-free circular polarizer covered 42% bandwidth, challenging the conventional bandwidth limit [20]. Stokes parameters, constructed from the measured data between 77GHz and 115GHz, show that the leakage from I to Q and U is below $\pm 2\%$, and the Q-U mutual leakage is below $\pm 1\%$. We also develop the D-band and G-band septum polarizer for extensions. In 2.3.1 to 2.3.4, we introduce the polarizer design and measurement. Detailed studies include the literature review, polarization leakages, D-band, and G-band results, are given in 3.1.

2.3.1 Septum Design

Figure 2.4 shows the schematics of the septum polarizer. A stepped metal septum cuts a circular waveguide into two half-circular output ports. For an input E_y , the electric field must rotate 90 degrees to reach the output ports, and thus the two electric fields at two output ports are 180 degrees out of phase. By contrast, an input E_x remains intact in orientation, and the two output electric fields are in phase (Figure 2.5). The septum serves an impedance transformer, which slows down the phase velocity of E_y , and creates a phase

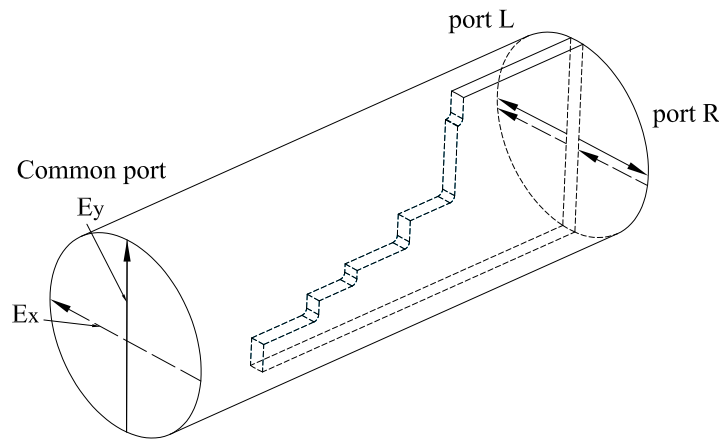


Figure 2.12: A typical configuration of the stepped septum polarizer in a circular waveguide. Vertical component (E^y) and horizontal component (E^x) of the electric field fed into the common port are separated by the septum to become the right-hand polarization component output at port R and the left-hand polarization component output at port L.

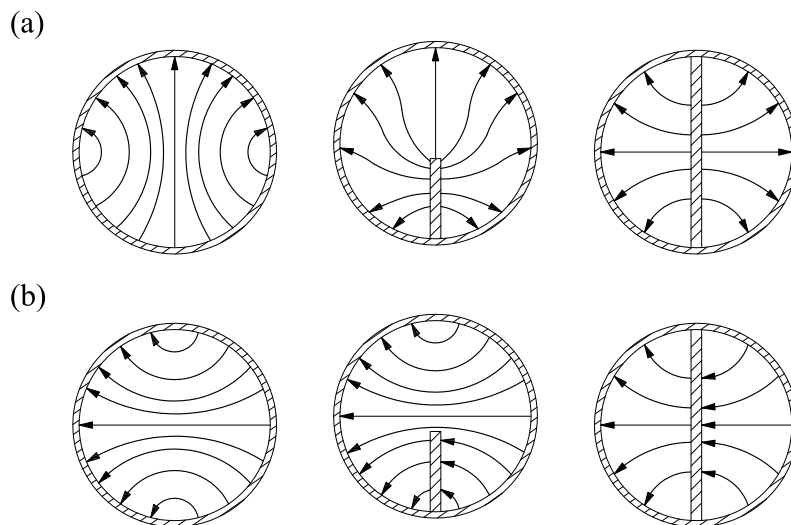


Figure 2.13: Field distributions of an E^y input (a) and an E^x input (b). The electric current smoothly circulates in opposite directions on either side of the common wall (septum) for the E^x input as if no septum ever existed. But the current flows in the same direction on either side of the common wall for the E^y input, so that the septum top edge becomes a stagnation point for charge accumulation. Therefore, a virtual TM_{01} mode, which has primarily the radial electric field, is excited. A good septum is able to re-convert the virtual TM_{01} mode back to the TE_{11} mode on its exit to output ports.

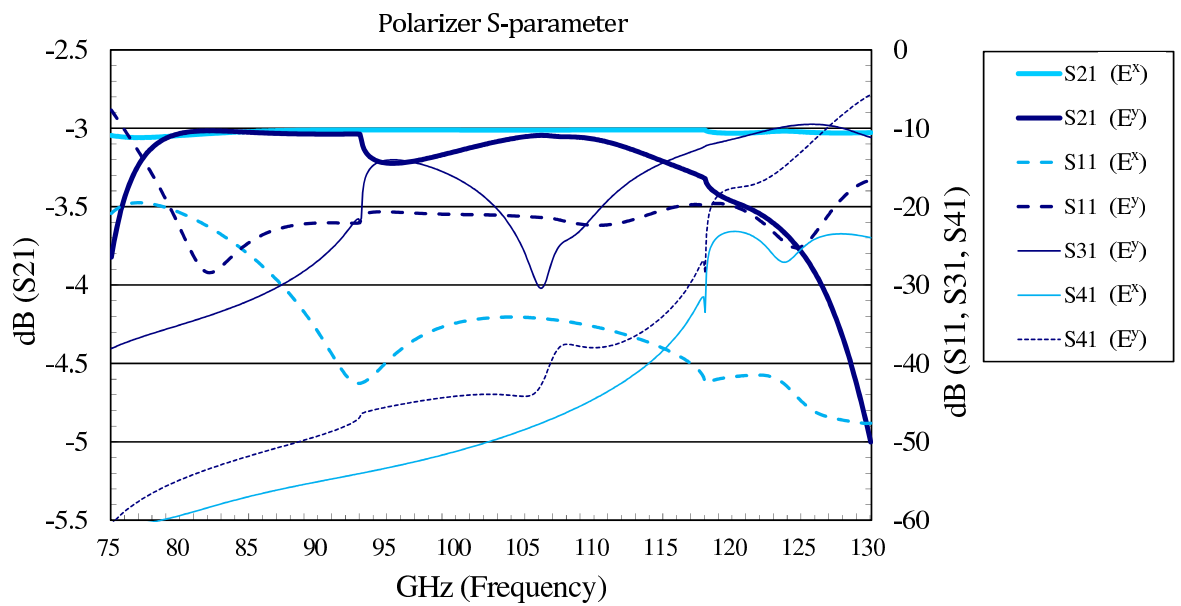


Figure 2.14: Simulation results of the transmission S_{21} and the reflection S_{11} of the fundamental TE_{11} mode, and of the reflected TM_{01} (S_{31}) and TE_{21} (S_{41}) modes, for our optimized septum polarizer. These simulation results are for an ideal polarizer, where the left-right symmetry is obeyed. For the E^y input, the TM_{01} is seen to be well suppressed except near the TM_{01} cutoff frequency 93 GHz. But even near this frequency the suppression is still good at the -14dB level with an insertion loss 0.2dB. Most impressively, this polarizer design has been tuned to eliminate all resonances across the entire W-band and beyond 120 GHz. The even higher-order modes TE_{21} begins to be excited beyond 118GHz for both E^y and E^x inputs, and the transmission S_{21} for the E^y input deteriorates rapidly beyond 120 GHz.

delay related to E_x . To preserve the input and output powers when both E_x and E_y are present, it follows that the phase delay must be -90 degrees. Hence, the electric field at two output port is RHP and LHP. We denote the input port as the common port, the RHP output port as the port R, and the LHP output port as the port L.

Our design principle of the septum is prohibiting any cavity modes, at the expense of allowing for some low level of TM_{01} modes, shown in the figure, which can radiate away through the input end. We begin with a size free design. When the widest percentage bandwidth is identified, we then fix the device size in accordance with the range of frequency desired. Given the circular waveguide with a 5-step septum, we use HFSS to optimize the height and the width of each septum step, based on the $\lambda/4$ rule. We find that a careful septum design can suppress TM_{01} modes beyond the excitation frequency. The optimized polarizer with the diameter of 2.5mm is free of resonances, not only across the entire W-band but also extending beyond 120 GHz. The septum thickness is 0.2mm for the mechanical rigidity of a bronze septum. Figure 2.6 shows the optimized HFSS results, where the TE_{11} modes (E^x , E^y) at the common port are denoted as mode 1, the TE_{11} mode at R/L ports as mode 2, the excited TM_{01} mode as mode 3, and the excited TE_{21} mode as mode 4. Here, the S parameter is defined as:

$$S_{ij}(E^{x,y}) = 10 \log_{10} \frac{|E^{x,y}(\text{mode}_i)|^2}{|E^{x,y}(\text{mode}_j)|^2}. \quad (2.2)$$

It shows that the input reflections $S_{11}(E^x)$ and $S_{11}(E^y)$ are under -20dB and $S_{31}(E^y)$ under -14dB within 94-118 GHz. The high-order mode TM_{01} cannot be excited by the E^x input. Hence, $S_{31}(E^x)$ is indeed close to zero and not shown in Fig. (3). The transmission $S_{21}(E^x)$ is nearly perfect; however, $S_{21}(E^y)$ has some loss due to energy conversion to the high-order mode beyond 93 GHz, and the loss is at most 0.2dB in between 94 and 100 GHz and 0.3dB at 118 GHz. We find that the excitation of TM_{01} mode is unavoidable beyond its cutoff frequency, and beyond 118 GHz an even higher-order mode TE_{21} begins to be significantly excited for both E^y and E^x inputs. Nevertheless one can manage to keep the high-order excitation level low at least up to 118 GHz. In particular, the simulation results

show that avoiding resonances is achievable over a very wide frequency range (75 - >120 GHz), thus opening a new regime of operation for a waveguide septum polarizer.



2.3.2 Polarizer Measurement

Despite that we can suppress the high-order excitation to a great degree, there is still some low level of TM_{01} mode that gets reflected back to the front-end devices. If the devices connected to the common port do not allow the TM_{01} mode to radiate, the reflection leads to a cavity effect and creates spurious resonances. Hence, devices at the common port require a total transmission of TM_{01} modes. In the telescope setting, a feedhorn connected to the polarizer allows the reflected TM_{01} mode to radiate away. However, if we measure the septum polarizer by connecting the common port to the rectangular waveguide, the excitation mode is reflected back to the polarizer, thereby producing new resonances. For this concern, we present two types of measurements, with the HP 8510 vector network analyzer (VNA) covered 75-115 GHz.

For measurement A, the common port is connected to a Potter feedhorn, and the R and L ports are connected to the two ports of VNA. For measurement B, one port of VNA is connected to the common port via a rectangular-to-circular waveguide transition adapter and the other port of VNA to the R(L) port, with the L(R) port properly terminated. Measurement A tests the performance of the R/L port return loss and mutual isolation. If there are internal multiple reflections, such as cavity modes produced by TM modes, measurement A reveals the resonances. On the other hand, measurement B applies a transition adapter in between the VNA and the common port, which reflects the excited TM_{01} mode back to the polarizer and creates resonances in the VNA measurement. Nevertheless, if one ignores the responses at some discrete resonances and reads only the continuum results, measurement B provides the full characteristics of the polarizer.

2.3.3 Measurement A

Figure 2.7 summarizes the results, where the measurement agrees with HFSS results. First of all, no resonance appears in this measurement. In the interval between 85 and 115

GHz, the return loss and the isolation are below -20dB. The slight rise of return loss to -17dB in the low-frequency interval 77-85 GHz is due to the mismatch between the WR10 rectangular waveguide of the VNA and the semi-circular waveguide of the polarizer (see 3.1). In our receiver setting, the mismatch is corrected by a transition adapter, which is a part of the stainless circular waveguide. In early studies, the polarizer under the setting of measurement A has shown resonances above the frequency of high-order modes(). Our results provide no resonance in measurement A, providing an evidence against any cavity mode inside the septum polarizer. Full justification of this claim requires the measurement B.

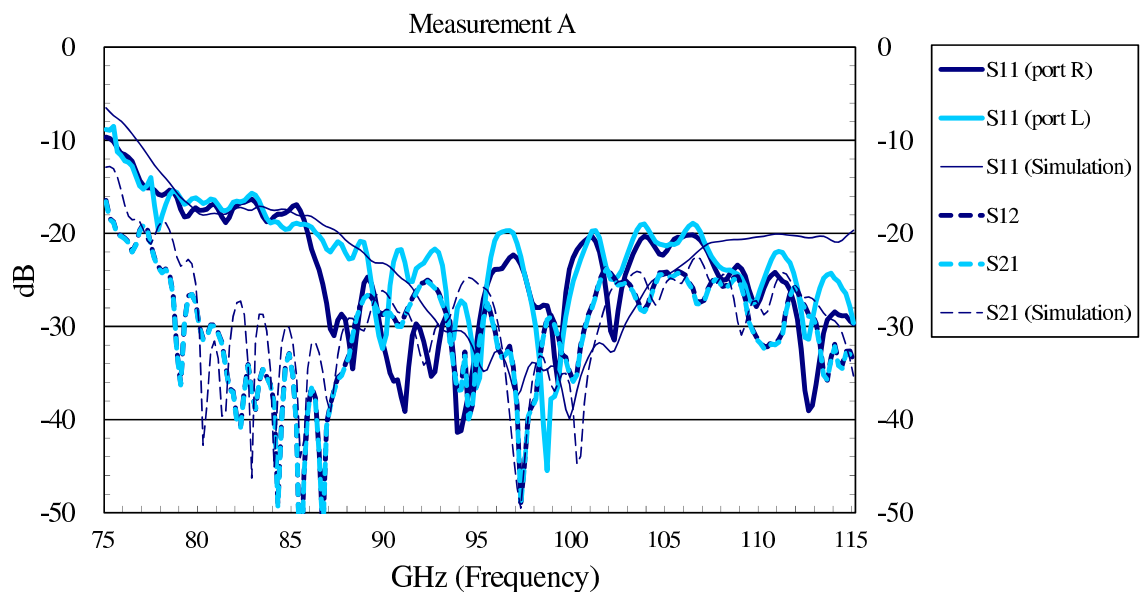
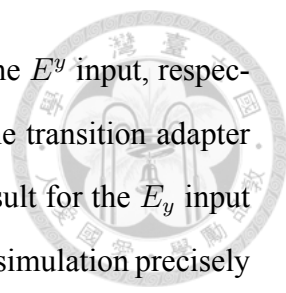


Figure 2.15: Results of isolation S_{ij} and reflection S_{ii} for measurement A, and results of the simulation with an identical setup as the measurement. The overall agreement between the two is very good. The measured S_{12} turns out to be indistinguishable from the measured S_{21} .

2.3.4 Measurement B

As mentioned in 2.3.2, measurement B cannot be free of resonance problems due to the VNA rectangular waveguide port that reflects TM_{01} modes to the polarizer, presenting



spurious resonances. Figure 2.8 shows results for the E^x input and the E^y input, respectively. Here the length of the circular waveguide section between the transition adapter and the septum is chosen to be the shortest possible, 0.2mm. The result for the E_y input reveals three resonances at 95.2, 104.2, and 110.2 GHz, and the HFSS simulation precisely yields the same resonances. The result for E_x shows an unexpected single resonance at 95 GHz. The resonance is produced from the mutual leakage between E^x and E^y , due to axis misalignment by 1.8 degrees. The interface of the axis misalignment is between the transition adapter and the polarizer. HFSS simulation verifies this misalignment as well. We also note that the power imbalance of R and L ports in input E^x and in input E^y measurements tends to be opposite. This axis misalignment also relates to the mutual leakage of Stokes Q and U , discussed in 3.1. However, In real telescope applications, the transition adapter will not be present, and the axis misalignment will not be an issue of concern.

Other than these discrete resonances, the polarizer performs well in the continuum, with about 0.2-0.3 dB additional power loss compared to the ideal polarizer simulation results. This additional loss is partly caused by the transition adapter preceding and a splitter following the polarizer. The output power imbalance between R and L ports in the continuum is also small, within 0.2 dB on average and 0.3 dB maximum, despite that half of the power imbalance is produced by irrelevant axis misalignment. The phase at each frequency has also been measured but is not shown here, which is essential for our further examination of the mutual leakage among four Stokes parameters, given in 3.1.

To examine the behaviour of resonances, we design the same measurement but with different length of rectangular-to-circular transition adaptors of 5mm and 10mm. Together with figure 2.9, we find that none of these resonances is in common in all three cases of different external cavity lengths, indicative of no internal cavity mode in the polarizer. We also find that all measured resonances coincide with the simulation resonances. The confirmation further reinforces our confidence that this polarizer is free of resonance over the measurement range.

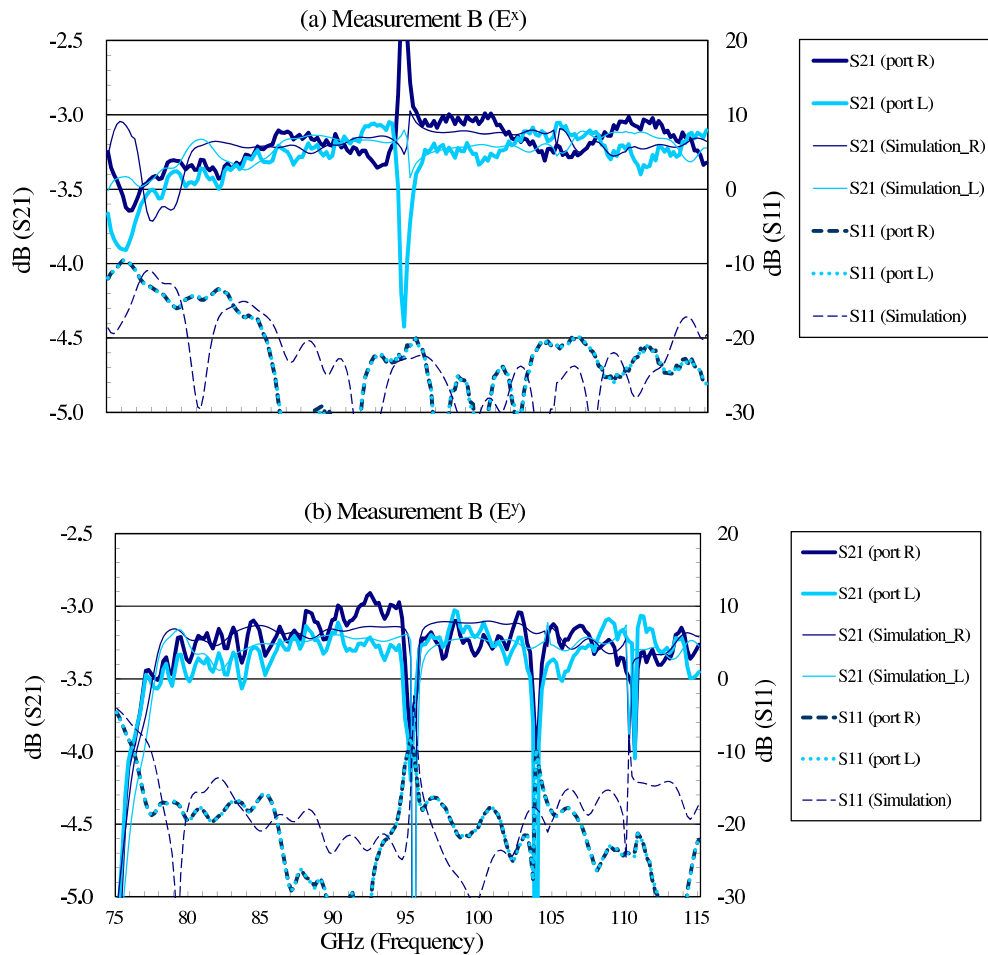


Figure 2.16: The measurement B and simulation results for the E^x input (a) and the E^y input (b). The rectangular-to-circular transition adapter is 0.2 mm in length. The unexpected resonance at 95 GHz shown in (a) is due to slight axis misalignment of 1.8 degrees at the interface between the adapter and the polarizer. The agreement between measurement and simulation is considerably good; especially the measured resonances are all captured by simulations. Again, we find the measured S_{11} 's for both R and L outputs are almost identical.

2.4 LNA

The solid-state amplifier based on transistors have shown very low-noise characteristics in millimeter-wavelength, between 1 cm and 1 mm (or 30–300 GHz in frequency). Examples include the high electron mobility transistor (HEMT), the metamorphic HEMT (mHEMT), and the heterojunction bipolar transistor (HBT). The monolithic microwave integrated circuit (MMIC) technology is applied for the compactness and small chip size. In recent years, amplifiers have reached 400–700 GHz operating frequencies and beyond, revealing the potential for THz operation [95] [94].

HEMT and HBT both employ the heterojunction, but the former applies field-effect transistors, and the latter uses bipolar junction transistors. The heterojunction is an interface between two layers or regions of distinct semiconductors, which have different energy bands and hence create a particular energy gap. For HEMT and HBT amplifiers, the substrate made of indium phosphide (InP) presents an excellent performance in high-frequency applications [113]; however, it is expensive. The mHEMTs offer a low-cost alternative for InP amplifiers. In mHEMTs, the active device layers are grown on a metamorphic buffer layer, for example, an InP-based transistor grown on a gallium arsenide (GaAs) substrate. The buffer layer can fit its lattice constant to the indium channel, allowing more degree of freedom to optimize the gain, linearity, high frequency, and low noise. Moreover, mHEMT allows a larger wafer size for the GaAs substrates than pure InP substrates [109] [94].

In our receiver, we apply the LNA produced by OMMIC, which contains the mHEMT channel with 70nm length and works in 75-110 GHz [21] [23] [108] [25] [111]. A high Indium content added in the HEMT channel improves the noise performance and frequency limits. Fig shows the on-wafer measurement at room temperature, where the overall gain is 28dB in 75-115 GHz, and the noise figure (NF) is 3dB in 75-110 GHz. NF rises to 5-8dB in 110-115 GHz, above the LNA working frequencies. Here NF means $\log F$, F is the noise factor. The on-wafer result indicates that the LNA can work up to 116GHz with tolerable degradations. $f S_{input}$ and S_{output} mean the signal power at input and output, N_{input} and N_{output} mean the noise power at input and output, S/N indicates the signal to

noise ratio (SN ratio). The noise factor (F) is defined as the input SN ratio divided by the output SN ratio [88]



$$F = \frac{S_{input}/N_{input}}{S_{output}/N_{output}} \quad (2.3)$$

We can further write the output signal power, S_{output} , as GS_{input} , where G is the receiver gain, and therefore:

$$F = \frac{N_{output}}{GN_{input}} \quad (2.4)$$

The output noise power includes the noise from the source, receivers, and the surroundings. The equation 2.4 indicates that F is the output noise power divided by the noise due to the input source only. In our case, assumed the same GN_{input} , 8dB NF means the output noise power is two times 3dB NF, which degrades the sensitivity of telescopes. A telescope equipped with LNAs giving 8dB NF requires four times the integration time than 3dB NF.

We can also estimate NF at the cryogenic temperature. If $N = GkTB$, N_{output} is equal to $Gk(T_0 + T_e)B$, N_{input} is equal to GkT_0B , and hence [4],

$$F = 1 + \frac{T_e}{T_0} \quad (2.5)$$

T_0 is the input noise at room temperature, 290K, and T_e is the equivalent noise temperature of LNAs. Again, 3dB NF implies $F = 2$, and $T_e = T_0 = 290K$. The cooled LNA at 20K will give roughly $F = 1.069$ and $NF = 0.3dB$, which means 3dB NF decreases by a factor of ten.

We aim to develop an LNA with a pre-amplification of 40dB, which contains two LNA chips and works under cryogenic temperature. We introduce the LNA housing in 2.4.1. In 2.4.2 and 2.4.3, one-chip and two-chip housing measurements are presented. Detail studies, including the transition probes, adhesives, ribbon bonding, and cryogenic housing, are discussed in the next chapter.

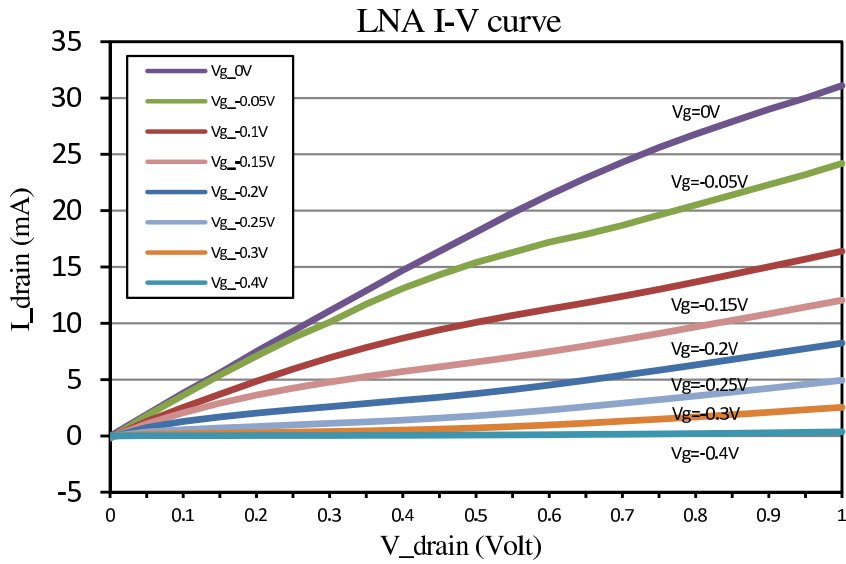


Figure 2.17: LNA I-V curve.

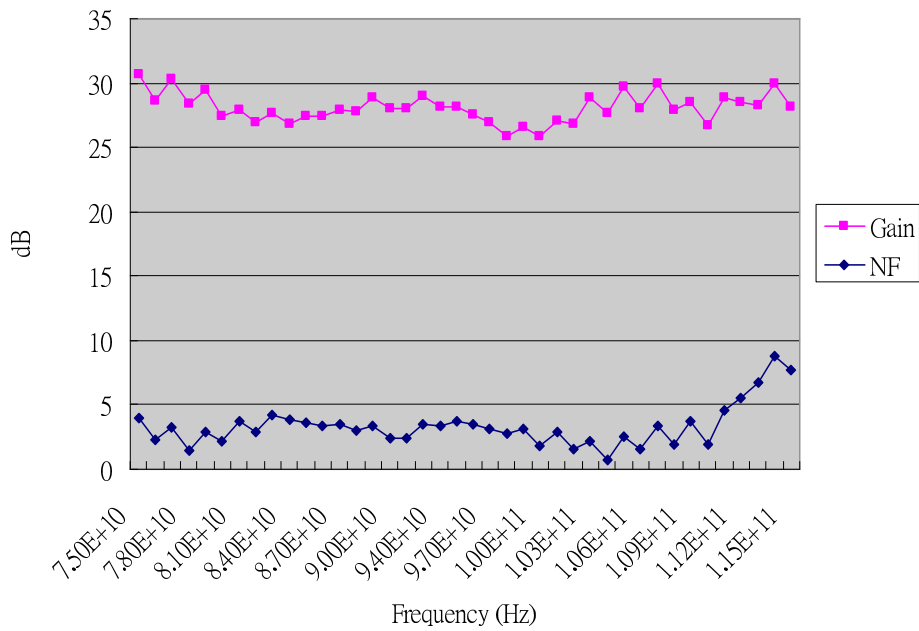


Figure 2.18: LNA gain and noise measured on wafer.



2.4.1 LNA Housing

The W-band LNA chip, provided by OMMIC, consists of four similar transistor stages, and each stage has one gate voltage (V_g) and one drain voltage (V_d). Eight biases in total are independently biased. The first stage's gain is about 6dB, not very high, and therefore we can fine-tune each bias for the minimum noise figure and an average gain of 25dB. The figure shows the measured I-V curve. Each line depicts the total drain current ($I_d(total)$) related to the changing V_d and a fixed V_g , where the gate current (I_g) is zero. While reaching the max gain, the V_d is about 1 volt (V), and the $I_d(total)$ is 40 milli-ampere (mA). In sum, we have ten parameters of bias for one-chip measurement, including V_{g1} - V_{g4} , V_{d1} - V_{d4} , I_g , and $I_d(total)$.

The figure shows the metallic housing made of brass, which contains the waveguide to microstrip line transitions, chips, a short microstrip line, capacitors, and wire bonds. The LNA chip size is $3 \times 2mm^2$, and chip thickness is 0.1mm. The waveguide to microstrip line transition (transition probe) connects LNA chips to a 90-degrees waveguide bender. The 90-degrees bender, not shown in the figure, creates enough space for the transition probe. The transition probe picks up and converts the EM wave from waveguide modes into the microstrip line mode, which is an impedance transform from a high value of 500 ohms to 50 ohms. Moreover, the air has $\epsilon = 1$, and GaAs has $\epsilon = 12.9$, the probe substrate thus requires a material of a dielectric constant in between 1 and 12.9, such as Rogers RT/Duroid 5880 ($\epsilon = 2.2$), quartz ($\epsilon = 3.7$), and the alumina ($\epsilon = 9.4$). We apply the alumina as the material of probe substrate. The silver adhesives, Epotek H20E, attach components to the metal housing, including transition probes, capacitors, and LNA chips. Capacitors prevent the bias circuit from voltage drops and current vibrations. For further reducing the possible variation of the power supply, we design a simple exterior circuit on FR4 boards, not shown in the figure. The exterior circuit contains bias connectors, a 1k ohms resistor for each I_g , and a 10 ohms resistor for each I_d .

LNA pads include the bias pads for gates/drains and ground-signal-ground pads for signal input/output. We apply two kinds of bond wires. One is the gold bond wires of 1mil diameter that connects the bias pads, the 10 pF capacitors put inside, and the 1nF capaci-

tors put outside. The other one is the gold ribbon wires with a cross-section of 1mil×3mil (0.25mm×0.75mm), connect transition probes and ground- signal-ground pads. The ribbon bond wire plays an essential role in LNA housing, and hence its dimensions are critical, for example, the wire length, bonding height, and the location of probes and LNA chips. HFSS simulations indicate that the optimized ribbon wire length from pad to pad is 120um, which represents the inductance of 80 pH (see 3.2 for more discussions). We employ the wire bonder TBT HB05 to connect these wires, and we thank Dr. Jerry for the suggestions and helps.

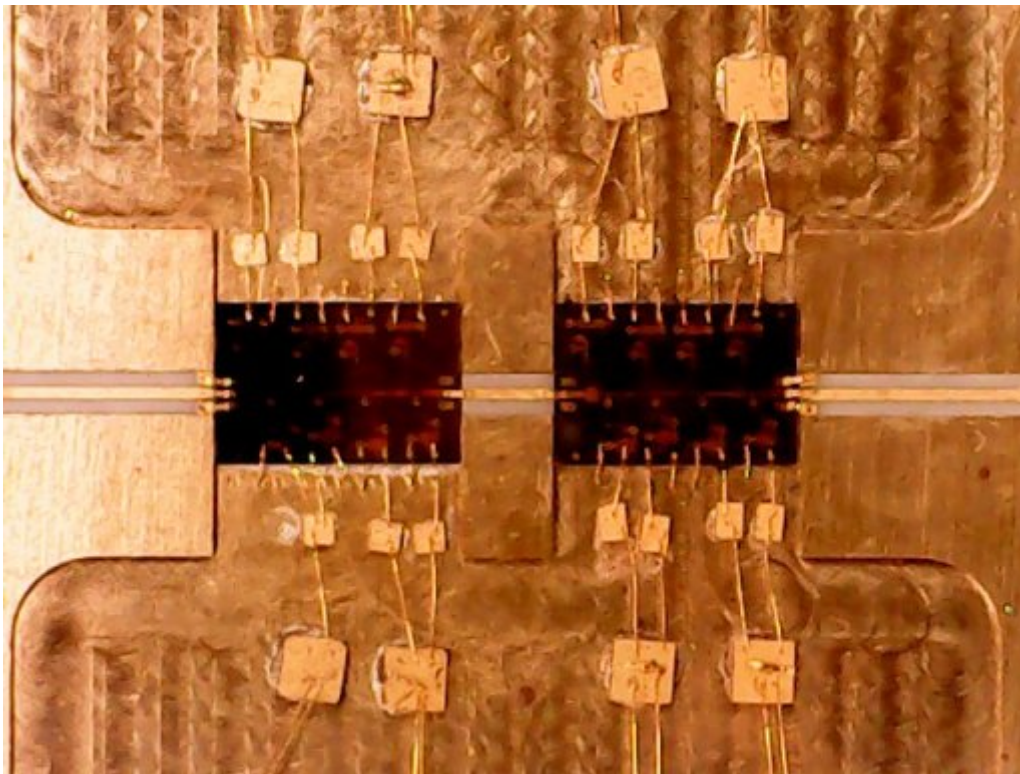


Figure 2.19: Picture of a LNA housing.



2.4.2 Transition Probe Measurement

The back-to-back transition probe, which contains two transition probes connected at each microstrip end, is a simple model to test the probe design [69]. The measurement result shown in the figure gives the transmission S21 is -1.3dB in 75-110 GHz and -1.8dB in 110-115 GHz, where the port1 and port2 are identical waveguide interfaces. The reflection S11 is -15dB in 75-115 GHz and rises to -12dB at 112 GHz. There is a 1dB additional loss due to the electric resistance of silver adhesive and possible imperfect grounding. S11 and S22 imply the standing wave ratio (SWR), where the reflection coefficient versus frequencies reveals a constant interval between local minimums. This interval is related to the total line length between two VNA ports. Because the back-to-back housing is similar to the one-chip housing, except for the chip and bond wires, the two housings should have comparable characteristics. In the figure, the interval of minimums is 8GHz, giving the line of 20mm, the dimension of housings (8GHz implies a transmission line length of 10mm in the alumina).

2.4.3 One-chip LNA Measurement

The figure shows the measurement of the one-chip housing, in which the port one and port 2 mean the input and output port. As we mentioned in 2.4.2, the one-chip housing and the back-to-back housing have very similar S21 responses. The one-chip housing has one V_g and one V_d , combined from $V_{g(1-4)}$ and $V_{d(1-4)}$. While we apply $V_g = -0.11V$, $V_d = 1.69V$, and the $I_{d(total)} = 36mA$, the gain (S21) shows 22dB averaged in 75-110 GHz and a decline toward high frequencies until 16dB at 115GHz. The isolation from port 2 to 1 is very high ($S_{12} < -60dB$). The port 2 (S22) reflection is -16dB in 80-100 GHz and -6dB in other frequencies.

However, the reflection measured at the port 1 is too small ($S_{11} < -30dB$), which is due to a 20dB attenuator put between the port 1 and VNA heads. In the VNA 8510A setting, the test head gives the signal power of -16dBm and its power upper limit is 6dBm. If the reflected power from devices is larger than 6dBm, the test head will be saturated and shown a fixed -10 dB response. Hence, the 20dB attenuator diminishes the input power

to at least -36dBm and avoid the VNA saturation, and its attenuation contributes most of the reflection loss. We have tried to include the attenuator in the calibration by moving the reference plane to the interface between the attenuator and LNAs, but the test head is still saturated. For this issue, we measure the second housing, which uses the same design but is not optimized, by another 75-110GHz HP8510XF system. Though lacking the information of 110-115GHz, the test head can work under the reflected power and thus provide correct S11. The figure shows the measurement, in which the S11 is in between -6dB and -8dB.

While an LNA is operated, its gain requires flatness and stability in all frequencies. We thus define 3dB as the minimum value of gain variations, where the gain variation means the difference from a local maximum to the adjacent minimum, and 3dB implies a half-power loss. For the one-chip housing (see the figure), the gain variation is <3dB in the working band, 75-110GHz, and <4dB in 110-115GHz. Without an absorber attached, the one-chip housing has an excellent performance in 75-110GHz and a modest gain in 110-115GHz.

2.4.4 Two-chip LNA measurement

Due to a white bias board placed at one side of the die, a weakness of the one-chip housing design is two bond wires that have to cross over the LNA chip. The crossing wires degrade the gain and increase the noise. Thus, in the two-chip housing design, we put two white bias boards on both sides of the die, and the crossing wire issue is solved. We also measure the two-chip housing, with and without crossing wires, and the latter one shows a better response.

The two-chip housing has three biases, including VG, VD12, and VD34. VG is combined from gate biases of two chips, VD12 is from drain biases of the former chip, and VD34 is from drain biases of the latter chip. The design difficulty is how to handle the multi-reflection between chips that produce possible resonances and LNA oscillations. Therefore, a short alumina microstrip line placed between chips, the same design as the air channel of transition probes, forbids higher-mode and diminishes reflections. The length

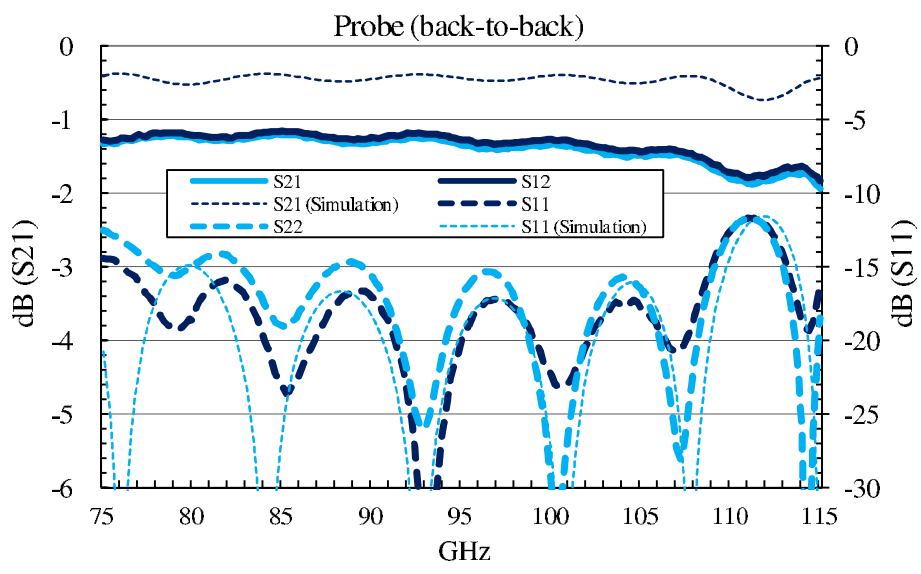
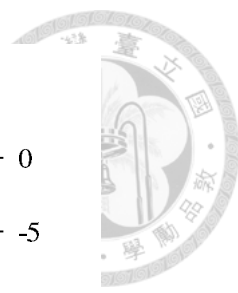


Figure 2.20: Measurement of a Alumina B2B probe

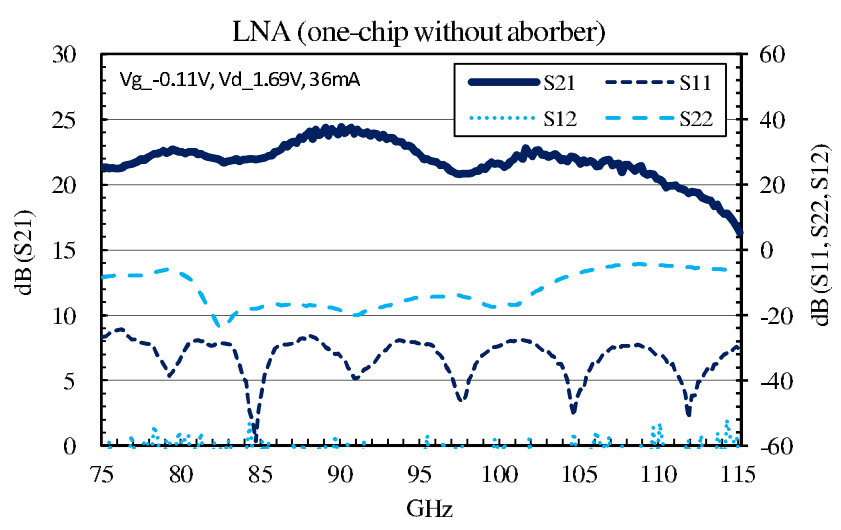


Figure 2.21: Measurement of a one-chip LNA without absorbers.

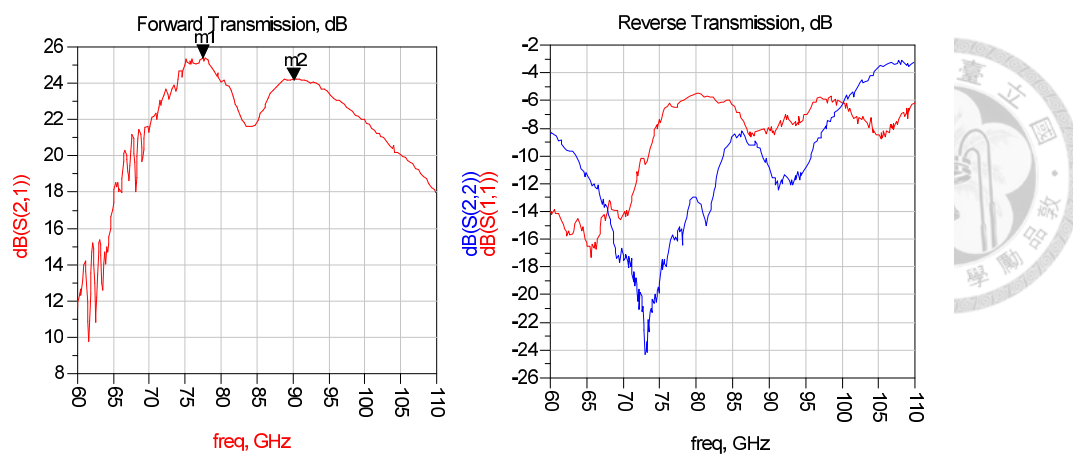


Figure 2.22: LNA S11 measurement.

of the alumina trace is 1.3mm, about five times a quarter wavelength of 100GHz in alumina. The figure shows VNA measurements without absorbers. While we apply $V_G = -0.18V$, $V_{D12} = 1.5V$, and $V_{D34} = 1.3V$, the gain (S_{21}) is 40dB averaged in 75-105GHz, and 35dB averaged in 105-115GHz, where I_{D12} is 19mA, and I_{D34} is 30mA. The isolation (S_{12}) is 60dB, and the weak input reflection ($S_{11} < -30dB$) is due to a 40dB attenuator, which is for avoiding the test head saturation.

The port 2 (S_{22}) reflection is -8dB, but it appears two resonances, 94GHz and 101GHz, shown $S_{22} > 0dB$ and two corresponding bumps in S_{21} . Though the S_{21} is very stable in at least one hour, the two resonances still reveal a possibility of the LNA oscillation, which means the gain varies with time and frequencies. In cryogenic temperature, oscillations may worsen, so we can hardly determine the accurate noise power. We thus define the criteria for the reflection, S_{11} and S_{22} are $< -3dB$.

The resonances are usually caused by the high-order mode produced by reflections between chips. Therefore, add an absorber is a simple way to eliminate resonances. By attaching an absorber on the ceiling of the second chip, we successfully remove unwanted resonances. The figure shows the same measurement but adding an absorber. The result gives that S_{22} is below -6dB in 75-115GHz, and the curve of S_{21} is flatter than an LNA without absorbers. Furthermore, if we exclude 100-104GHz, where the gain reaches 50dB, the gain variation in 75-115GHz is below 3dB, representing excellent performance.

The final version of LNAs installed in receivers will contain four chips, giving more biases. Furthermore, one has to take the thermal load into account, making the housing

design more complicated. The figure presents the cryogenic LNA housing.



2.5 RF Components after LNA

After LNAs, the receiver components include bend waveguides, stainless waveguides, faraday rotation isolators, high-pass filters, the waveguide feed through, and mixers. The waveguide feed-through is installed on the receiver wall, and the mixer is placed in the air. Each component plays an essential role for receivers, such as mechanical supports, heat isolation, signal isolation, filtering, vacuum seal, and signal mixing. Since a 40dB pre-amplification has controlled the receiver noise, the loss of each component after LNAs is not critical. We expect the insertion loss is $<1.5\text{dB}$ for each passive device.

2.5.1 Waveguide Bend

The waveguide bend is applied to increase the space between components and avoid the cold head of cryogenic pumps. Types of bend include the E-plane and H-plane, where the E-plane bend is a waveguide bent along the E-plane (or the rectangular waveguide's shorter side), and the H-plane bend is that bent along the H-plane (or the rectangular waveguide's longer side). The definition of E-plane is a plane along the propagated E-field lines of TE₀₁ mode, and the H-plane, represented as a plane on which B-field lines of TE₀₁ mode circulate, is perpendicular to the E-plane. We can think that the E-plane bend is bent easier, and the H-plane bend is bent harder (Microwave 101).

We employ mostly the E-plane bend waveguides, and a few are H-plane bends. The waveguide bend connects LNAs and the stainless waveguides, where the waveguide's projected length is 114mm. One side of a waveguide bend is matched to the LNA output, which contains two waveguide ports in one flange, and the other side is a standard WR10 flange. The waveguide bend, made of brass and gold plated on its outer surface, is provided by Hengda Microwave. The VSWR of each bends measured by vendors is below 1.12, indicating $>21\text{dB}$ return loss. For checking, We have measured two E-plane bends by VNA, and the S₂₁ is -0.5dB. Besides, the waveguide bend can absorb displacement

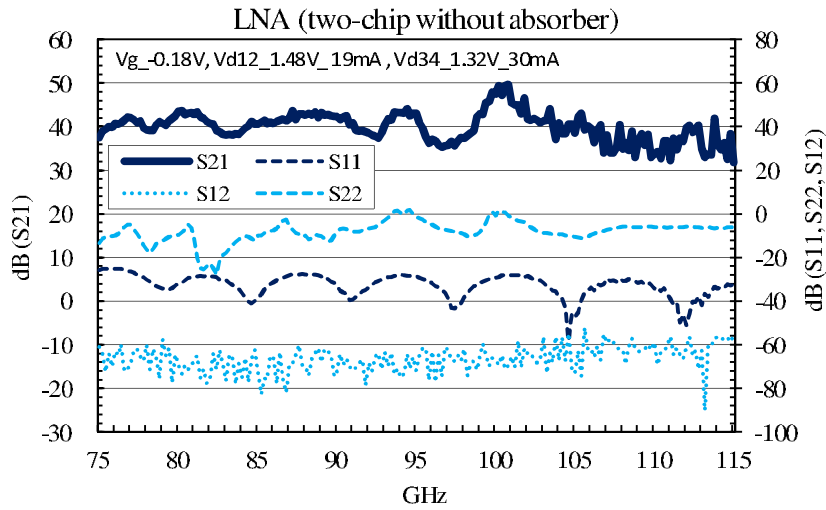


Figure 2.23: Two-chip LNA measurement without absorbers.

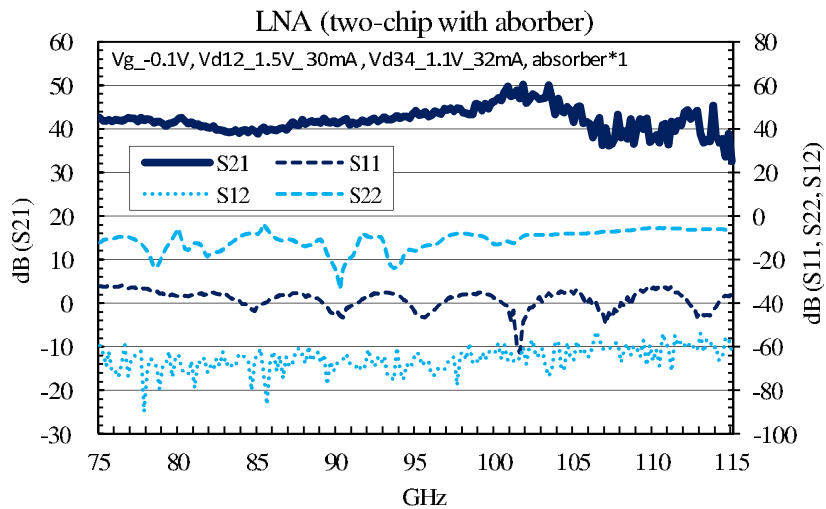


Figure 2.24: Two-chip LNA measurement added a absorber.

resulting from thermal contraction while the component chain is cooled.



2.5.2 Stainless Waveguide

The stainless steel waveguide provides thermal isolation for the first cooling stage. One side of a stainless waveguide, connected to the waveguide bends, is anchored by 70K, and the other side fixed to faraday isolators is at 300K. The multi-pixel LNA block has many waveguides directly coupled with the receiver wall. Compared to the circular stainless waveguide connected to feedhorns and contact the vacuum, the stainless waveguides suffer much more thermal loads. Therefore, we apply two stainless waveguides for an LNA output, one is placed inside the radiation shield, and the other is outside the shield. Each waveguide has a length of 3.8mm.

The thickness of a standard stainless waveguide provided by Penn Engineering is 0.28 mm. Due to thermal loads and cost, we design a simple waveguide compressed from a stainless steel tube, and the waveguide thickness is only 0.1mm. The stainless tube made of SUS304, with an outer diameter of 2.1mm, is cramped to an elliptical-like shape, in which the longer side is flat, and hence the elliptical tube is similar to a rectangular waveguide. Since a cramp can only confine the minor axis, we made several elliptical tubes with the different minor axis and compared them with simulations. The simulation shows that while the minor axis is restricted to 1.16mm, and the major axis is 2.485mm, the waveguide has S21 of 0.5-1.5 dB in 80-116GHz.

The ends of the stainless waveguide are soldered by waveguide flanges made of brass and aluminum. For welding with stainless steel, it is challenging to use high thermal conductive materials, brass and aluminum, in which aluminum is more difficult due to a low melting point, 660°C. In comparison, stainless steel is melting at 1450°C. Using the surrounding noble gas of Argon, one can solder brass with stainless steel. The aluminum soldering is more complicated. One must plate aluminum with a copper film, and stainless is joined on the copper surface with the Argon welding.

The figure shows the measurement of a stainless waveguide with a length of 3.8mm, in which the simulation and measurement coincided very well. The insertion loss (S21)

is 0.6dB in 95-115GHz and increases to -1.4dB at 75GHz. The return loss (S11) is >20dB in 90-115GHz and >12dB in 75-90GHz. The high reflection in low frequencies is caused by a mismatch between a stainless waveguide and a WR10 port, but since LNA has high isolation of 60dB, the reflected power is ignorable.

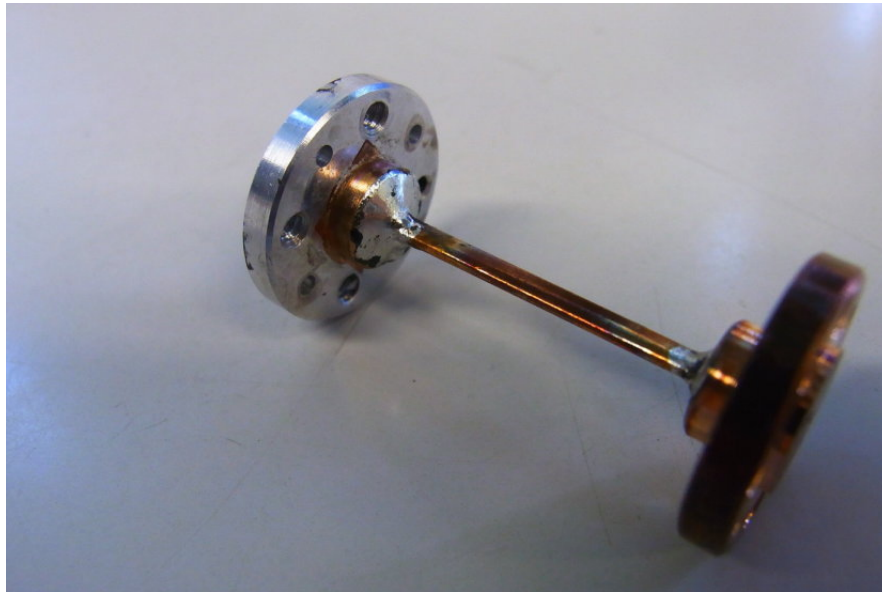
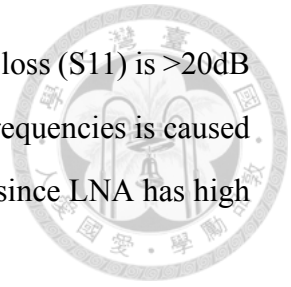


Figure 2.25: Picture of a stainless waveguide soldering on an aluminum flange.

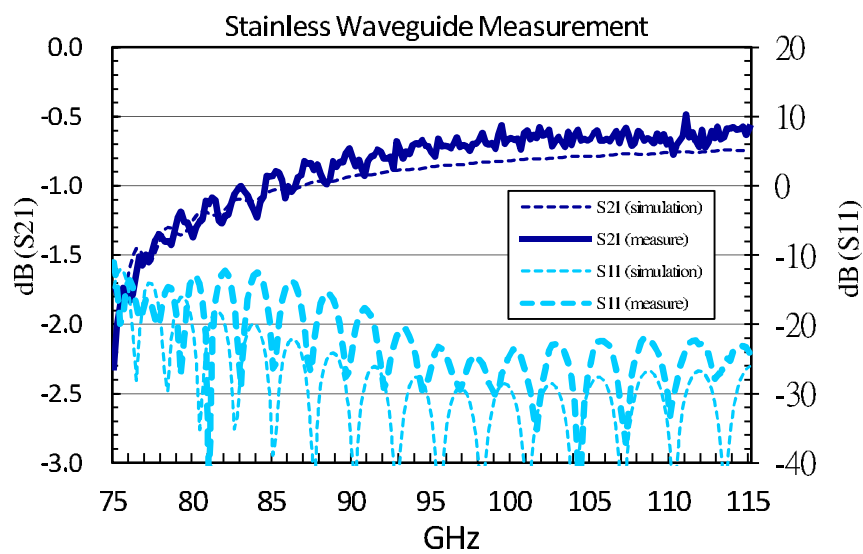
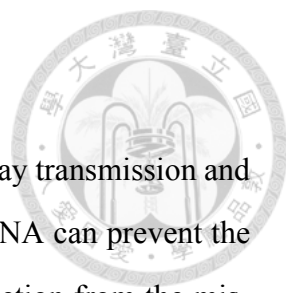


Figure 2.26: Measurement of stainless waveguides.

2.5.3 Faraday rotation Isolator



A Faraday rotation isolator is a two-port device that allows one-way transmission and forbids the opposite way [30] [31]. Connected with an isolator, an LNA can prevent the LNA oscillation by suppressing unwanted power, including the reflection from the mismatch between LNA and mixers and the leakage from the local oscillators (LO). For example, the two-chip LNA has an isolation of 60dB, a gain of 40dB, and S22 (the output port) of -6dB. If a mixer has a return loss of 5dB, the reflection from mixers fed into the LNA will be damped by 65dB (5dB+60dB=65dB), and hence the mixer reflection is not critical. However, the LO power is very high, such as 10dBm for a Ducommun balanced mixer, and in comparison, the LNA output power is -80dBm in weak source observations. Therefore, the LO power leakage will cause LNA oscillations. If a mixer have isolation of 20dB, the passive devices after LNA gives a loss of 5dB, the LO power leaked to LNA is thus -75dBm (10dBm-20dB-5dB-60dB = -75dBm). If equipped with an isolator of 20dB isolation, the LO power leakage will drop to -95dBm, much smaller than the LNA output power.

For this concern, the isolator applied in receivers requires isolation of >20dB, the return loss of >15dB, and the insertion loss of <1.5dB. In the figure, an isolator contains a ferrite rod, a dielectric cone, a dielectric cone embedded with a film, and two waveguide ports, where two dielectric cones are attached to the ferrite rod. We define port 1 as the forward wave's input port and port 2 as the output port. The orientation of the input waveguide is 45 degrees relative to the output waveguide. While applying a magnetic field parallel to the ferrite rod axis, and the forward direction is the same as the field, the polarization will rotate clockwise as the forward wave propagated in the magnetized ferrite. The rotation is named the Faraday rotation. If the rotation angle is precisely 45 degrees, the forward wave can pass through the waveguides. But for the reverse wave that transmits opposite to magnetic fields, the polarization still rotates clockwise by 45 degrees and perpendicular to the preferred direction of the port 1. Hence, the reverse wave cannot propagate through the isolator.

Put at port 1, a resistive metal film embedded in a dielectric cone can absorb the reverse

wave, where the film is aligned to the polarization of reverse waves. The dielectric cone is a taper that transmits waves from a ferrite ($\epsilon > 12$) to air ($\epsilon = 1$), and hence the dielectric material requires low-loss and a high dielectric constant, such as alumina ($\epsilon = 10$). A small Teflon tube supports the ferrite rod, and the absorber tape attached to the tube diminishes unwanted resonances.

Given an applied magnetic field H and an incident wave frequency w , with $\gamma H \ll w$, a condition of small applied field, the Faraday rotation equation is simplified to [44]

$$\theta = 4\pi M \gamma l \sqrt{\epsilon} / 2c \quad (2.6)$$

Where $4\pi M$ is the axial magnetization of ferrites, l is the ferrite length, c is the speed of light, ϵ means the ferrite's dielectric constant, and γ means the electron gyromagnetic ratio ($8.795 \times 10^6 (g \cdot rad) / (sec \cdot oersted)$, g implies the Landé g-factor). In a weak field, the equation indicates the Faraday rotation angle is proportional to the magnetization and independent of the frequency. The dielectric constant is frequency-dependent, but it is usually measured at low frequencies, such as 10MHz. In high frequencies, ϵ will change to a different value, altering the rotation angle and impedance matching. For example, the nickel ferrite TT2-111 has $4\pi M$ of 5000 gauss and g of 2.11. While rotating by 45 degrees, $\pi/4 = 5000 \times (8.795 \times 10^6) \times 2.11 \times \sqrt{\epsilon} l / (2 \times 3 \times 10^{11})$, which gives $\sqrt{\epsilon} l = 5.0705mm$. If we use $\epsilon = 12.5$ (9.4GHz) provided from the datasheet, the ferrite length is 1.434mm. If we use $\epsilon = 14.1$ from the measured value in 70-100GHz [58], the ferrite length is 1.35mm. A solution is to apply a longer ferrite length and a smaller applied field, giving an unsaturated ferrite, and hence we can modify the overall performance by changing magnetic fields. We use the ferrite length of 1.78mm suggested in Erickson's study [30].

2.5.4 Faraday Rotation Isolator Measurement

The figure shows the measurement and simulation results. S21 means the transmission, the S12 is the isolation, and S11, S22 are reflections at two ports. In 80-115GHz, S21 is -1.2dB averaged, S12, the isolation is -15dB in 80-115GHz but higher with -12dB at 100GHz, and both S11 and S22 are below -15dB. Below 80GHz, S11 rises to -10dB

and S_{21} is -1.6dB. The dot lines represent the simulation results and coincide well with measurements. Compared to Erickson's isolator, which has S_{21} of -0.6dB, S_{12} of -30dB, and reflection of -25dB, our isolator is still imperfect. We think the resistive metal film is the reason that gives weak isolation and thus reduces overall performance. The film is Ag-Pd, plated on a half alumina cone with a specified resistivity of 0.1 ohm-cm, 10um thickness, and particular dimensions. The metal film provides only electric resistivity but no magnetic resistance. If we add magnetized particle inside films, the ability of EM filed absorption will be improved.

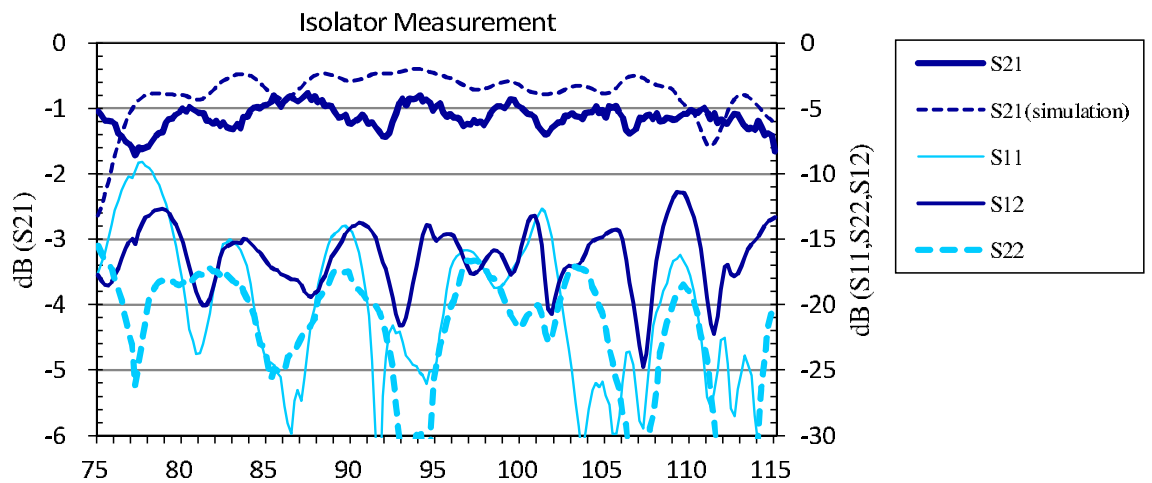


Figure 2.27: Measurement of Faraday rotation isolators.

2.5.5 High-Pass Filter

A receiver obtains not only the in-band power but the noise in lower frequencies from the surroundings. Therefore, a suitable high-pass filter is required to select the desired band and exclude the lower-band noise. For the higher-band noise, the IR filter mentioned in 2.3.2 forbids infrared radiations. The high-pass filter based on a stepped-wall rectangular waveguide, where the dimension of the wider wall is reduced, creating a waveguide transformer [72]. At the narrowest part, the width and the length of the waveguide determine the filter cutoff frequency and the steepness of high-pass response, respectively. Hence, the machining tolerance at the narrowest part is critical. Each filter consists of two

identical halves, cut in E-plane or H-plane. The E-plane is in parallel to the E-field lines of TE_{01} mode. The H-plane is where the B-field lines of TE_{01} mode circulate, perpendicular to the E-plane. The waveguide machining prefers cutting in E-plane instead of H-plane, because the H-plane cut interrupts the surface current on the shorter wall, causing more losses.

We apply the high-pass filter, divided by E-plane, and the cutoff frequency is 80GHz. A filter design defines the 3dB point of insertion loss, representing the slope of attenuation. If the slope is steep, the 3dB point will be closed to the cutoff frequency. For example, a commercial SAGE 75-110GHz high-pass filter sets 3dB point at 73.5GHz. The frequency interval from 3dB point to cutoff point is 1-2GHz. We choose S_{21} of -3dB at 79GHz.

2.5.6 Waveguide Feed through

The waveguide feed-through is the last receiver component that separates vacuum from the air and transmits RF signals outside. The feed-through consists of three parts: two waveguide flanges and one window. The window put in between flanges is made of dielectric such as Mylar, epoxy [26], or quartz. The O-rings give the vacuum seal between the three components and receiver walls. Since the 14 signal outputs are close and compact, the waveguide feed-through must use O-rings of smaller diameters. Applied the Mylar film, we have designed the waveguide feed-through, but it requires further VNA measurement and vacuum leak test.

2.5.7 Mixer

The mixer put in room temperature down-convert RF signals into IF signals. We apply the balanced mixer, Ducommun FDB series, which provides 9 dB conversion loss and 20 dB port isolation in 75-110 GHz. The maximum input signal power is 17 dBm. Meanwhile, using 90nm CMOS, National Chiao-Tung University has designed the mixer module that combines a mixer, IF, and LO circuits (the earlier prototype is published in [104]). We aim to employ the mixer module in upgraded front-end receivers.

2.6 Summary

In table 2.4, we summarize the optical and RF components mentioned in this chapter.

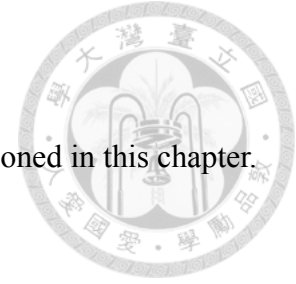


Table 2.4: Summary of receiver components

Components	Note	Performance
Dish	Cassegrain reflector, 1.2 m diameter	Gain: 60 dBi
Vacuum window	Zotefoam	Insertion loss: 0.1 dB
IR filter	Quartz plated with metal meshes	Emissivity: 0.8
Feed horns	Smooth wall design	Gain: 25 dB
Septum polarizer	Resonance free (77-118 GHz)	Insertion loss: 0.3 dB
LNA	Two OMMIC chips	Gain: 40 dB
Stainless waveguide	0.1mm wall thickness	Insertion loss: 0.8 dB
Isolator	TT2-111 ferrite	Isolation: 15 dB
High-pass filter	Stepped-wall design	30 dB cutoff (80 GHz)
Mixer	balanced mixer	Conversion loss : 9 dB



Chapter 3

Discussion of Critical RF Components

In this section, we discuss three critical receiver components, including the septum polarizer, low noise amplifiers (LNA), and Faraday rotation isolators.

3.1 Resonance-Free Septum Polarizer

3.1.1 History

The principle of a septum polarizer has been known for decades. The very first concept of the septum polarizer is given in [91]. The author conceived a simple picture, in a circular waveguide, how the field lines propagate along a sloping septum. While E^x is unimpeded, E^y must have a slower phase velocity with its orientation turning ± 90 degrees on either side of the septum. The understanding of the septum came to light some years later. The septum was regarded as a common wall [18] which has a spatially varying slot with changing cutoff frequencies [97] [12]. The in-phase fields fed into port R/L causing the current to circulate in opposite directions on either side of the common wall, thereby closing the current circuit at the slot without disturbance. By contrast, the out-of-phase fields cause the current to flow in the same direction on the two sides of the common wall, and the slot interrupts the current, altering the impedance.

In modern stepped septum polarizers, each step in the septum can be regarded as an individual slot. If one alters the slot shape, the septum polarizer is equivalent to a single-

ridge waveguide. The ridge waveguide, such as single-ridge or double ridge, has been extensively studied for bandwidth enhancement and better impedance match [75] [15]. The ridge effect lowers the cutoff frequency and hence explains why the phase velocity of E^y is slower than E^x . Height-varying ridge yields changing cutoff frequencies and control various degrees of delay over some frequency interval. A careful septum design can often yield a 90-degree delay in E^y relative to E^x over some finite frequency interval.

Early developments of the septum polarizer were for phased array applications [83]. A five-element phased array with receivers installed with sloping septum polarizers was soon reported in a conference, where the polarizer achieves 15% bandwidth [24]. Several years later, the first paper was published in which a stepped septum in a square waveguide was used; the authors report that the polarizer can achieve an even wider (20%) bandwidth [18]. In the same paper, the authors claimed that the 20% bandwidth was close to the bandwidth limit. After this initial publication, square waveguide polarizers remained popular until 1991 when the first circular waveguide polarizer with a stepped septum was made [12]. Circular waveguide polarizers have the advantage that the interface to the front-end feed horn is natural without the need of a transformer, and they have since been widely used in antenna arrays [62] [34] [35].

Early investigations of the septum polarizer were limited to methods of trial-and-error. The first analysis of a slot septum was conducted based on the Wiener–Hopf method [9]. Subsequently, the mode-matching method, generalized transverse resonance method, and finite-element method were suggested as design improvements [27] [12] [33]. In these studies, the excitations of high-order TE and TM modes presented major challenges, thus making it necessary to adopt the single-value decomposition method of isolating the excitation modes from the fundamental mode [63]. It was not until 1995 that an optimized square waveguide, four-step septum polarizer was reported [14]. That work provided detailed analyses of the dimensions of the steps and the thickness of the septum. Like [18], these authors also claimed that the polarizers maximum bandwidth was about 20%.

3.1.2 Summary of Historic Review

We sum up this brief review by listing three key issues discussed in the literature concerning septum polarizers. First, the bandwidth of the septum polarizer is primarily limited by that of the square (circular) waveguide. Chen's study [18] suggested that a square (circular) waveguide has a ratio of 1 : 1.4 (1 : 1.3) for the cutoff frequencies of the TE_{01} (TE_{11}) mode and the TE_{11} (TM_{01}) mode, therefore, the maximum bandwidth of the fundamental mode is at most 34% (26%). If we avoid the lowest 12% and the highest 2% bandwidth, where the polarizer performance is difficult to control, only 20% (12%) bandwidth for use. Even with further refinements, the polarizer has at most 25% (15%) bandwidth. Exceeding this limit is the excitation of high order modes, which can alter the phases of the fundamental modes and produce resonances. An increase in the step number will not help. The bandwidth limit considered above has been so fundamental that it cannot be broken [14].

Second, there is possibly an impedance mismatch between the septum polarizer and the connecting waveguides. The septum polarizer tends to perform well at lower frequencies of the working band, due to higher-order mode resonances. Hence, the polarizer must be made smaller by as much as 25% of its standard size, creating an impedance mismatch problem for the polarizer's interfaces to other typical waveguides, an issue noted in earlier studies [83].

Third, the 90-degree phase shift of E^y , relative to E^x over a wide bandwidth is a critical issue. Either placing an auxiliary Teflon thin plate next to the metal septum [18], or adopting corrugated walls in the waveguide [49] can achieve the phase delay. The corrugated wall has long been regarded as a phase shifter [100]. However, these improvements are impractical in high-frequency applications. Typical dimensions of the polarizer are too small for precision arrangements of extra components or fabrication of a complicated waveguide interior.

In this work, we report a novel design that yields good solutions to all of the issues listed above. We find it possible to break the aforementioned bandwidth limit by carefully optimizing the septum steps for suppressing high order excitations and resonances over

an unprecedentedly wide bandwidth. The circular waveguide septum polarizer reported here can reach a 42% bandwidth. Moreover, the dimension of the polarizer input/output ports is only 10% smaller than normal, making it easy to join waveguide components with unsophisticated impedance transformers. Most importantly, this septum polarizer, without any Teflon plate or corrugated wall for additional fine-tuning, has been designed for high-frequency applications, specifically for the W-band, and has been fabricated by conventional machining tools. An extension of 42% bandwidth designs include G-band and D-band are envisioned, challenging the 10% bandwidth G-band polarizer reported recently [66].

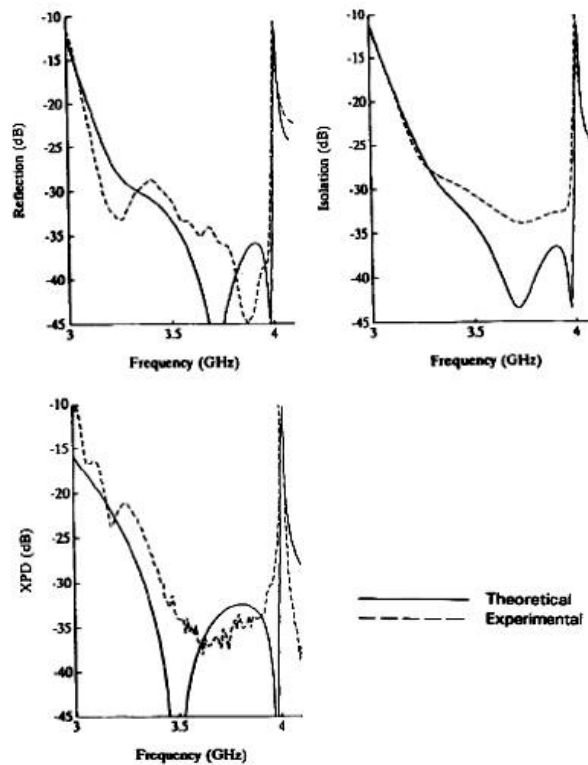


Figure 3.1: Resonances measured in the septum polarizer.

3.1.3 Comparison of Septum Polarizer and OMT

Polarization measurements require separating the incoming radiation into two orthogonal components to determine the Stokes parameters. Traditionally two devices have been available for the separation of polarization: the septum polarizer and the ortho-mode trans-

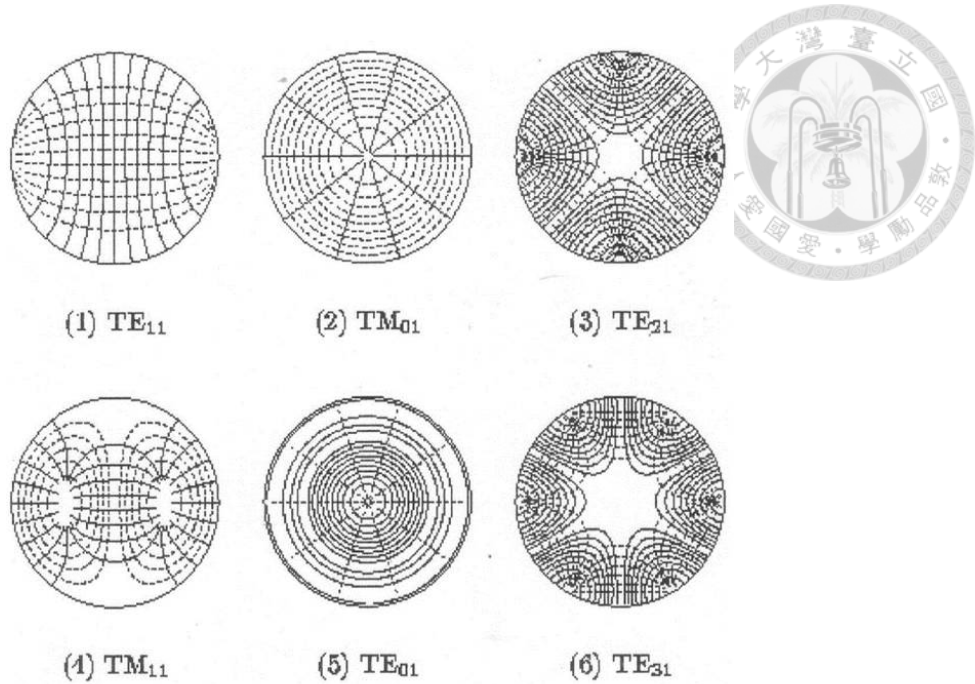


Figure 3.2: Waveguide modes of a circular waveguide.

ducer (OMT).

A further comparison for the two kinds of devices reveals that the septum polarizer is good for measurements of Stokes Q ($\equiv [\langle E^x E^{y*} \rangle - \langle E^y E^{x*} \rangle]/2$) and Stokes U ($\equiv [\langle E^x E^{y*} \rangle + \langle E^y E^{x*} \rangle]/2$), or the linear polarization, and the OMT good for those of Stokes U and Stokes V ($\equiv i[\langle E^x E^{y*} \rangle - \langle E^y E^{x*} \rangle]/2$), or the circular polarization, where $\langle \dots \rangle$ are the time average. The reasons are as follows. Consider linearly polarized signals and denote the outputs of the septum polarizer to be the right-hand polarization electric field, $E^R \equiv (E^x + iE^y)/\sqrt{2}$ and the left-hand polarization electric field $E^L \equiv (E^x - iE^y)/\sqrt{2}$. By cross-correlating E^R and E^L , we obtain Stokes Q as $\langle E^R E^{L*} + E^L E^{R*} \rangle$ and Stokes U as $\langle E^R E^{L*} - E^L E^{R*} \rangle$. In practice, one normally needs to amplify the weak incoming signals, with gains G_R and G_L , immediately following the polarizer. The constructed Stokes parameters are in effect $\langle G_R G_L \rangle Q$ and $\langle G_R G_L \rangle U$, assuming the gains are real. (See Section (6) for a discussion of complex gains.) If one has an approximate knowledge of the average gains G_R and G_L , the Stokes Q and U can be determined to an acceptable accuracy. This is what can be achieved with a septum polarizer that measures E^R and E^L directly. On the other hand, if one adopts the OMT, the Stokes U becomes

$\langle G_x G_y \rangle [\langle E^x E^{y*} \rangle + \langle E^y E^{x*} \rangle]$ and the Stokes Q becomes $\langle G_x^2 \rangle \langle |E^x|^2 \rangle - \langle G_y^2 \rangle \langle |E^y|^2 \rangle$. While Stokes U can be recovered in a similar manner as that with a septum polarizer, the recovery of Stokes Q has a serious problem [90].

This is because not only the polarized signal is already mixed with the much stronger unpolarized sky, but the amplifiers also introduce substantial unpolarized noise to the signal. Hence $|E^x|^2$ and $|E^y|^2$ contain almost the unpolarized radiation, and the recovery of weak polarized signals is reminiscent of the determination of a very small number by subtracting two big numbers from each other, for which any small error in the two big numbers will render a poorly determined small number. The recovery of Stokes Q is therefore only possible if the amplifier gains $\langle G_x^2 \rangle$ and $\langle G_y^2 \rangle$ can be calibrated to a high accuracy. However, due to the presence of gain fluctuations in amplifiers, a telescope equipped with an OMT is often difficult to yield a well-determined Stokes Q . On the other hand, when the polarized signal contains only Stokes U and V , a similar argument applies, except for replacing E^x by E^R , E^y by E^L , and the OMT by the septum polarizer. But, there have rarely been pure circular polarization signals in astronomical observations; hence the OMT is normally disfavored for astronomical polarization measurements and used mostly for the measurements of Stokes I . (Nevertheless, a sophisticated solution for polarization measurements with the OMT has been proposed [73].)

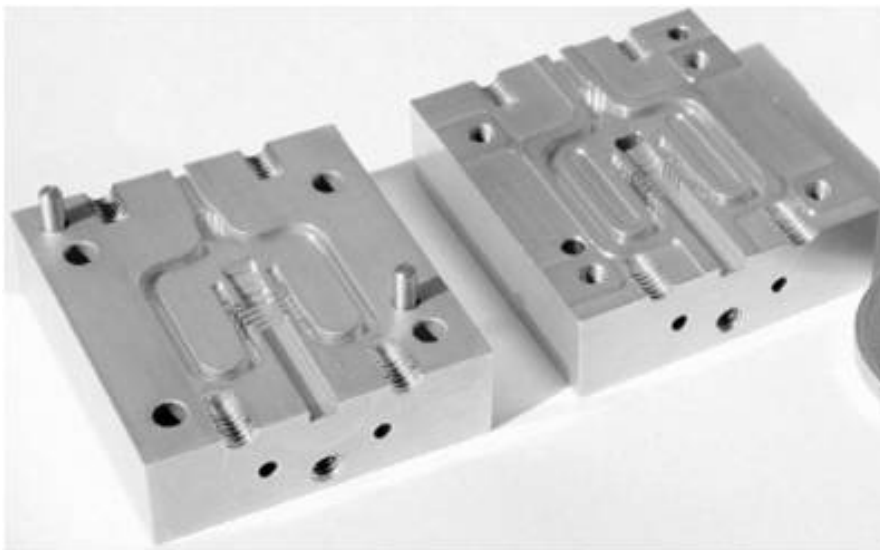
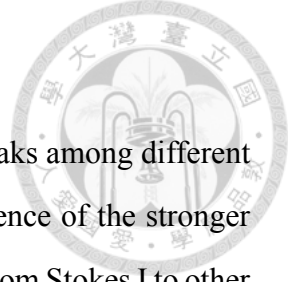


Figure 3.3: Example of the ortho-mode transducer.



3.1.4 Polarization Leakage

A number of minor imperfections in the polarizer lead to small leaks among different Stokes parameters. In view of the weak polarized signal in the presence of the stronger unpolarized source, the primary concern of a polarizer is the leakage from Stokes I to other three Stokes parameters. Other lesser critical concerns are the mutual leakage among the three polarized components. Since the observed polarized radiation is mostly linearly polarized, the Stokes V is zero, and the polarization mutual leakage is between Stokes Q and U . As long as the $Q - U$ leakage is controlled within the few-percent level, the performance of the polarizer is considered to be acceptable [68]. However, in very demanding observations such as the B-mode polarization observations of the CMB radiation, it is the level of $Q - U$ leakage that sets the sensitivity limit of an instrument [46] [78]. Below, we compute the mutual leakage of the four Stokes parameters from the data of measurement B with the 0.2 mm transition adapter.

The output complex electric fields at the R and L ports for an ideal septum polarizer are expressed as:

$$E^R = \frac{1}{\sqrt{2}}(E^x + iE^y) \quad (3.1a)$$

$$E^L = \frac{1}{\sqrt{2}}(E^x - iE^y), \quad (3.1b)$$

for an ideal septum polarizer. Consider different polarizers inside a pair of receivers (m, n) . The visibility is known as the time-averaged cross-correlation of the complex electric fields incident to receivers m and n , and the correlation responses are obtained as:

$$\langle E_m^R E_n^{R*} \rangle = \frac{1}{2}[(E_m^x E_n^{x*} + E_m^y E_n^{y*}) - i(E_m^x E_n^{y*} - E_m^y E_n^{x*})] = \frac{1}{2}(I + V) \quad (3.2a)$$

$$\langle E_m^L E_n^{L*} \rangle = \frac{1}{2}[(E_m^x E_n^{x*} + E_m^y E_n^{y*}) + i(E_m^x E_n^{y*} - E_m^y E_n^{x*})] = \frac{1}{2}(I - V) \quad (3.2b)$$

$$\langle E_m^R E_n^{L*} \rangle = \frac{1}{2}[(E_m^x E_n^{x*} - E_m^y E_n^{y*}) + i(E_m^x E_n^{y*} + E_m^y E_n^{x*})] = \frac{1}{2}(Q + iU) \quad (3.2c)$$

$$\langle E_m^L E_n^{R*} \rangle = \frac{1}{2}[(E_m^x E_n^{x*} - E_m^y E_n^{y*}) + i(E_m^x E_n^{y*} - E_m^y E_n^{x*})] = \frac{1}{2}(Q - iU) \quad (3.2d)$$

The co-polar $(E^R E^R, E^L E^L)$ correlations provide information about I and V and the

cross-polar ($E^R E^L$, $E^L E^R$) correlations about Q and U . For simplicity we consider a radiometer polarizer as an example with $m = n = 1$ and drop the receiver indices. We model the imperfect responses of the E^R and E^L outputs after the amplifiers as

$$\tilde{E}^R = \frac{G_R}{\sqrt{2}}[(1 - \Delta_R)E^x + ie^{i\alpha_R}(1 - \varepsilon_R)E^y] \quad (3.3a)$$

$$\tilde{E}^L = \frac{G_L}{\sqrt{2}}[e^{i\alpha_\Delta}(1 - \Delta_L)E^x - ie^{i\alpha_L}(1 - \varepsilon_L)E^y] \quad (3.3b)$$

where $\Delta_{R,L}$ and $\varepsilon_{R,L}$ denote the magnitude losses of E^x and E^y at ports R and L, and α_Δ , α_R and α_L denote the phase errors in reference to E^x at the R port. Here, $\Delta_{R,L}$, $\varepsilon_{R,L}$, α_Δ , α_R and α_L are of the same order of smallness $O(\eta)$, Here, $\eta < 2\%$ from the VNA measurements, and the leading-order corrections suffice to compute the leakage. We also take the amplifier gains, G_R and G_L , to be real. This is because the relative phase between the two complex gains and the relative path delay in \tilde{E}^R and \tilde{E}^L can be pre-determined and calibrated out. Hence after the phase calibration, the gain can be made a real quantity. The correlations of the two amplified electric fields now become:

$$\tilde{Q} \equiv \Re \langle 2\tilde{E}_1^R \tilde{E}_1^{L*} \rangle$$

$$= \langle |G_R G_L| \rangle \left\{ -\frac{1}{2}[(\Delta_L - \varepsilon_L) + (\Delta_R - \varepsilon_R)]I \right. \quad (3.4a)$$

$$\left. + \{1 - \frac{1}{2}[(\Delta_R + \Delta_L) + (\varepsilon_R + \varepsilon_L)]\}Q \right. \quad (3.4b)$$

$$\left. + \frac{1}{2}[(\alpha_L - \alpha_R) + \alpha_\Delta]U \right. \quad (3.4c)$$

$$\left. - \frac{1}{2}[(\Delta_L - \varepsilon_L) - (\Delta_R - \varepsilon_R)]V \right\}, \quad (3.4d)$$



$$\begin{aligned}\tilde{U} &\equiv \Im \langle 2\tilde{E}_1^R \tilde{E}_1^{L*} \rangle \\ &= \langle |G_R G_L| \rangle \left\{ -\frac{1}{2}[(\alpha_\Delta - \alpha_L) + \alpha_R]I \right. \end{aligned} \quad (3.5a)$$

$$\left. -\frac{1}{2}[(\alpha_L - \alpha_R) + \alpha_\Delta]Q \right. \quad (3.5b)$$

$$\left. + \left\{ 1 - \frac{1}{2}[(\Delta_R + \Delta_L) + (\varepsilon_R + \varepsilon_L)] \right\} U \right. \quad (3.5c)$$

$$\left. -\frac{1}{2}[(\alpha_\Delta - \alpha_L) - \alpha_R]V \right\}, \quad (3.5d)$$

$$\begin{aligned}\tilde{V} &\equiv \langle \tilde{E}_1^R \tilde{E}_1^{R*} \rangle - \langle \tilde{E}_1^L \tilde{E}_1^{L*} \rangle \\ &= \frac{1}{2} \left\{ \langle |G_R|^2 \rangle (1 - \Delta_R - \varepsilon_R) - \langle |G_L|^2 \rangle (1 - \Delta_L - \varepsilon_L) \right\} I \end{aligned} \quad (3.6a)$$

$$+ \frac{1}{2} \left\{ \langle |G_L|^2 \rangle (\Delta_L - \varepsilon_L) - \langle |G_R|^2 \rangle (\Delta_R - \varepsilon_R) \right\} Q \quad (3.6b)$$

$$+ \frac{1}{2} \left\{ \langle |G_L|^2 \rangle (\alpha_\Delta - \alpha_L) - \langle |G_R|^2 \rangle \alpha_R \right\} U \quad (3.6c)$$

$$+ \frac{1}{2} \left\{ \langle |G_R|^2 \rangle (1 - \Delta_R - \varepsilon_R) + \langle |G_L|^2 \rangle (1 - \Delta_L - \varepsilon_L) \right\} V, \quad (3.6d)$$

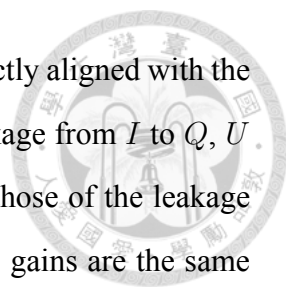
$$\begin{aligned}\tilde{I} &\equiv \langle \tilde{E}_1^R \tilde{E}_1^{R*} \rangle + \langle \tilde{E}_1^L \tilde{E}_1^{L*} \rangle \\ &= \frac{1}{2} \left\{ \langle |G_R|^2 \rangle (1 - \Delta_R - \varepsilon_R) + \langle |G_L|^2 \rangle (1 - \Delta_L - \varepsilon_L) \right\} I \end{aligned} \quad (3.7a)$$

$$- \frac{1}{2} \left\{ \langle |G_L|^2 \rangle (\Delta_L - \varepsilon_L) + \langle |G_R|^2 \rangle (\Delta_R - \varepsilon_R) \right\} Q \quad (3.7b)$$

$$- \frac{1}{2} \left\{ \langle |G_L|^2 \rangle (\alpha_\Delta - \alpha_L) + \langle |G_R|^2 \rangle \alpha_R \right\} U \quad (3.7c)$$

$$+ \frac{1}{2} \left\{ \langle |G_R|^2 \rangle (1 - \Delta_R - \varepsilon_R) - \langle |G_L|^2 \rangle (1 - \Delta_L - \varepsilon_L) \right\} V. \quad (3.7d)$$

The above four expressions contain the leading order Stokes parameters, Q , U , V and I , followed by the leakage from other three Stokes parameters on the order $O(\eta)$. The leakage obeys a symmetry principle, as a result of the scattering matrix being unitary or the quantity $I^2 - (Q^2 + U^2 + V^2)$ being an invariant, if no loss were to occur. The leakage coefficients between Q and U , Eq. (5.4c) and Eq. (5.5b), are the same in magnitude but



opposite in sign, representing the antenna principal axes are not perfectly aligned with the polarizer axes and rotate by a small amount. The coefficients of leakage from I to Q , U and V , Eqs. (5.4a), (5.5a) and (5.6a), respectively, are the same as those of the leakage from Q , U and V to I , Eqs. (5.7b), (5.7c) and (5.7d), when the two gains are the same $G_R = G_L$. The leakage between Q and V and that between U and V also have the same magnitudes but opposite signs when $G_R = G_L$. Finally, the net loss in Stokes I , Eq. (5.7a), is the same as the loss in Q , Eq. (5.4b), in U , Eq. (5.5c), and in V , Eq. (5.6d), again when $G_R = G_L$. Hence without amplifiers, the leakage in a septum polarizer is determined by 6 parameters, 3 from the amplitude imbalance, i.e., $\Delta_R + \Delta_L - \epsilon_R - \epsilon_L$, $\Delta_R - \Delta_L + \epsilon_R - \epsilon_L$, and $\Delta_R - \Delta_L - \epsilon_R + \epsilon_L$, and 3 from the phase imbalance, i.e., $\alpha_\Delta - \alpha_R - \alpha_L$, $\alpha_\Delta + \alpha_R - \alpha_L$, and $\alpha_\Delta - \alpha_R + \alpha_L$. If the polarizer is lossy, there will be an additional parameter, $\Delta_R + \Delta_L + \epsilon_R + \epsilon_L$, that gives uniform suppression of all 4 Stokes parameters.

3.1.5 Result of Polarization Leakage

Take the VNA measurement data for two individual septum polarizers fabricated with the same design, and we can compute various leakage coefficients according to the formula given above. As the measurements involve only VNA with no amplifiers, we let $G_R = G_L = 1$. In Figs. (8), we plot the leakage from I to other three polarization components and the polarization mutual leakage. The measurement results are consistent for the two polarizers, and they are summarized in Table. Clearly the leakage are systematically different below and above the excitation frequency at 95 GHz, despite they are both small. Given the finite line widths of the three resonances present in Fig. (6), the measured results of the nearby continuum are likely contaminated by the poor responses at the resonances. Therefore, the leakage should be regarded as pessimistic, and the actual performance should be better than the results indicated here. We additionally find that the mechanical requirement of the polarizer has no major bottleneck, judging from the performance consistency of the two polarizers.

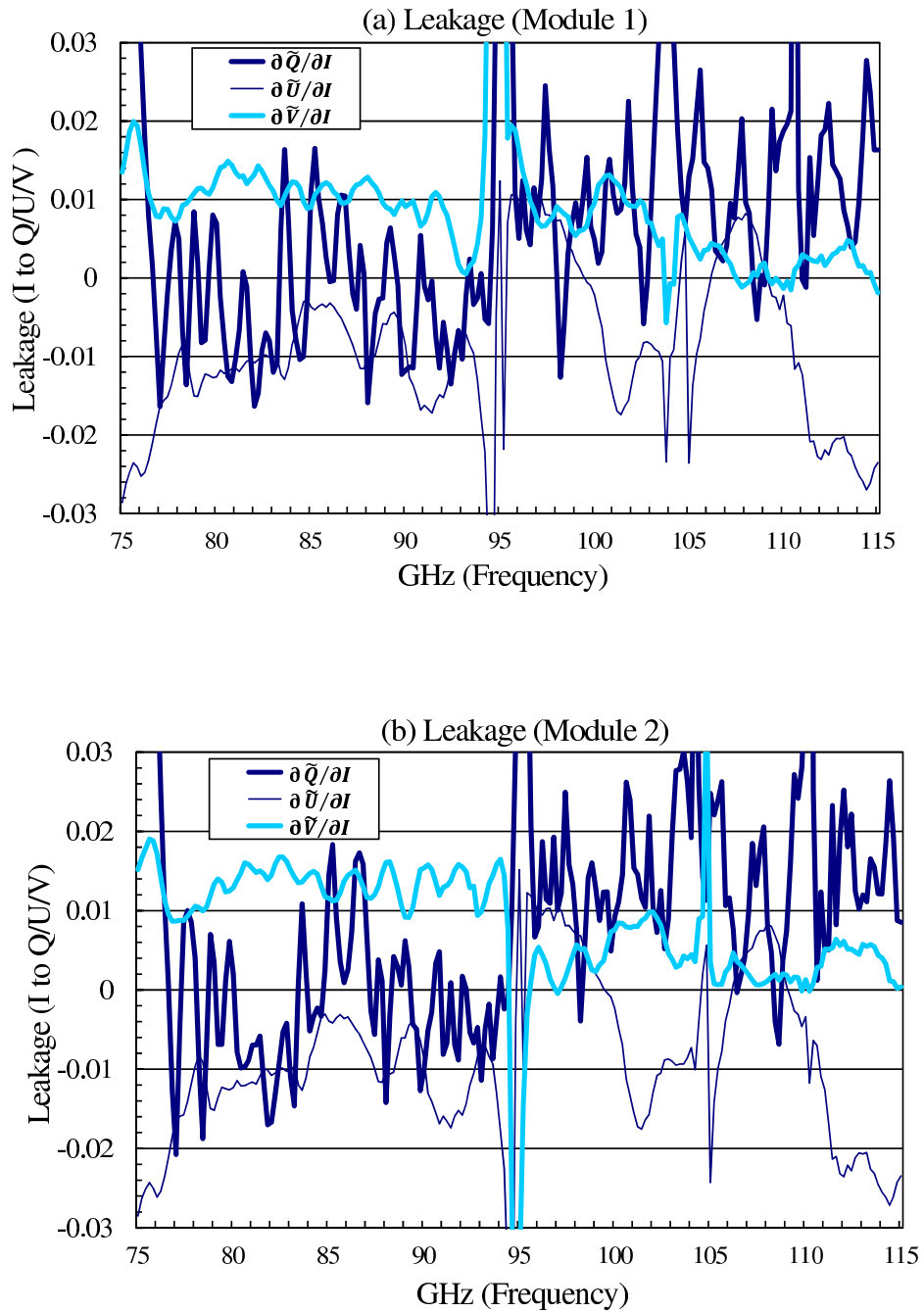


Figure 3.4: The measured leakage from Stokes I to polarized components, $(\partial\tilde{Q}/\partial I, \partial\tilde{U}/\partial I, \partial\tilde{V}/\partial I)$ for the two modules (a) and (b). The partial differentiations are taken on Eqs. (5.4), (5.5) and (5.6).

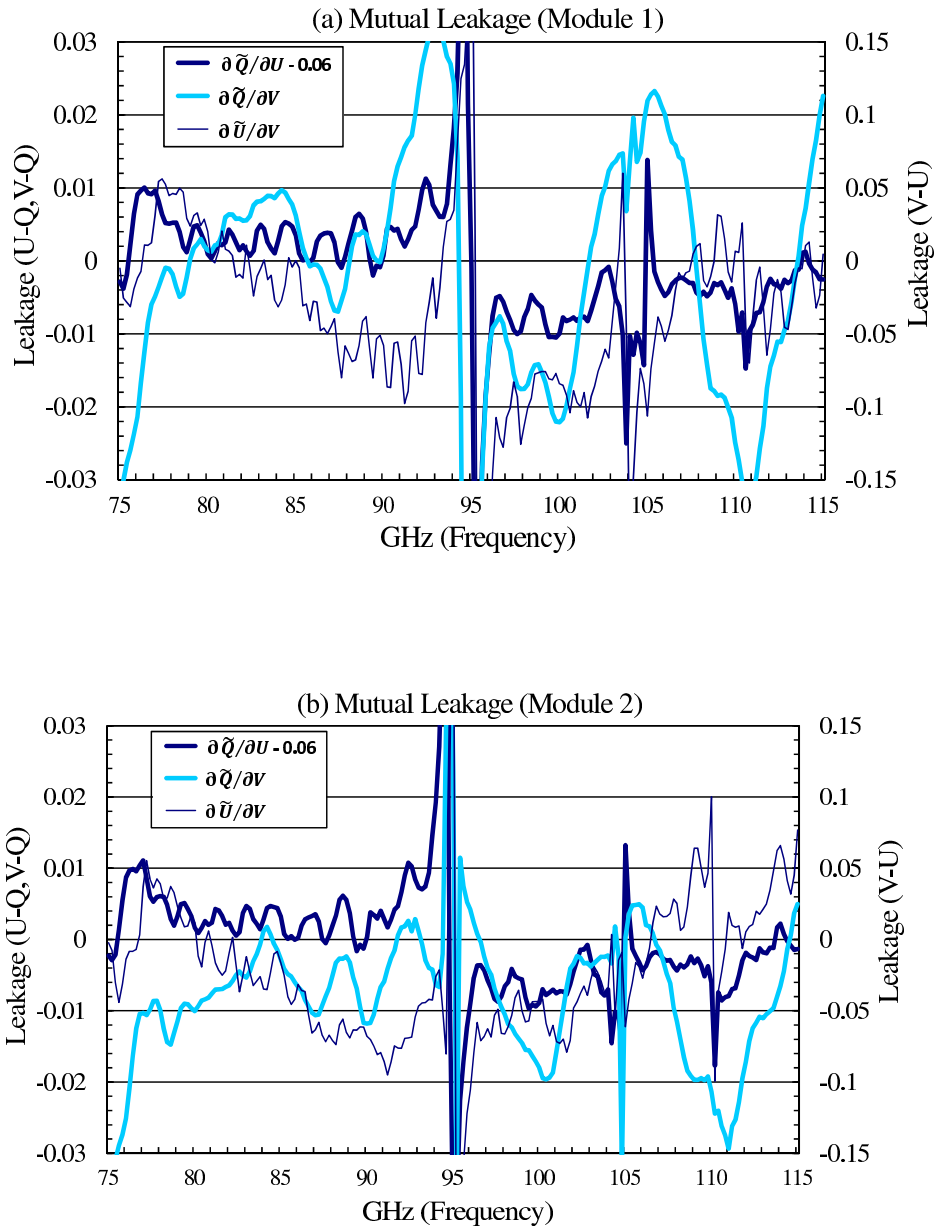


Figure 3.5: The measured leakage among the polarized components Q , U and V for the two modules (a) and (b). The $Q - U$ mutual leakage has a major contribution from the axis misalignment of the measurement adapter, and the resulting phase error has been corrected in this figure. Note that the $V - U$ leakage is a few times larger than others.



Table 3.1: Summary of W-band Polarization Leakage

Leakage	77-95 GHz	95-115 GHz
I to Q	1% ~ -1%	2% ~ 0%
I to U	0% ~ -1%	1% ~ -2%
I to V	1.5% ~ 0.5%	1% ~ 0%
Q to U	0.5% ~ 0%	0% ~ -0.5%
Q to V	0% ~ -1%	0% ~ -2%
U to V	0% ~ -8%	5% ~ -8%

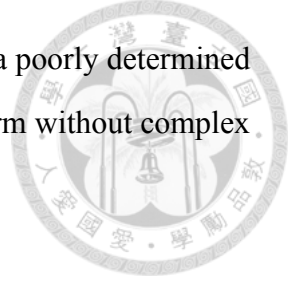
3.1.6 Calibration for removing Stokes I

Given the polarization leakage, a telescope can calibrate and remove leakages from the Stokes I, the much stronger, unpolarized component. Again, taking the simple case of a radiometer, where the single receiver outputs, $G_R E^R$ and $G_L E^L$, can be correlated to obtain the four Stokes parameters. But G_R and G_L are now complex gains, including system phase delays. A perfect receiver gets a finite value of Stokes I and zero values for other Stokes components with an unpolarized source. Non-zero values in other Stokes components represent the instrument leakage in a real system.

Exposed to an unpolarized source of known temperature, we can obtain the magnitudes of G_R and G_L from the power measurements of the two outputs, $|G_R E^R|^2$ and $|G_L E^L|^2$. Determining the relative phase between G_R and G_L is tricky, requiring a variable delay to alter the relative phase between $G_R E^R$ and $G_L E^L$. For a finite bandwidth source, the delay cross-correlation between $G_R E^R$ and $G_L E^L$ create fringes with an amplitude modulation as a function of the delay. The zero-delay between G_R and G_L is one condition that both amplitude modulation and fringe are the maxima. When calibrating with frequency resolution, digitization of data is required to determine complex gains per frequency, $G_R(\nu)$ and $G_L(\nu)$. We can thus measure complex gain to high precision in a well-controlled laboratory. Unlike the VNA measurement results having spurious resonances, the receiver using feed horns is resonance-free, and thus we can fully determine the non-zero coefficients in equation 3.4a, 3.5a, and 3.6a.

Next, having the complex gain, we can perform the calibration in the sky field and subtract the Stokes I leakage from the observed, polarized components. However, removing

I to V leakage is difficult due to the gain fluctuations, and therefore, a poorly determined Stokes V is expected. We write equations 5.4 and 5.5 to a simpler form without complex gain, and consider the variation of Stokes I:



$$Q = a_1(I + \Delta I) + a_2Q + a_3U + a_4V \quad (3.8a)$$

$$U = b_1(I + \Delta I) + b_2Q + b_3U + b_4V \quad (3.8b)$$

Where a_1 - a_4 and b_1 - b_4 are the coefficients in equation 5.4 and 5.5, ΔI implies the uncertainty of measured Stokes I. If I to Q/U leakage, a_1 and b_1 , is $O(\eta)$ (for example, 2% in Table 2), after calibrating, we can determine the leakage to $O(\eta^2)$ order.

The accuracy of Stokes I, ΔI , now places a limit on the second-order calibration. In the sky field, where other three Stokes parameters are much smaller than Stokes I by a factor of $O(\delta)$, with $\delta \ll 1$. The a_2Q and b_3U are equal to $O(\delta)I$. To identify the Stokes Q/U, $a_1\delta I$ and $b_1\delta I$ should be at least $O(\delta/10)I$. For example, assume that we have detected the weak linear polarization signals with S/N= 10, the Stokes I must have already been measured with a high S/N of about $O(10/\delta)$. With a measurement error of order $\delta/10$ in Stokes I, we can remove $a_1\Delta I$ and $b_1\Delta I$, from $O(\eta)$ to $O(\eta/10)$. Although the residual is not as small as $O(\eta^2)$, it is still much smaller than the polarization mutual leakage $O(\eta)$. We cannot deduce the mutual Q-U mutual leakage by the leading-order calibration since Q and U are weak with a relatively low S/N, unlike the strong I. It is, therefore, up to the performance of the polarizer to limit the leakage. In our case, the Q-U mutual leakage is $< \pm 1\%$.

In sum, after the leading-order removal of the Stoke I leakage, the polarized components can be made accurate up to order $O(\eta)$. Higher-order calibration is possible with even deeper integration, provided that the receiver system is sufficiently stable.

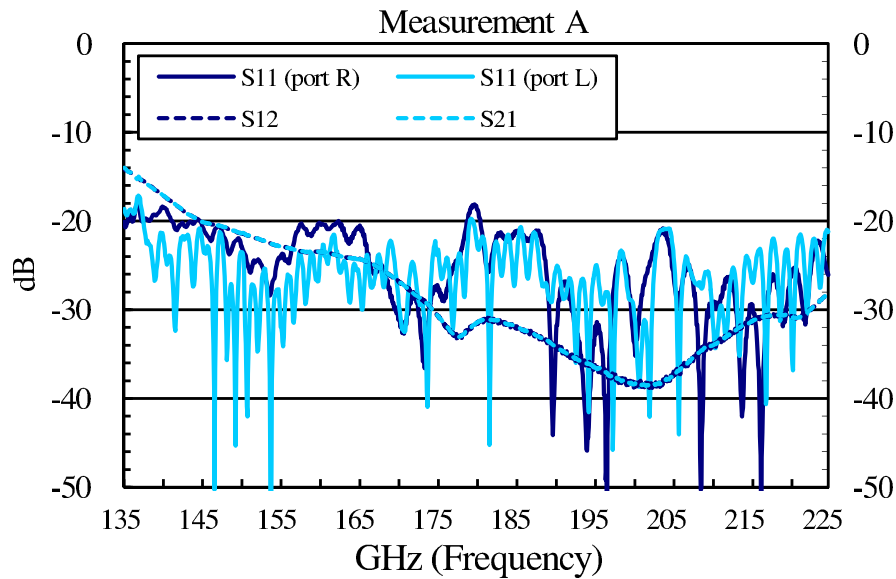


Figure 3.6: Measurement A of 140-220GHz polarizer.

3.1.7 D-band and G-band Results

For higher frequency applications, we develop a D-band polarizer and a G-band polarizer, both of which provide comparable performance to W-band. We start with a scaled version of the W-band polarizer. Because the septum machining based on the wire-electrical cut requires a fixed radius angle at each corner, the scale symmetry breaks and thus we need to optimize the septum again. The radius angle (R-angle) is 0.07-0.1 mm. We apply the same procedures, including measurement A, measurement B, and polarization leakage to identify the two polarizers, shown as follows.

The figure shows measurements of a D-band polarizer. The D-band polarizer based on a circular waveguide of 1.6mm diameter has an excellent performance in 124-142 GHz and moderate function extending to 142-165 GHz, given 31.3% bandwidth. We design the D-band polarizer for Korea VLBI Network (KVN). In D-band polarizer, we give further result for the 90 degrees issue. Due to the waveguide twister, it is challenging to measure the exact phase difference of E_x to E_y . For example, our W-band polarizer yields relatively high U-V mutual leakage, ranging from 0-8%, mostly +5%, which implies the axial ratio and how perfect the 90 degrees is. Though the septum polarizer is in favor of linear polar-

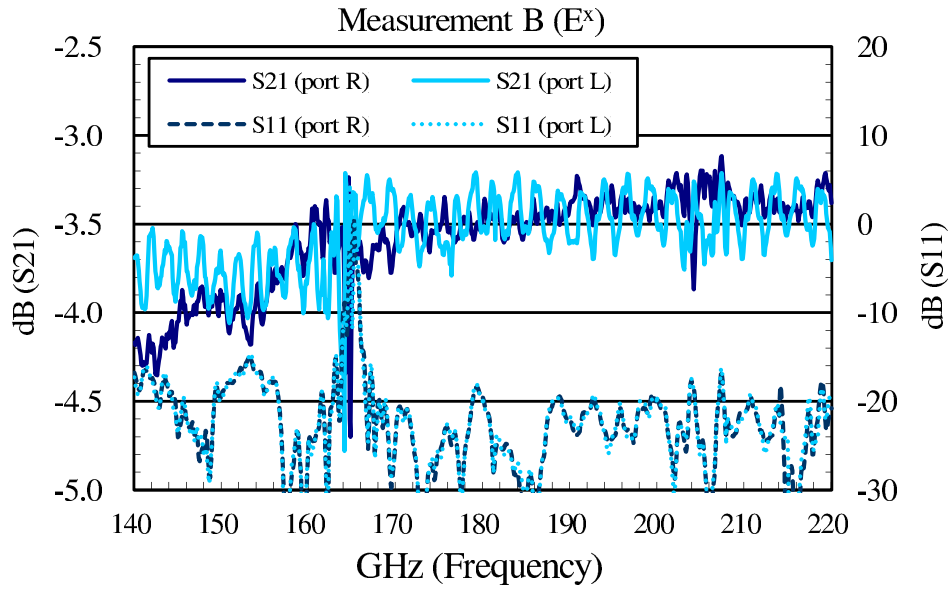


Figure 3.7: Measurement B(E^x) of 140-220GHz polarizer.

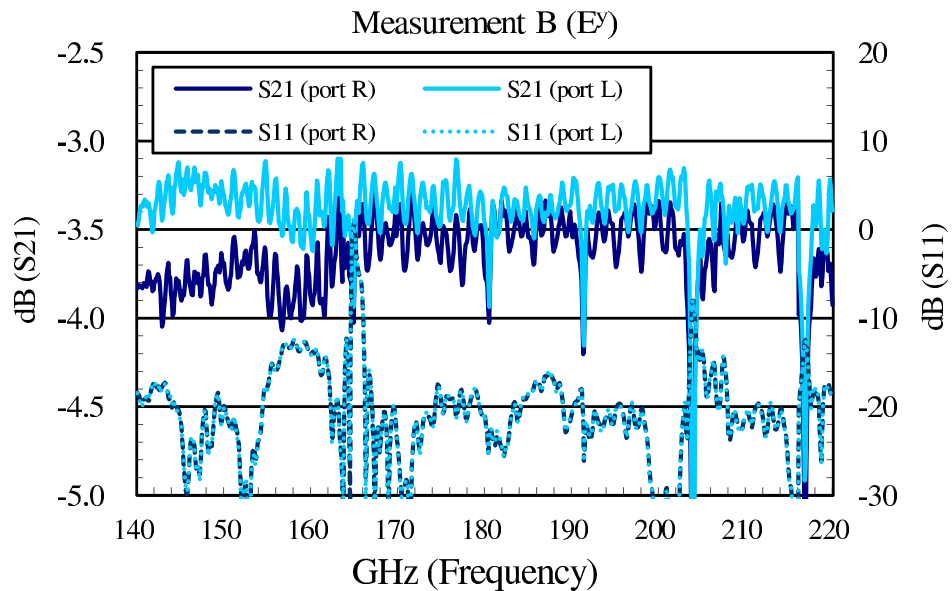


Figure 3.8: Measurement B(E^y) of 140-220GHz polarizer.

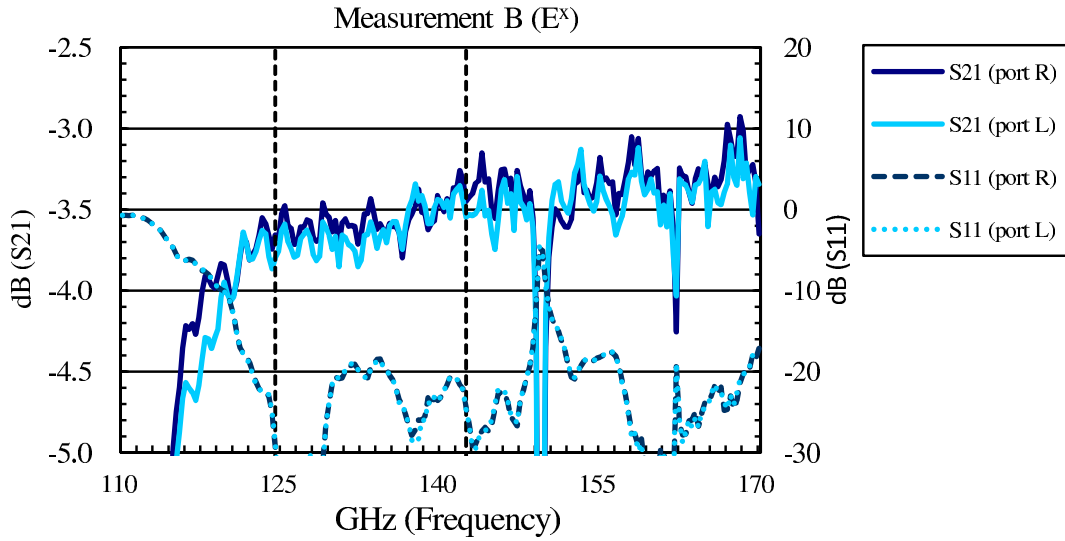


Figure 3.9: Measurement B(E_x) of 110-170GHz polarizer.

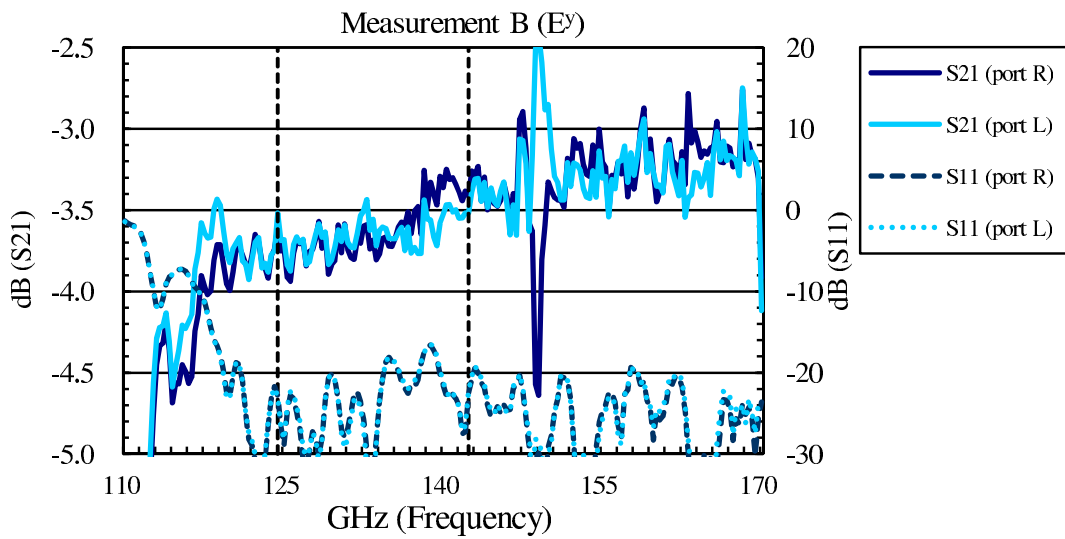


Figure 3.10: Measurement B(E_y) of 110-170GHz polarizer.

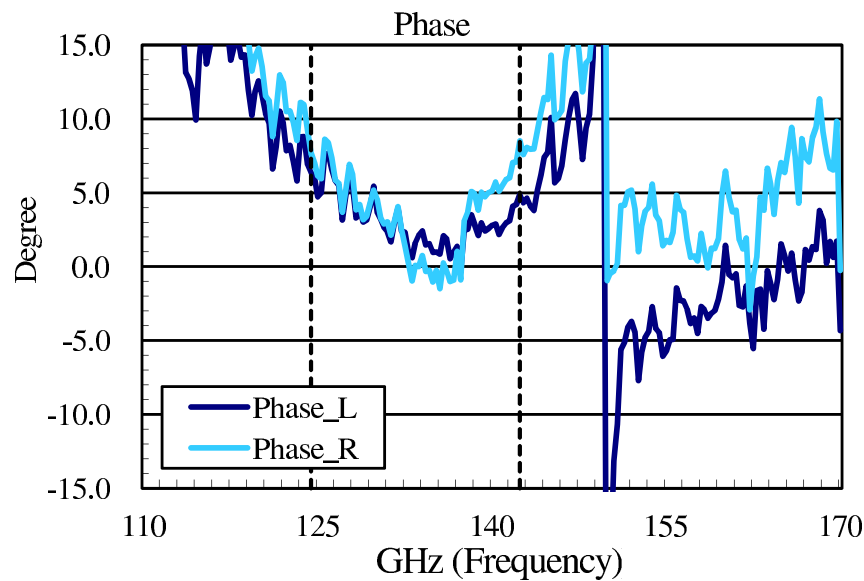
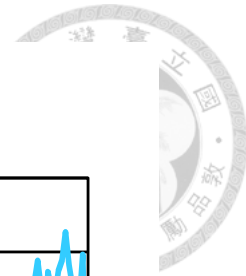


Figure 3.11: Phase deviation of 110-170GHz polarizer.

ization and we assume very weak Stokes V component in observation, the U-V leakage remains an issue. We aim to improve the axial ratio for the circular polarization detection, such as the electrical vector position angle calibration (EVPA calibration), which requires precisely 90 degrees between RHP and LHP [70]. The figure shows a better axial ratio of D-band polarizer, representing $<0.5\text{dB}$ in 128-142 GHz and 150-160 GHz. In the figure, we give the polarization leakages of D-band polarizer.

The figure shows the results of a G-band polarizer covered 165-220 GHz. The noisy-like response in S21 is due to the long waveguide components while calibrating. The figure shows the polarization leakage of G-band polarizer. Because lacking a 90-degree twister in VNA measurements, we didn't have the U-V leakage for the G-band case. We conclude the results in Table. The figure gives the phase information of W-band polarizer and D-band polarizer. The phase difference reveals the essential data, and therefore we can convert them to polarization leakages from equations.

The ability to extend from W-band to G-band with conventional precision machining demonstrates that this polarizer is relatively uncomplicated to manufacture, and we have currently used the same manufacturing method to push it to even higher frequencies to



Table 3.2: Summary of D-band Polarization Leakage

Leakage	124-142 GHz	143-170 GHz
I to Q	2% ~ 0%	3% ~ 0%
I to U	2% ~ 0%	3% ~ 1%
I to V	1% ~ 0%	1% ~ 0%
Q to U	3% ~ 2%	0% ~ 2%
Q to V	0% ~ 1%	0% ~ 1%
U to V	0% ~ 8%	5% ~ -5%

Table 3.3: Summary of G-band Polarization Leakage

Leakage	140-165 GHz	166-220 GHz
I to Q	3% ~ 0%	2% ~ 0%
I to U	1% ~ 4%	3% ~ 2%
I to V	0% ~ 4%	0% ~ 1%
Q to U	0% ~ 4%	0% ~ 4%
Q to V	0% ~ 2%	0% ~ 2%

test the limit.

3.2 Discussion of Cryogenic LNA Housing

In section 3.2.1, we introduce the amplifier-based detector and bolometers and give a sensitivity comparison. In 3.2.2, we discuss the simulation and measurements of alumina probes. The technique of the amplifier housing, including the epoxy and wire bonding, is given in 3.2.3.

3.2.1 Comparison of Amplifiers and Bolometers

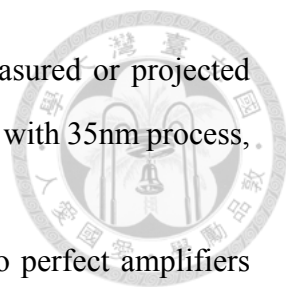
The coherent and incoherent detector are two competing devices using for telescopes, especially the CMB experiments. The frequency of CMB anisotropy spans from radio to infrared band. The amplifier-based, coherent detector is suitable for radio to sub-millimeter wave, and the bolometer, the incoherent detector is applied to infrared, optical, and higher frequencies. The choice of detectors determines the type of telescopes.

Currently, the CMB polarization-capable telescope tends to employ bolometers, such as BICEP2 in 150GHz. The characteristic of bolometers has the potential for extremely low noise. Above a particular frequency, the bolometer system can achieve lower noise than the coherent system, due to that an amplifier has a linear dependence of quantum noise on frequency. The noise temperature at quantum limit is defined as $q_T = h\nu/k\log 2 \sim [\nu(\text{GHz})/20]K$.

The amplifier-based detector still has advantages. For example, the amplifier provides the lowest noise at a relatively high cooling temperature, 20K. The amplifier is inherently a band-pass device that filters unwanted noise. Moreover, the amplifier has a large dynamic range, broad temperature operation, and is insensitive to cosmic rays and microphonics. These advantages reduce complexity and cost of the coherent system. In comparison, bolometers must be the final device of the detector chain, and therefore any optical inefficiency and surrounding noise directly reduce the sensitivity.

The figure given by C.R. Laurenz in 2009 [65], shows the comparison of the sensitivity for amplifiers and bolometers, where the x-axis means the frequency in GHz. The y-axis denotes the noise equivalent temperature (NET) of Stokes Q/U, in $\mu K s^{1/2}$. The black solid curve indicates a perfect quantum-noise-limited amplifier at the quantum noise level, and the dashed curve means a perfect photon-noise-limited bolometer with 100% optical efficiency. The sensitivity calculation assumes a 25% bandwidth. Since the amplifier can measure Q and U simultaneously through a single feed, its sensitivity includes a factor of $1/\sqrt{2}$. In comparison, the bolometer that directly detects photons measures only Q or U at one time. The rise and down of curves represent the atmospheric windows and absorptions (See Laurenz 09 and Zmuidzinas 03 for sensitivity calculations).

The horizontal line sets the detectable limit. While a 512-feed telescope equipped with detectors reach 100nK per square degree in the 4% of the sky, with the lowest foreground levels, the horizontal blue (green) line indicates the sensitivity of a detector required for one year (4 years) integration, from the ground. The rms polarization temperature of 100nK implies the criterion of B-mode detection (the figure). A real amplifier provides more noise than the quantum noise, and hence the blue (red) dash line defines an amplifier



at three (five) times the quantum limit. Discrete points denote measured or projected sensitivity of experiments, including MIC amplifier, MMIC amplifier with 35nm process, QUIET amplifier, BICEP, and BICEP2.

From the figure, the sensitivity of perfect bolometers is equal to perfect amplifiers around 130GHz and better than that around 220GHz. Below 120GHz, the amplifier is favorable. We further conclude that using a 100GHz amplifier with the noise temperature of 100K, five times the quantum level, 20K, a 512-pixel telescope can achieve 100nK between one and four years, a reasonable time. If we apply the 35nm gate HEMTs, the integration time reduces to one year.

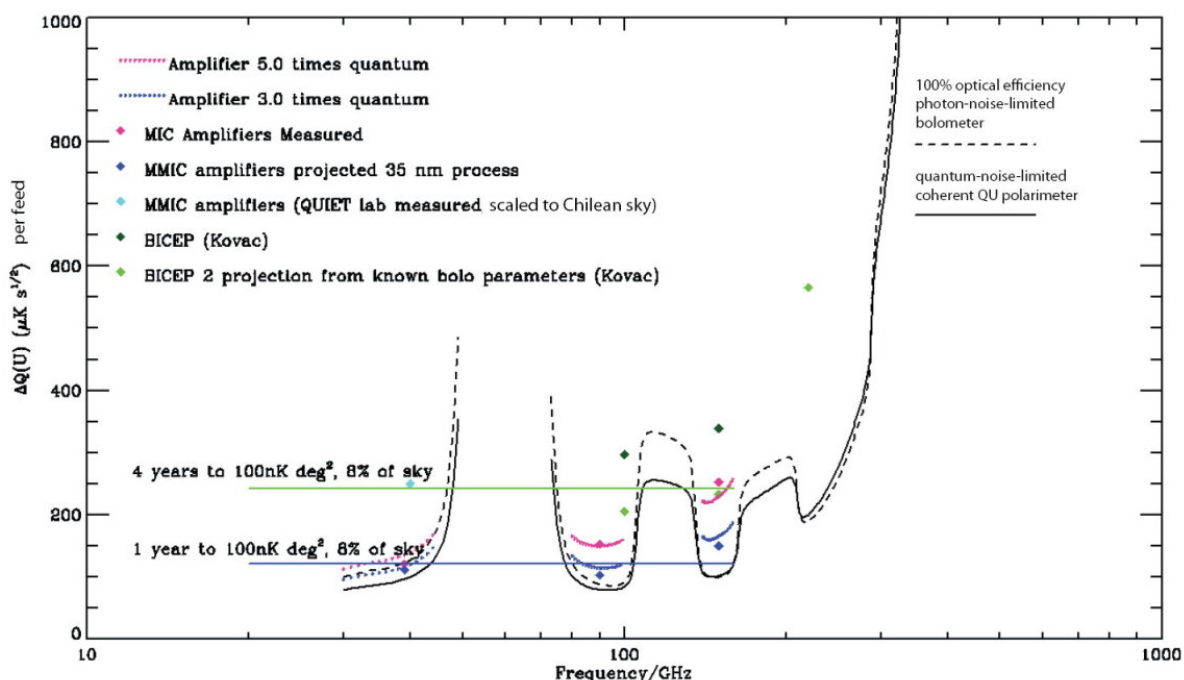


Figure 3.12: Sensitivity comparison of amplifiers and bolometers.

3.2.2 Waveguide to Microstrip line Transition

Packaging and integrating microwave circuits usually require a waveguide to microstrip line transition to connect waveguides and circuits, since the waveguide is a low-loss device applied in radio frequencies [96] [81]. Furthermore, for the lack of connectors in sub-millimeter and terahertz frequencies, most test equipment is waveguide-based. The E-plane probe is widely used among various transition probe designs. The figure lists

examples of E-plane probe [69] [71] [55], in which a microstrip line inserted through the E-plane of a rectangular waveguide couples TE_{10} mode the quasi-TEM mode of the microstrip line. Typical examples include the probe A and probe B, in which the surface of the microstrip line lies on the E-plane. The probe C is another design similar to the E-plane probe, where the surface of the substrate faces to the propagation direction, but the center of the transmission line still coincides the E-plane. Thus, we further refer probe A to face-on, and probe B and C to edge-on, according to how the substrate surface put related to the incoming wave. For face-on and edge-on probes, Leong's study provided comprehensive studies, including the substrate of four dielectric constants ($\epsilon_r = 2.2, 6.0, 10.1, \text{ and } 13$) [69].

These E-plane probe designs have comparable performance. The selection of face-on or edge-on depends on which surface the chips placed. Each telescope can adopt a suitable one for its instrument setting. For example, the bolometers and QUIET experiment apply face-on E-plane probes, because their receiver has compact detectors distributed on a large area for receiving light. The amplifier-based telescope that integrates amplifiers independently to each channel, using edge-on E-plane probes. The input port of the E-plane probe is usually perpendicular to the output port, and hence it requires a waveguide bender, making the device cumbersome. In recent years, the H-plane probe is developed to solve this issue, such as the inline transition adopted a ridge-waveguide to microstrip junction [119] [89].

The figure shows the schematic of the transition probe design. One end of the alumina microstrip is inserted into the waveguide's broader wall, through an air-channel. It picks the energy at the $\lambda/4$ position from the back-short, in which λ is the waveguide wavelength. The back-short means a waveguide wall at the terminal where the circuit shorted. The other end of the alumina probe has a particular design, matched to amplifier pads for wire bonds. The air-channel, where the alumina probe located, gives a cutoff frequency that forbids waveguide modes and allows only the microstrip quasi-TEM mode propagated inside. The channel width and height are therefore required small enough. For the alumina probe design, its performance is sensitive to the position and dimension of the

substrate. While we manually operate the alumina probe, a tiny error may cause problems. Hence, it is essential to consider the overall tolerance in the EM simulation.

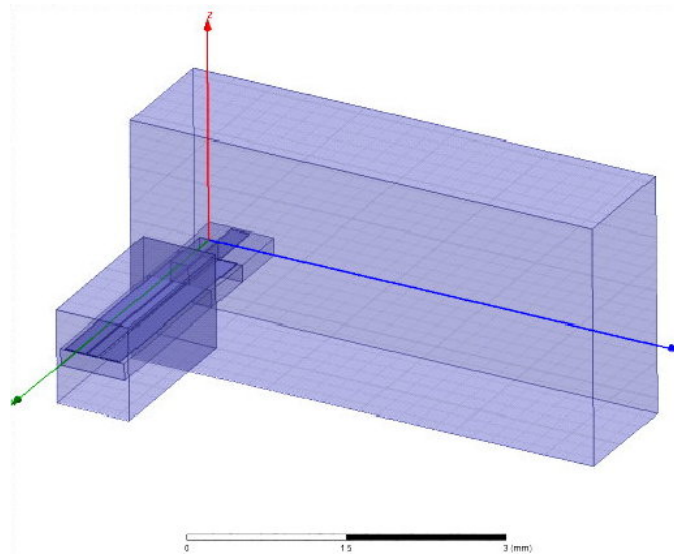


Figure 3.13: Schematic of the transition probe design.

3.2.3 Simulation of Transition Probes

The simulation of alumina probes based on the back-to-back design contains two waveguide outputs is robust while setting the excitations. We can easily conform simulated results with the VNA measurements. The simulated results include the connected probe without wire bonds, shown in the figure 1a-1c, and the separated probe with wire bonds, shown in the figure 2a-2c. At the fixed channel height of 0.527mm, the figure 1a gives how the performance changes related to the channel width of 0.3, 0.4, 0.5, 0.6, 0.7, and 0.8mm. It reveals that increasing the width degrades S21 at high frequencies, and too narrow width came with a little decline of the overall S21. Here the channel width is the same as the substrate. Thus we can determine the optimized probe width, about 0.6mm.

The figure 1b gives the result with changes of the channel height, from 0.254mm to 1.016mm, meaning two to eight times a probe thickness, where the channel and probe width are both fixed at 0.6mm. The result shows a resonance at high frequencies, and increasing the channel height will move the resonance from 120GHz to 115GHz. The amplifier housing is hence a cavity issue. We can change the dimension of the channel

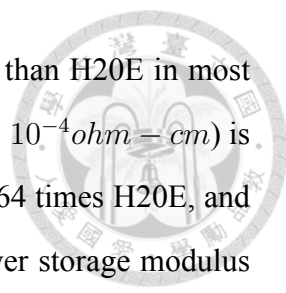
and probes to adjust or remove the resonances.

The figure 1c gives how the electrical resistance effects the result, where the resistance of 10^7 , 10^6 , 10^5 , 10^4 , and 10^2 siemens/m (S/m). The channel width is 0.6mm, and the height is 0.482mm. While the probes attached, the contact resistance will increase the effective electrical resistance. In the simulation, the resistance of 10^7 , 10^6 , 10^2 S/m implies approximately gold, stainless steel, and carbon, respectively. The result shows a high dependence of the resistivity, and the S21 falls toward high frequencies. Because the resistance of silver adhesives is 10^5 - 10^6 S/m, such as H20E that has 2.5×10^5 S/m, the silver adhesives will provide an additional insertion loss of 0.5-1.5dB.

3.2.4 Silver adhesives

Conductive adhesives provide an efficient way to place and attach housing electric devices. These are usually A/B part adhesives, in which the two components contain silver particles but different epoxy content. Silver particles give electric conduction for the grounding of dies, and the thermal conduction of adhesives takes the heat of active devices away. While mixed and heated, these thermosetting epoxies locate the chip. More importantly, the adhesive tolerates the tensile stress forced on the InP based GaAs substrate at the thermal cycle. The table lists the essential parameters and examples of housing materials. The housing materials include brass and aluminum, and the substrate materials include InP, GaAs, alumina, and quartz. At room temperature, brass has CTE of $19 \times 10^{-6} K^{-1}$, aluminum has CTE of $23 \times 10^{-6} K^{-1}$, and the GaAs substrate has CTE of $5.8 \times 10^{-6} K^{-1}$. Because the housing CTE is larger than the substrate, the semiconductor-based substrate imposed a compressive force during the cooling cycle, resulting in joint layers bending and a possible fracture. The study reported the tensile stress of 50 MPa for the InP chip on Al6061 [109], and hence the adhesive buffer layer is required to absorb the strain. The figure shows how the multi-layer bends at cooling.

We take H20E and H20F as examples of how to consider the buffer material. The two epoxies, both provided by Epotek, have different characteristics, such as CTE, electric resistivity (ρ), thermal conductivity (K), adhesive property, stress absorption, and viscos-



ity. Roughly speaking, H20F is more conductive, softer, and, better than H20E in most properties. For comparison, the electric resistivity of H20F ($\rho = 1.0 \times 10^{-4} \text{ ohm} - \text{cm}$) is 0.25 times H20E, the thermal conductivity of H20F (4.10 K^{-1}) is 1.64 times H20E, and the storage modulus of H20F (21153 psi) is 0.026 times H20E. Lower storage modulus implies that the solid part of epoxy is less elastic and softer, and therefore H20F can absorb more tensile stress than H20E. However, the die shear strength of H20F (680 psi) is 0.4 times H20E, which means components applied soft H20F can be easily removed after thermosetting. Since MMIC chips usually require bond wires, low adhesive strength epoxy is unstable when the bonding tool gives ultrasonic forces on the substrate. Therefore, most housings applied H20E that has good adhesive strength and medium value of other properties. H20E has CTE of $31 \times 10^{-6} \text{ K}^{-1}$ at room temperature, acting a buffer when the cooled housing compresses chips. The study suggested that thicker adhesive, in which the thickness is 20-50 μm , is safer for the cooled housing [23].

3.2.5 Impedance of Wire bonds

Wire bonding is the standard method that interconnects an MMIC, PCBs, and electronics. The bonding techniques include the ball bonding and the wedge bonding, where the bonding machine provides an ultrasonic power and force, through the capillary of a bonding tool, to a metal wire. When the metal wire contacts the heated sample about 120 degrees, the ultrasonic power will make the wire melt and connect to pads. We employ the wedge bonding, in which the 25 μm diameter gold wire is for bias pads, and the 25 \times 75 μm ribbon gold wire is for signal pads. The ribbon wire bonding is essential for LNA housing because it controls the input/output port's performance and requires low-loss in full-band.

The figure shows that a bonding wire design acts as a low-pass circuit, in which a single bond-wire is a series inductor, and the two signal pads are shunt capacitors [1]. The pad capacitance is usually 50-100 pF in 100GHz, depending on the pad size, which gives much lower impedance than 50ohm. The wire length determines the inductance and the electrical resistance, and hence the bonding wire has more influence on circuits. The cavities between wires, pads, and ceiling also contribute parasite capacitances. Therefore,

we can modulate each content of the RLC low-pass circuit to improve the bonding wire performance. We expect the wire inductance is approximately 80pH, given an impedance of 50ohm in 100GHz, the same as matched probes and chips.

We can calculate the inductance of a single bond wire, from the equation based on the airbridge inductance that implies the area of the loop [42]

$$L_{single_wire}(nH) = (5.08 \times 10^{-3}) \times L \times [\ln(4 \times L/D) - 1] \quad (3.9)$$

Where L and D are length and diameter in mils. For 25um diameter and 1mm length wire, the inductance is 0.81 nH. The bond wire inductance is roughly proportional to the length, and hence the 80 pH wire has 100um in length. That short length is difficult for the ball bonding, where the minimum bonding length is about 500um. We thus employ wedge bonding and ribbon wires.

The equation gives the inductance of a rectangular strip of ribbon [118]

$$L_{ribbon}(nH) = (5.08 \times 10^{-3}) \times L \times [\ln[(L/(W+T))] + 1.19 + 0.22 \times [(W+T)/L]] \quad (3.10)$$

Where L, W, and T mean length, width, and thickness of ribbons in mils. For a 25x75 um ribbon wire and a reasonable 200um length in wedge bonding, the inductance is 79.9pH. Besides, if without ribbon wires, there is an alternative way to use two parallel wires. Because of the mutual inductance, the two parallel wires have only 30-40% of a single wire inductance.

3.2.6 Simulation of Bond Wires

Figure 2 shows the back-to-back result of bond wires, in which the probe is the same as figure 1 but cut at the center and connected by wires. In f2a, with 20um separation of two probes, we simulate the 25X75um ribbon wire with different wire lengths, from 40um to 240um. The results show that a shorter length gives better performance. While the wire length is <120um, the insertion loss is below 0.7dB in 75-115 GHz and the S21 is very

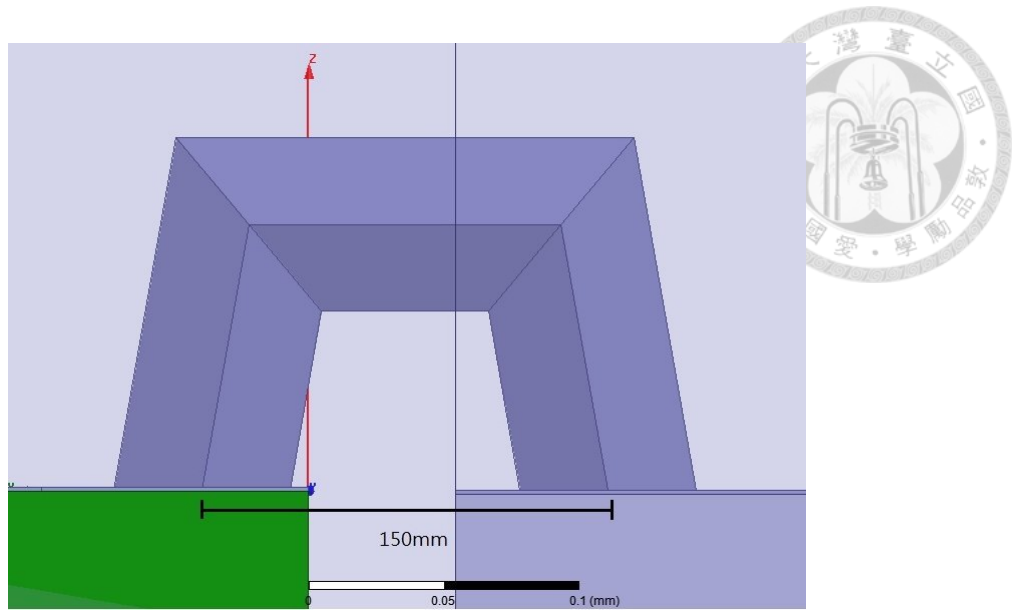
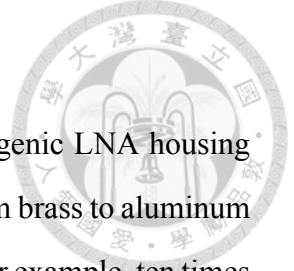


Figure 3.14: Schematic of the bond wire.

similar, implying the matched bonding wires. We thus set the optimized ribbon bonding length to 120 μ m. In our wedge bonding, we maintain the maximum wire length for signal pads is 150 μ m.

In f2b, with the same B2B arrangement, we add the ground pads to transition probes, in which the ground pad will be applied to connect the MMIC chip in LNA housings. The probe with ground pads is similar to the original probe, but if the bond wires are attached, the insertion loss will increase about 0.5dB. We keep the same wire length of 120 μ m, and just change the separation of two probes, from 20 μ m to 90 μ m, and the result reveals that the 90 μ m case gives more 0.5dB loss compared to 20 μ m. Therefore, besides the shorter wire length, we should keep the space between probes and chips as close as possible.

Figure 2c shows the simulation of different transition probes employed a ribbon wire, a single 25 μ m wire, two wires, and three wires. Here the wire length is 120 μ m, the separation is 20 μ m, and both ground pads are connected. The result has the same conclusion in 3.2.6. Compared to the 25 \times 75 μ m ribbon wire, a single 25 μ m gives an additional loss of 0.6-0.8dB, and two parallel 25 μ m wires reduce the extra loss to 0.2dB. More importantly, three 25 μ m wires arrive at an identical performance as ribbon wire. Because only a particular wedge bonding machine can locate the ribbon wires, we can use parallel round wires as an alternative method.



3.2.7 Cryogenic LNA Housing for Receivers

Referred to the two-chip housing design, we can develop a cryogenic LNA housing for the multi-pixel receiver. First, we change the housing material from brass to aluminum 6063 T5 since Al 6063 has a higher thermal conductivity than brass, for example, ten times brass at 20K. The aluminum housing is plated with gold and nickel to avoid oxidation, where nickel is a buffer layer for plating. The thickness of gold is 1.4 μ m, six times its skin depth, 0.236 μ m (100GHz), and the nickel thickness is 1.8 μ m. Second, the cryogenic housing must contain four LNA chips for the dual-polarization, two for an RHP signal and the other two for an LHP signal. Moreover, the housing has a small size, only $20 \times 20 \times 30\text{mm}^3$, and hence suitable and expansible for multi-pixel integration.

Third, the four LNA chips will give many biases and thermal loads, making the bias circuit and the heat strap arrangement more complicated. We apply a Teflon insulated wire, which is penetrated through a 1mm diameter hole on the housing for connecting biases from the outside to the inner side. A Teflon wire with a diameter of 0.15mm is soldered on FR4 boards. The multi-pixel LNA integration requires a small and compact connector, and hence we employ a 15 pin strip connector, provided by TE Connectivity, in which the size is $1 \times 5 \times 10\text{mm}^3$. The strip connector is smaller enough to be put in the space between circular waveguide flanges, and thus its wires can reach the receiver vacuum feed through.

Finally, each cryogenic housings is fixed side by side, with two M2.5 screws, and formed an LNA block. Hereafter, we connect heat straps on the side of LNA blocks for thermal anchors. The heat strap is oxygen-free copper straps plated by tin, and its cross-dimension is $3 \times 15\text{mm}^2$.

3.3 Development of Faraday Rotation Isolator

3.3.1 Introduction to Faraday Rotation

Up to now, the millimeter-wave components discussed are all reciprocal devices, where the reciprocal means symmetric S-parameter matrix, $S_{ij} = S_{ji}$, and i and j are any two

ports. On the contrary, the Faraday rotation isolator is an interesting non-reciprocal and two-port device that provides transmission at one port and isolation at the other port. The asymmetric S-matrix is due to the ferrite materials, in which the electron spin produces the magnetic dipole moment. While we apply an external magnetic field H_0 , the magnetic dipole moment of ferrites will rotate along the axis of magnetic field direction, named the Larmor precession, and the equation of motion is [88]

$$dM/dt = -\mu_0\gamma M \times H \quad (3.11)$$

Where H is the internal applied field, M is the magnetization, μ_0 is the permeability of free space, and γ is the gyromagnetic ratio. According to the hysteresis loop, the magnetization M is in proportional to the strength of the external bias field H_0 . For the ferrite saturated with a magnetization M_s and an external magnetic field H_0 , the input EM wave is a small AC magnetic field, which adds a perturbation term. Thus the total magnetic field H_{total} is $H_0 + \tilde{H}$, and the total magnetization M_{total} is $M_s + \tilde{M}$, where \tilde{H} and \tilde{M} imply the AC term produced by an EM wave. Put H_{total} and M_{total} into the procession equation, we can have the relation of \tilde{H} and \tilde{M} , the tensor susceptibility $[\chi]$, which gives a non-reciprocal property.

According to the right-hand or left-hand circular polarized AC field, a magnetic dipole inside a saturated ferrite has a different forced precession. Referred to a favorable precession direction given by the bias field, an RHCP wave causes the dipole to precession in the same direction. An LHCP wave causes the opposite direction. Therefore, RHCP and LHCP plane waves in the biased ferrite medium have different propagation constant. We can represent a linearly polarized field as the sum of an RHCP wave and an LHCP wave, and the linear polarization will rotate while propagating in the direction of the applied magnetic field. This effect is named the Faraday rotation. In the presence of a very small applied magnetic field, the Faraday rotation equation becomes equation (2.4), verified by Hogan [44].

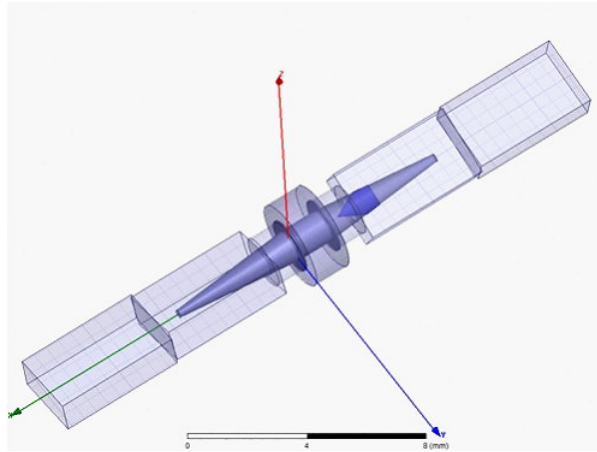
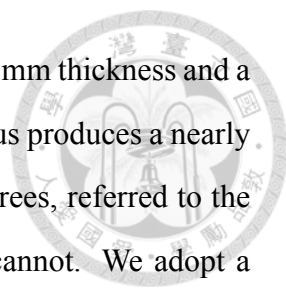


Figure 3.15: Schematic of the Faraday rotation isolator.

3.3.2 Dielectric components

The ferrite rod in the isolator gives the Faraday rotation. Since the rotation angle is proportional to the ferrite length, we require a ferrite with low-loss, high saturated magnetization, and a steeper slope of the hysteresis curve. With the hysteresis curve, a small applied H_0 field can fully saturate the ferrite. Trans-Tech TT2-111, made of Ni-Zn ferrite, has $\epsilon=12.5$, loss tangent <0.01 , and high saturation ($4\pi M=5000$ gauss) at 10GHz, and hence suitable for millimeter-wave instrument. Trans-Tech TT86-6000 is similar to TT2-111 but has a smaller loss tangent (<0.002). The Faraday rotation angle is sensitive to the value of epsilon. According to equation 2.4, the ferrite length of 45 degrees rotation is 1.434mm for $\epsilon=12.5$ measured in 10GHz, and 1.35mm for $\epsilon=14.1$ measured in 70-100 GHz. Therefore, it is better to fine-tune the rotation on the unsaturated ferrite, with a longer ferrite length and a weaker H_0 field. We thus adopt the ferrite length of 1.78mm and the ferrite diameter of 1.17mm, in which the length-to-diameter ratio of about 1.5 creates a uniform internal axial magnetic field.

The alumina taper attached to the ferrite rod provides the impedance matching from air to the ferrite. The 99.5% high purity alumina ($\epsilon=9.4$) is the same as the material we apply in transition probes. The cone-shape alumina taper has an 11 degrees full angle, 5mm in length, and 1.17mm diameter at the bottom. The tip diameter of the alumina taper is 0.25mm. The magnetic field is supported by four common NdFeB or SmCo magnets,



which are surrounding the ferrite rod. Two silicon steel disks, with 0.5mm thickness and a small hole at center, contact the magnet pole. The magnetized disk thus produces a nearly uniform axial field. Now if the output waveguide is tilted by 45 degrees, referred to the input port, the input wave can pass through and the reverse wave cannot. We adopt a two-step waveguide twister to obtain 22.5 degrees rotation, which has 11.25 degrees tilt for each step. The milled waveguide has 0.5mm of the round angle at corners.

A resistive metal film embedded in the alumina taper absorbs the opposite propagated waves, giving the isolation. From the HFSS simulation, we find that the metal film with a volume resistivity, 0.1-0.13 ohm-cm, has 20dB attenuation. The value of 0.1 ohm-cm ($\sigma=1000$ siemens/m) is in the order of carbon, such as the carbon ink 124-50 (0.1 ohm-cm in maximum) and 120-24 (0.13 ohm-cm in maximum). However, tho of the carbon ink measured from the multimeter and the four-probe method reveals inconsistent results, 0.45 ohm-cm for 124-50 and 0.175 ohm-cm for 120-24. Besides, the physical dimensions of metal film require a specific shape and a thickness of 10um, for avoiding additional reflections. Hence, we employ a plated Ag-Pd film. The figure shows the metal film on half-cone alumina. The complete assembling requires four dielectric pieces, including an alumina cone, a half cone, a half cone with plating, and a ferrite rod. Putting these dielectric components in a Teflon housing, and a polymer glue cured at 100 degrees with 15 min combines them into one piece. A Teflon housing is non-adhesive to glues and thus helps to locate components.

3.3.3 Higher-mode suppression

While the wave propagated in isolators, the mode transition is from the TE_{01} rectangular waveguide mode to the HE_{11} hybrid mode [102]. The HE_{11} is the zero-order mode in a dielectric waveguide; it also exists in corrugated feedhorns and optical fibers. The field lines of HE_{11} hybrid mode is very similar to that of the TE_{11} circular waveguide mode, but the HE_{11} mode contains both E_z and H_z , where H_z is much stronger. The high epsilon alumina taper transforms the intense EM field lines of waveguide modes into the purely HE_{11} mode and fed it into the ferrite rod. However, alumina tapers permit higher-order

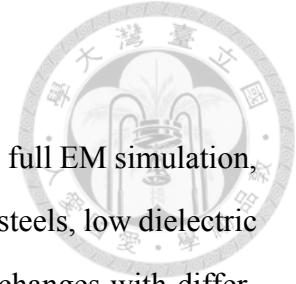
dielectric waveguide modes, up to sixth-order [30]. If there is a mode conversion from the TE_{01} mode to higher-order modes, the alumina taper will appear unavoidable resonances. The challenge is, therefore, to suppress higher modes and allow only the HE_{11} mode passed.

A circular waveguide put in the mode transition area can suppress high modes. From HFSS simulation, the circular waveguide has an inner diameter of 1.88mm and a length of 1.07mm, and it is surrounding the alumina taper. The final task is to design mechanical support for a ferrite rod and alumina tapers. The mechanical support will degrade the isolator performance, and hence the material has to be very thin, low-loss, and robustness. The traditional method is applying a Mylar film with a thickness of 0.08mm. We use a Teflon tube, in which the ferrite rod is penetrated through the tube's inner side and fixed with a little glue. There are still possible reflections between alumina and ferrites and additional losses from the unparallel magnetic field. An absorber encircled on the tube's outside surface is thus employed. For the issue of mode suppression, the Faraday rotation isolator is very similar to the LNA housing, in which the circular section in isolators and the air bridge in transition probes diminish the existing resonances.

3.3.4 Simulation of Faraday Rotation Isolator

For the isolator simulated in HFSS 13.0, we have to set the permeability and the saturated magnetization for the ferrite. However, if we apply $\mu > 1$, the software will require a lot of RAMs (random access memory), more than 64GB, which is due to the intense meshes in the transition area. To solve the issue, a method is using an HFSS option, named Distributed Domain Meshes, for that HFSS can automatically assign meshes to computer nodes in the networks. We have successfully employed the distributed domain method to calculate an isolator with four connected computers, one for a local machine and three for remote machines (The figure).

3.3.5 Electrical property at Cryogenic temperature



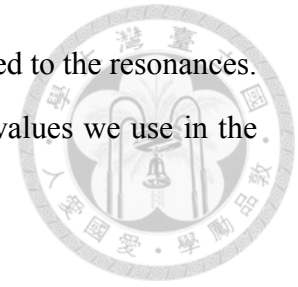
For an isolator, it is complicated to assign various materials in the full EM simulation, including the metal housing, high dielectric alumina, ferrites, silicon steels, low dielectric Teflon and glues. Furthermore, the electrical property of materials changes with different temperature and frequencies. The isolator is designed for 100GHz and 20K, and we also expect that it works at room temperature. EM simulation thus requires two results, 300K and 20K. We cannot have comprehensive information of low temperature and high frequency, but there is still a trend to make a correct guess. The materials that we have to consider are ferrite TT2-111, alumina, and Teflon. Here we discuss the alumina as an example.

While the frequency increases, the value for epsilon of a dielectric slightly decreases at radio band ($10^8 - 10^{11}$ Hz) and remains a constant at a higher and lower band ($10^{11} - 10^{12}$ and $10^4 - 10^8$ Hz). That is because of four polarization mechanisms in dielectrics: space charge, orientation, ionic, and electron polarization, where the orientation polarization are losing effectiveness at radio band [57]. The vendor's datasheet gives that ϵ of 99.6% alumina is 10.2 at 1MHz, and that of 96% alumina is 9.4 at 10MHz [2]. The HFSS database gives ϵ of 9.4 at 10GHz, and in Afasar's study [8], ϵ is from 9.6 (100GHz) to 9.594 (300GHz). In summary, ϵ increases as higher alumina purity, decreases from 10MHz to 10GHz, and stays in 9.4-9.6 in 10-300GHz. We thus adopt the ϵ of 9.4-9.6 at 100GHz.

With decreased temperature, the mobility of polar molecules will fall and thus lower the dielectric constant. For example, Molla's study [74] reported that ϵ of the sapphire, a kind of high-purity and crystalline alumina, is 9.41 (300K) and 9.26 (20K). Since the cryogenic cooling causes $\delta\epsilon$ of -0.15, a decline of 1.6%, we expect the ϵ of alumina is 9.25-9.45 at 20K.

The value of the loss tangent increases with both higher frequency and temperature. For $\tan\delta$ of 99.5% alumina, the vendor's datasheet gives 2×10^{-4} (10MHz) [2], the HFSS database gives 6×10^{-4} (10GHz). Afasar [8] measured that it is 6×10^{-4} (100GHz) and rises to 13×10^{-4} (300GHz). On the other hand, for the cryogenic test, Molla [74] measured that $\tan\delta$ of 99.9% alumina is 3×10^{-4} (300K) and falls to 10^{-5} order (100K). These

are two compromising effects, and the loss tangent is usually unrelated to the resonances. We apply the HFSS value, 6×10^{-4} . The table lists the electrical values we use in the simulations.





Chapter 4

Cryogenic

In this chapter, we discuss the cryogenics design, including the receiver cartridge, cryostat and vacuum system. We also provide the thermal load estimations of the multi-pixel receiver.

4.1 Introduction to Receiver Cryostat

A cryostat is a large vacuum chamber or Dewar that contains devices such as electrical components and vacuum instruments. Assembling these devices causes the cryostat's design very complicated. The standard method for the cryostat installation is applying a receiver cartridge, which mechanically supports and fixes the receiver components. We can easily install a receiver by putting cartridges into a cryostat. Moreover, the cartridge design is aiming to reduce the thermal load. The material applied to cartridge structures is usually G10, a high-pressure fiberglass laminate similar to carbon fiber but having lower thermal conductivity.

The 80-116GHz receiver cartridge consists of two cooling stages, in which the first stage is 70K is and the second stage is 20K. The cold head of the cryopump CTI-350 (CTI cryopump model 350) penetrated the cryostat gives the cooling power. LNAs are thermally anchored to 20K on the cold head, using heat traps made of oxygen-free high thermal conductivity copper (OFHC). The upper and the lower stainless waveguides clamp the radiation shield, fixed to 70K of the cold head. The stainless waveguide is thus anchored

at 70K and provides thermal insulation to 20K and 300K.

The cryopump CTI-350 is initially installed on a standard CTI pump, Flat on-board 8F, which includes a vacuum vessel and radiation shield. The vacuum vessel is a stainless steel chamber having an inner diameter of 200mm, an inner length of 227mm, and a thickness of 2.5mm. Since the outermost diameter of the 19-pixel LNA blocks is 102mm, much smaller than the vessel, we can directly use Flat on-board 8F as the receiver cryostat. On the vacuum vessel's bottom, we drill a hole and solder a vacuum flange, and hence the chamber can be extended by adding a receiver top and a receiver bottom. With a smaller diameter of 123mm, the receiver top can be put in the primary dish's hole, in which the hole diameter is 130mm. The receiver bottom design allows 38 waveguide vacuum feed-throughs installed. The final exterior cryostat will have a diameter of 205mm and a length of 460mm, where the cryostat size is similar to a 6 liter round bucket.

The 19-pixel receiver components have 38 waveguide filters fixed on the receiver bottom, giving a strong base. The stainless steel waveguides anchored on the 70K radiation shield also support the components. Therefore, we use the compact front-end chain as a cartridge instead of adding a G10 structure that may cause more thermal conduction. The position of feedhorns may have a tiny shift while the cryostat is tilted in observations, and hence we put a thin Teflon plate at the place of the feed horn's neck to increase the stability.

4.2 Heat Transfer

4.2.1 Introduction

The third critical issue we concern about is the thermal load given by multi-pixel receivers (another two issues are the off-axis problem and the cryogenic LNA design). For example, the cryopump CTI-22 (CTI cryopump model 22) applied in the one-pixel receiver has a cooling power of 6W (70K) and 1W (20K). The cryopump CTI-350 that we aim to employ in the 7-pixel receiver has 15W (70K) and 4W (20K). If we assume, in the worst case, the cooling power is linear dependent on the number of pixels, the 7-pixel

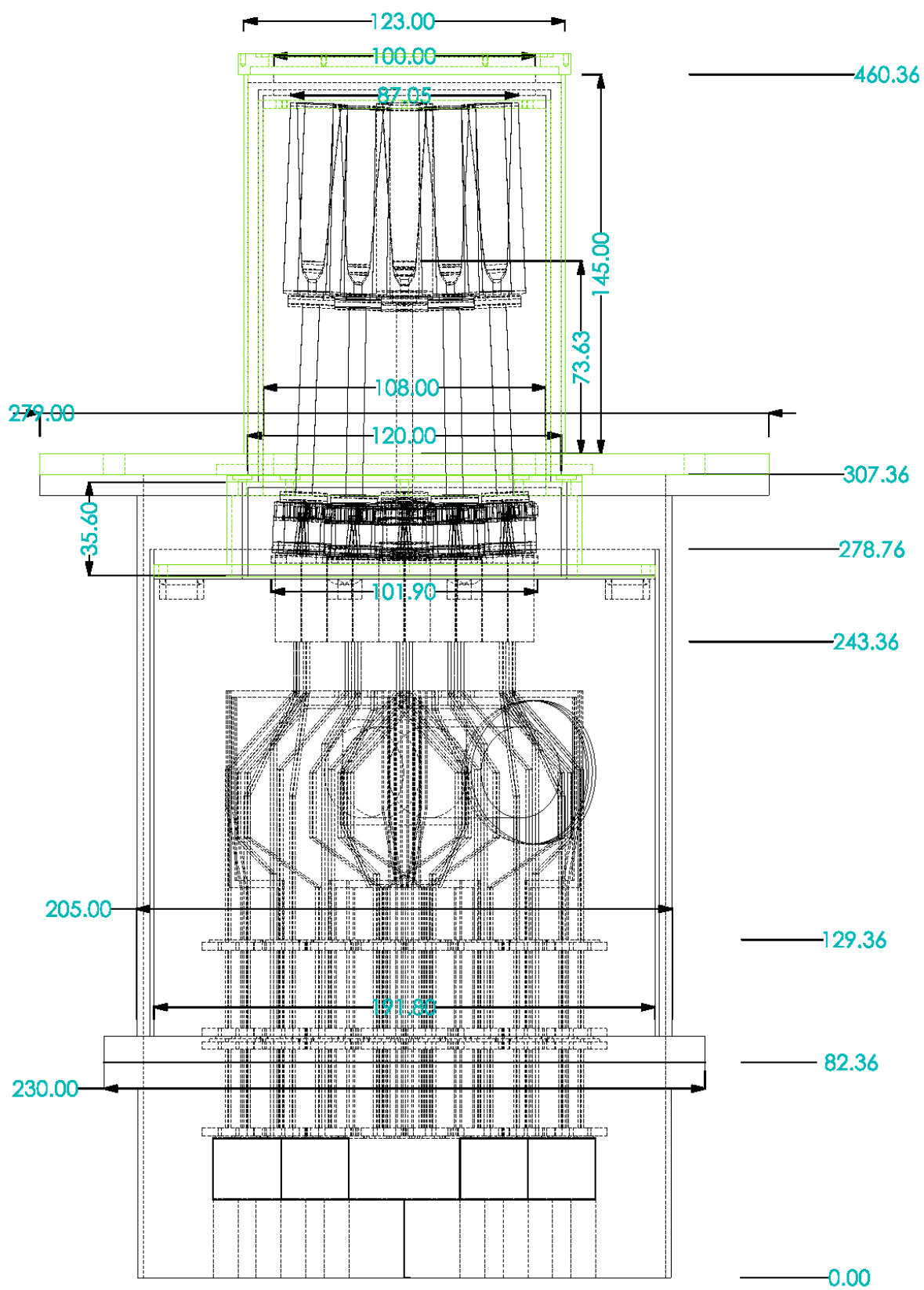


Figure 4.1: Schematic of the receiver cryostat.

receiver will require 42W (70K) and 7W (20K), much larger than the ability of the cryopump CTI-350. However, the real pixels are stacked compactly, and hence it is possible to achieve a lower value of the thermal load. In this section, we provide the estimation of the thermal load, and the result reveals that the cryopump CTI-350 can even sustain the 19-pixel receiver.

The ways of heat transfer include conduction, convection, and radiation. Since evacuating gas is the standard procedure for a cryostat to achieve the cryogenic temperature, we can exclude the heat convection in a high vacuum receiver. But we still have to consider the heat conduction through remaining low-pressure gas. Besides, Joule heating from the electrical resistance of wires and heat produced by active devices also contribute to the receiver's thermal load [114] [19]. Here all the diameter is in meter, and the unit of temperature is in Kelvin.

4.2.2 Thermal Conduction through Solids

The thermal conduction equation describes that given the temperature gradient (dT/dx), how the heat flow (dQ/dt) passed through a solid with a cross-section (A):

$$dQ/dt = -K(T)AdT/dx, \quad (4.1)$$

where $K(T)$ implies the thermal conductivity (m/K), a temperature-dependent coefficient that requires integration. For easily calculating, we assume that heat is flowing from T_1 to T_2 , through a solid bar with a uniform cross-section A and a length of L , the equation becomes

$$dQ/dt = -(A/L) \int K(T)dT = -(A/L)(\Theta_2 - \Theta_1), \quad (4.2)$$

where Θ is the integral of $K(T)$, defined as $\Theta = \text{integral } K(T) (\text{W/m})$. The equation is more useful for estimating the thermal load if we know the value of Θ . The figure1 and figure2 give $K(T)$ and Θ of selected materials. The table lists information of materials applied to receivers [3].

4.2.3 Thermal Radiation

The thermal radiation transfers heat by the electromagnetic waves generated from a black body with a temperature T , given the Stefan–Boltzmann law:

$$dQ/dt = \sigma AT^4, \quad (4.3)$$

where σ is the Stefan–Boltzmann constant ($\sigma = 5.67 \times 10^{-8} W m^{-2} deg^{-4}$) and A is the surface area. The equation indicates that the heat flow (or the radiated power) emitted by a black body is proportional to the fourth power of the black body temperature maintained in the thermal equilibrium. The black body is defined as a perfect body that absorbs radiations in all frequencies and emits the black body radiation with emissivity (ϵ) of 1. If given two black bodies with different temperature, T_1 and T_2 , the net energy exchange is $\dot{Q} = \sigma A(T_1^4 - T_2^4)$, in which \dot{Q} means dQ/dT . A real body has emissivity less than 1 ($0 < \epsilon < 1$), and hence the equation becomes

$$\dot{Q} = \epsilon \sigma AT^4, \quad (4.4)$$

For calculating the receiver's thermal load, the useful equation is the two parallel surface case, where two surfaces have different areas (A_1, A_2), different emissivity (ϵ_1, ϵ_2) and different temperature (T_1, T_2), given the heat flow:

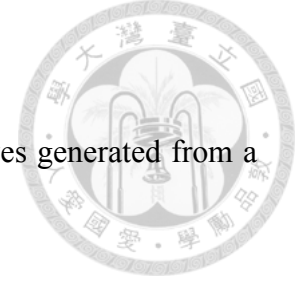
$$\dot{Q} = \sigma(T_1^4 - T_2^4) / \left(\frac{1 - \epsilon_1}{\epsilon_1 A_1} + \frac{1}{F_{12} A_1} + \frac{1 - \epsilon_2}{\epsilon_2 A_2} \right) \quad (4.5)$$

With $T_1 > T_2$, F_{12} implies a fraction that A_2 intercepts the radiation from A_1 , and we assume $F_{12} = 1$. If $A_1 = A_2 = A$, the equation reduces to [114]

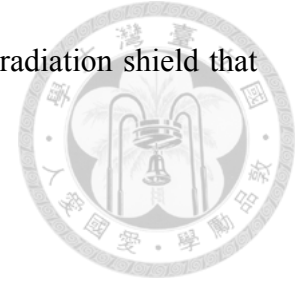
$$\dot{Q} = \sigma A(T_1^4 - T_2^4) \frac{\epsilon_1 \epsilon_2}{\epsilon_1 + \epsilon_2 - \epsilon_1 \epsilon_2} \quad (4.6)$$

If $\epsilon_2 \ll \epsilon_1$, the equation reduces to:

$$\dot{Q} = \sigma A(T_1^4 - T_2^4) \epsilon_2 \quad (4.7)$$



Using these equations, we can estimate the thermal load of the radiation shield that suffers the radiation from cryostat walls.



4.2.4 Heat Transfer in other ways

The other thermal load includes the heat conduction through a gas, joule heating, and heat produced by active devices. Estimating gas conduction involves various gas properties, such as thermal conductivity of gases, mean free path, molecular weight, and specific heat. In low pressure, the mean free path of gases is comparable to the receiver dimensions. The gas thermal conductivity is proportional to the remaining number of molecular and pressure. We can thus simplify the gas conduction equation. For two concentric cylindrical or spherical surfaces with a temperature difference ΔT , the gas heat conduction is [28]

$$\dot{Q} = K a_0 p A \Delta T, \quad (4.8)$$

where K is a constant with an approximate value of 2.1, 4.4, and 1.2 for helium, hydrogen, and air. The value of p is the gas pressure (Pa), A is the inner surface area (m^2), and a_0 is the accommodation coefficient. The accommodation coefficient characterizes the behavior of gas particles while they are colliding between two surfaces. Assuming two surfaces having the same area, the accommodation coefficient is

$$a_0 = \frac{a_1 a_2}{a_1 + a_2 - a_1 a_2}, \quad (4.9)$$

where a_1 and a_2 are the accommodation coefficient of two surfaces. The experimental value gives $a \leq 0.5$ for helium gas at low pressure while colliding in a metal cryostat. Taking the upper limit value of 0.5 for both surfaces, we use $a_0 = 1/3$ for calculating the receiver load.

Joule heating is resulting from ohm's law. While the electric current is flowing through wires, the electric resistance (ρ) gives the heat transfer of $\dot{Q} = I^2 R$. Since the electric resistance varies with temperature, the electric wire connected to two cooling stages has a

temperature gradient. We adopt a higher ρ , such as ρ (300K) for the 300-70K Joule heating. The table lists the electric resistivity of copper and constantan in different temperatures. Note that pure metal and alloys have distinct characteristics in thermal conductivity and electric conductivity. For copper, both conductivities increase by a factor of 100 from 300K to 20K. Below 20K, the copper's electric conductivity stills rise, but the thermal conductivity declines and gives roughly the same value at 4K and 300K. For constantan, the thermal conductivity declines by a factor of 5 from 300K to 20K (or a factor of 100 from 300K to 4K), but the electric conductivity remains roughly the same.

The active devices such as LNAs also produce heat, which can be estimated from the LNA power consumption given by bias circuits. While the receiver is cooling, the bias current will reduce due to the increasing electric mobility and conductivity. We thus expect a lower value of the LNA dissipated power. For example, an InP HEMP working in 4-12 GHz reported 50mA (1.8V) at 300K and 20mA (1.2V) at 15K.

4.3 Thermal Load

4.3.1 Thermal load of the First Stage

The thermal load of the first stage (300K-70K) includes:

- (1) Radiation from chamber walls to the radiation shield
- (2) Radiation from the window to IR filters
- (3) Radiation from IR filters to feed horns
- (4) Conduction through stainless waveguides
- (5) Conduction through LNA electric wires
- (6) Conduction through the gas
- (7) Joule Heating from LNA electric wires

Here we calculate the thermal load of a 19-pixel receiver and assume all nineteen LNAs are installed.

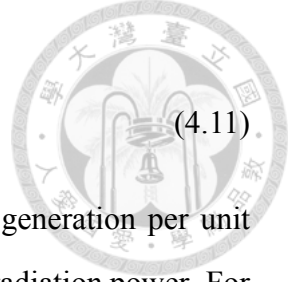
(1) The radiation shield's exterior is coated with polished nickel, given $\epsilon = 0.033$ at 70K [82], and the exterior surface is $231,410\text{mm}^2$. The chamber consists of a stainless steel part and two extended aluminum parts, and the stainless (aluminum) inner surface is $172,788\text{mm}^2$ ($167,453\text{mm}^2$). In total, the cryostat's inner area is $340,241\text{mm}^2$. The aluminum surface at 300K has $\epsilon = 0.1$, and a stainless steel surface at 300K has $\epsilon = 0.074$. Here we assume a normal metal surface using machine milling. Since aluminum suffers more oxidization than stainless steel, aluminum has a higher epsilon. The emissivity of a highly-oxidized Al surface is 0.31. Using the equation and assuming all the cryostat surfaces are aluminum, the thermal load is:

$$\begin{aligned} \dot{Q} &= \sigma(300^4 - 70^4) / \left(\frac{1 - 0.1}{0.1 \times 340241 \times 10^{-6}} + \frac{1}{340241 \times 10^{-6}} + \frac{1 - 0.033}{0.033 \times 231410 \times 10^{-6}} \right) \\ &= 2.935(W) \end{aligned} \tag{4.10}$$

If all the cryostat surfaces are stainless steel, the thermal load is 2.753W.

(2) The Zotefoam window can transmit millimeter-wave and forbid part of IR radiations, given $\epsilon = 0.68$ at 300K [50]. The IR filter, put on the 70K radiation shield, employs metal meshes plating on one side of a quartz layer to reflect and absorb IR radiations. Thus, we assume that the IR filter is a reflective surface similar to highly oxidized aluminum ($\epsilon = 0.31$). The diameter of windows and IR filters is 119mm and 101.6mm . Using the equation, the thermal load from the window to the IR filter is 1.125W.

(3) To locate feedhorns, we put a Teflon plate between the middle part of horns and the radiation shield, and hence the feedhorns are at 70K. The edge of IR filters is also at 70K. However, since the IR filter suffers thermal radiation from the window, it's limited thermal conductivity will cause thermal gradient and re-emit radiation. With a diameter of R , a thickness of t , an edge temperature of $T(R)$, the temperature at radius r of IR filters gives [56]



$$T(r) = T(R) + \frac{q_g(R^2 - r^2)}{4K}, \quad (4.11)$$

where K is the thermal conductivity and q_g is the rate of heat generation per unit volume. In the IR filter's case, $q_g = P/2\pi Rt$, P implies the incident radiation power. For the thickness of $3mm$, the temperature at the center ($r = 0$) is:

$$T(0) = T(R) + \frac{PR}{8\pi t} = 70 + \frac{1.125W \times (50.8 \times 10^{-3})}{8\pi(3 \times 10^{-3})} = 2.9K \quad (4.12)$$

We assume the reheated IR filter is 80K and apply quartz emissivity of 0.93 (300K) to the value of 80K. With the gold-plated surface, the feed horns area faced to filters is $51,558mm^2$, given $\epsilon = 0.026$ (20K). Using the equation, the thermal load from IR filters to feed horns is $1.167 \times 10^{-3} W$.

(4) The stainless waveguide is compressed from a stainless steel tube with an inner radius of $1.9mm$, an outer radius of $2.1mm$, and a thickness of $0.2mm$, given a cross-section of $0.62832mm^2$. The total length of a waveguide is $38mm$. If we exclude the length of two flanges, the stainless section is $29mm$, in which stainless steel has $\Theta = 3000W/m$ (300K) and $\Theta = 300W/m$ (70K). A waveguide's thermal load is

$$\dot{Q} = \frac{0.62832 \times 10^{-6}}{29 \times 10^{-3}}(3000 - 300) = 0.0585W \quad (4.13)$$

A 19-pixel receiver has 38 stainless waveguides for thermally insulating the first stage, and the total load is 2.223W (for 38 guides).

(5) Lakeshore DT-32 is an enameled wire applied for cryogenics, in which phosphor bronze is surrounded by polyimide. The insulator diameter is $0.241mm$, and the conductor diameter is $0.203mm$. Polyimide gives the conductivity of $0.1W/mK$ at 70K (), similar to Teflon, and hence we use the integrated $K(T)$ of Teflon for calculating polyimide. The middle section of LNA bias wires, anchored at 70K, requires a wire length of $275mm$ to connect 300K and 70K. A 19-pixel receiver has 249 wires in total, including two wires for the temperature sensor placed at 70K and 247 biases for 19 LNAs (each LNA gives 13 bias wires). The conductor part of a wire contributes:



$$\dot{Q}(\text{conductor}) = \frac{\pi(0.203/2)^2 \times 10^{-6}}{175 \times 10^{-3}}(10000 - 1000) = 1.05923 \times 10^{-3}W \quad (4.14)$$

The insulator part contributes:

$$\dot{Q}(\text{insulator}) = \frac{\pi[(0.241/2)^2 - (0.203/2)^2] \times 10^{-6}}{175 \times 10^{-3}}(70 - 10) = 2.89118 \times 10^{-6}W \quad (4.15)$$

The total thermal load of a wire is $\dot{Q}(\text{conductor}) + \dot{Q}(\text{insulator}) = 1.062125 \times 10^{-3}W$ (per wire), and 249 wires provide $2.623 \times 10^{-1}W$.

(6) Referred to the equation, we assume the constant k of 2.1 (helium gas), a_0 of 1/3, the pressure of 1.33×10^{-4} Pa (10^{-6} torr), the heat conducted by gas is:

$$\dot{Q} = 2.1 \times 1/3 \times (1.33 \times 10^{-4}) \times (231410 \times 10^{-6})(300 - 70) = 4.955 \times 10^{-3}W \quad (4.16)$$

(7) The phosphor bronze wire (0.203mm in diameter) of DT-32 has a resistance of 4.02 ohm/m (305K) and 3.45 ohm/m (77K). We use the mean resistance of 3.735 ohm/m and apply the LNA bias current measured at room temperature for the upper limit. An LNA contains four Vd wires with 16mA and two Vd wires with 32mA, given thermal loads:

$$\dot{Q} = [4 \times (16 \times 10^{-3})^2 + 2 \times (32 \times 10^{-3})^2] \times 3.735 \times (275 \times 10^{-3}) = 3.155 \times 10^{-3}W \quad (4.17)$$

The total thermal load from the Joule heating gives $5.995 \times 10^{-2} W$ (19 LNAs).

In summary, the 300K-70K stage contributes 7.49W, 49.99% of the cooling power, where the first three dominate terms are:

- Radiation from walls to shields (25.48%)
- Conduction by stainless waveguides (14.82%)

- Radiation from windows to IF filters (7.50%)



4.3.2 Thermal load of the Second Stage

The thermal load of the second stage (70K-20K) includes:

- (1) Radiation from the radiation shield to front-end elements
- (2) Conduction through circular waveguides
- (3) Conduction through stainless waveguides
- (4) Conduction through LNA electric wires
- (5) Conduction through the gas
- (6) Joule Heating from LNA electric wires
- (7) Heat produced by LNAs

(1) The radiation shield's interior is coated with the black nickel, a Zn-Ni alloy usually applied to decoration and metal protection. The emissivity of black nickel is 0.83 at room temperature [103], and we adopt it for the value of epsilon at 70K. Given the thickness of $2mm$, the shield interior surface is roughly the same as the exterior. Front-end elements are coated with gold, which gives $\epsilon = 0.026$ at 78K, and we adopt the value for 20K. The surface area of front-end elements calculated by HFSS is $394,513mm^2$. Using the equation, the heat radiated from shields to front-end elements gives 1.35×10^{-2} W.

(2) The circular waveguides put after feed horns is a thin-wall stainless waveguide plated with gold in its interior side. The stainless part has an inner diameter of $3mm$, a thickness of $0.2mm$, and a length of $80mm$, given an inner perimeter of $9.425mm$ and a cross-section of $2.011mm$. With a buffer nickel layer of $1\mu m$, the $1\mu m$ gold provides the electric conductivity. The cross-section of the nickel layer and gold layer is $9.425 \times 10^{-3}mm^2$. Using the table, the heat conduction for a waveguide is:



$$\dot{Q} = \frac{1}{80 \times 10^{-3}} [2.011 \times 10^{-6}(300 - 18) + 9.425 \times 10^{-9}(40000 - 20000) + 9.425 \times 10^{-9}(3270 - 320)] = 9.791 \times 10^{-3} \text{ W} \quad (4.18)$$

A 19-pixel receiver requires 19 waveguides, and hence the total thermal load is 0.186W (19 waveguides).

(3) The stainless waveguide is identical to that applied in the first stage. Using the same calculation with $\Theta = 300 \text{ W/m}$ (70K) and $\Theta = 18 \text{ W/m}$ (20K), a waveguide gives $6.81 \times 10^{-3} \text{ W}$. The total thermal load is 0.259 W (for 38 guides).

(4) The section of LNA bias wires from 70K to 20K requires a length of 200mm. The wire heat conduction is the same as the first stage but using the integrated $K(T)$ of 70K and 20K. A wire gives $\dot{Q}(\text{conductor}) + \dot{Q}(\text{insulator}) = 1.456 \times 10^{-4} \text{ W} + 5.963 \times 10^{-7} \text{ W} = 1.462 \times 10^{-4} \text{ W}$ (per wire), and 249 wires provide $3.612 \times 10^{-2} \text{ W}$.

(5) Using the equation and the inner area of 394, 513mm² (the surface of front-end elements), the heat conducted by gas is $1.839 \times 10^{-3} \text{ W}$.

(6) We use 3.45 ohm/m (77K) of DT-32 phosphor bronze wire to calculate the Joule heating of the second stage. An LNA gives the thermal load of $2.119 \times 10^{-3} \text{ W}$ (per LNA), and the total is $4.027 \times 10^{-2} \text{ W}$ (19 LNAs).

(7) From two-chip LNA measurement, an LNA working at room temperature requires the drain biases of $I_d = 30 \text{ mA}$ ($V_d = 1.5 \text{ V}$) and $I_d = 32 \text{ mA}$ ($V_d = 1.1 \text{ V}$) for one polarization. An LNA contains two polarizations and gives the dissipated power of 80.2mW (per LNA). The total dissipated power is 3.047 W (19 LNAs).

Though the LNA dissipated power accounts for most of the thermal load, it will decrease at cryogenic temperature. If it reduces to half power, 40.1mW, the total dissipated power is 1.523W.

In summary, the 70K-20K stage contributes 3.585W, 89.63% of the cooling power. But if the LNA dissipated power is a half, the load is 51.54% of the cooling power. The first three dominate terms are:

- LNA dissipated power (76.19%)



- Conduction by stainless waveguides (6.47%)
- Conduction by circular waveguides (4.65%)

4.3.3 Discussion of the Thermal Load

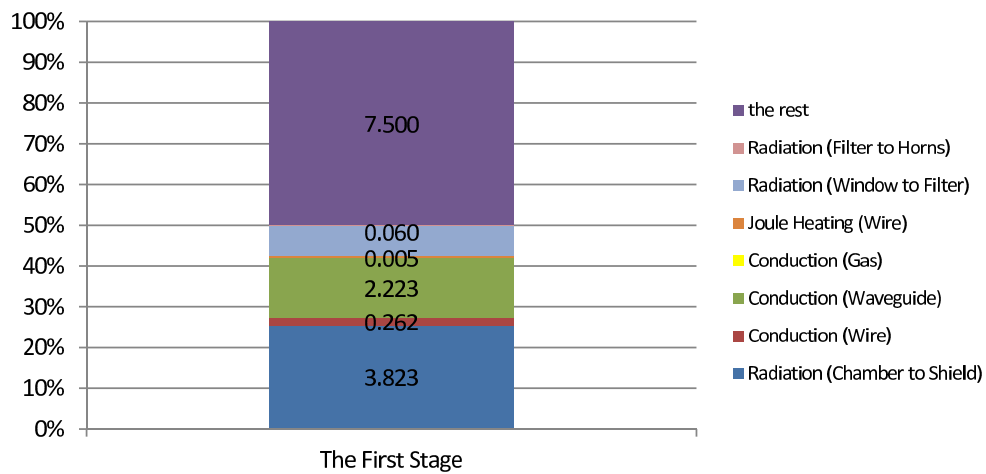


Figure 4.2: The thermal load of the first stage.

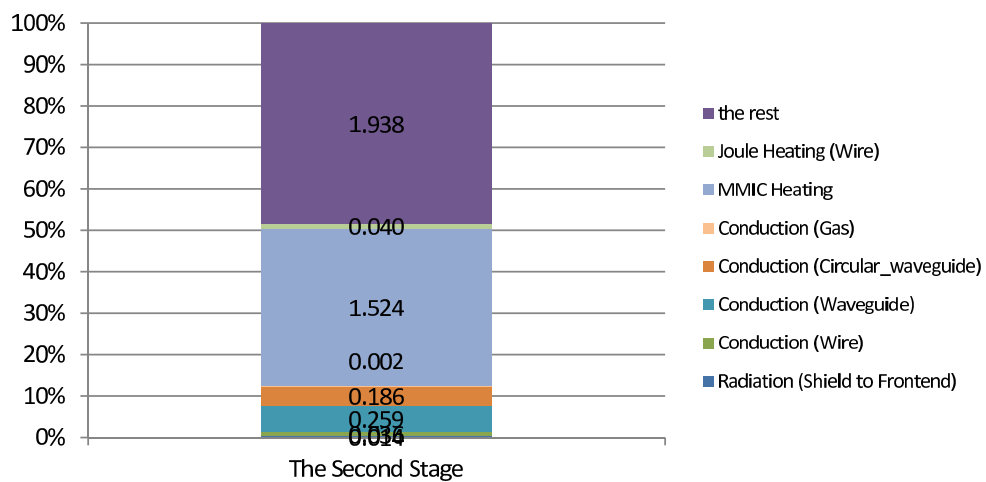


Figure 4.3: The thermal load of the second stage.





Chapter 5

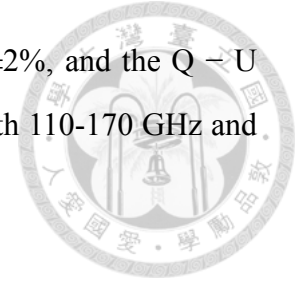
Conclusion

This work presents a 19-pixel front-end receiver with wide-band (80-116GHz), wide field of view, and dual-polarization for the NTU-array. Currently, only 7-pixel contains low noise amplifiers (LNA), and hence the receiver gives 7-pixel images. The NTU interferometer array equipped with the 7-pixel receiver can reduce its survey time by a factor of 7.

Though the multi-pixel receiver directly enhances the mapping speed of telescopes or arrays, it has three concerns: off-axis feeds, LNA modules with dual-polarization, and thermal loads. First, applied the information of a 1.2-meter diameter dish, we give the optical simulation of off-axis feed horns. Results show that with a displacement of 1.5 mm, we can reduce the phase deviation of outer horns to only 1.4% of a wavelength, less than the surface roughness of dishes. Hence, the 19-pixel feed is safe for the receiver optics.

Second, we design a septum polarizer and the cryogenic LNA module. In tradition, the septum polarizer is limited to a significantly narrower bandwidth than the ortho-mode transducers (OMT). However, the septum polarizer possesses advantageous features unparalleled by the OMT when determining astronomical polarization. Moreover, the septum polarizer design is simple, compact, and suitable for multi-pixel receivers. We design an extremely wide-band circular waveguide septum polarizer, covering 42% bandwidth, from 77 GHz to 118 GHz, without any undesired resonance, challenging the conventional bandwidth limit. Stokes parameters, constructed from the measured data between 77 GHz

and 115 GHz, show that the leakage from I to Q and U is below $\pm 2\%$, and the Q \rightarrow U mutual leakage is below $\pm 1\%$. We also design septum polarizers with 110-170 GHz and 144-220 GHz, which give a comparable performance.





Appendix A

Polarization Leakage

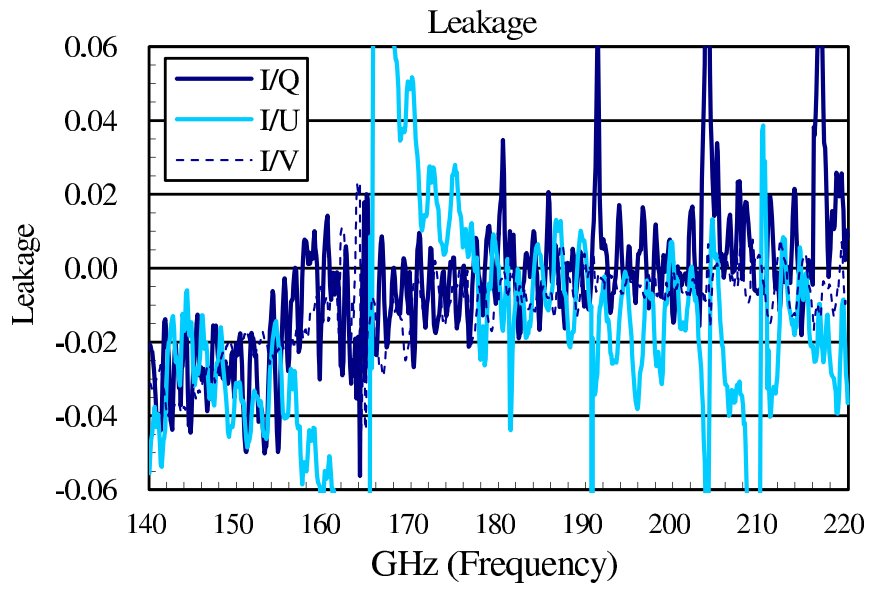


Figure A.1: Leakage of 140-220GHz polarizer.

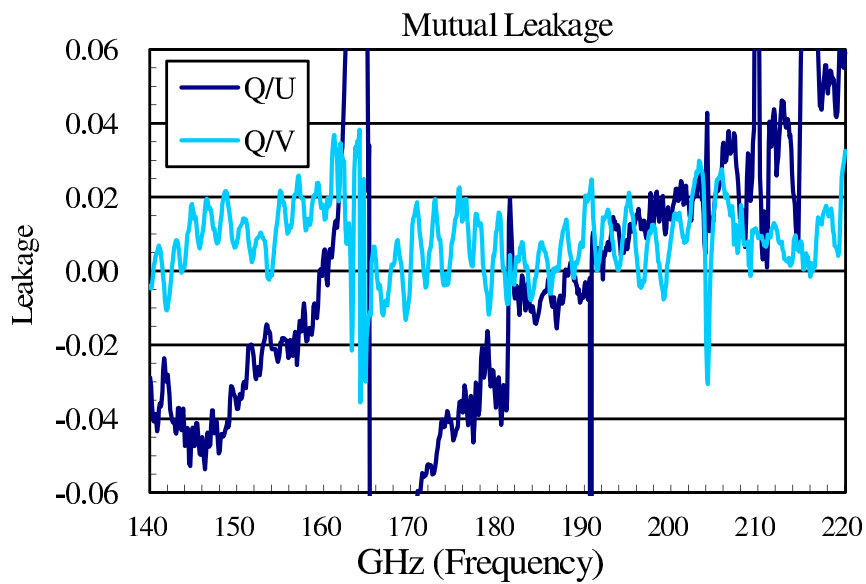


Figure A.2: Mutual leakage of 140-220GHz polarizer.

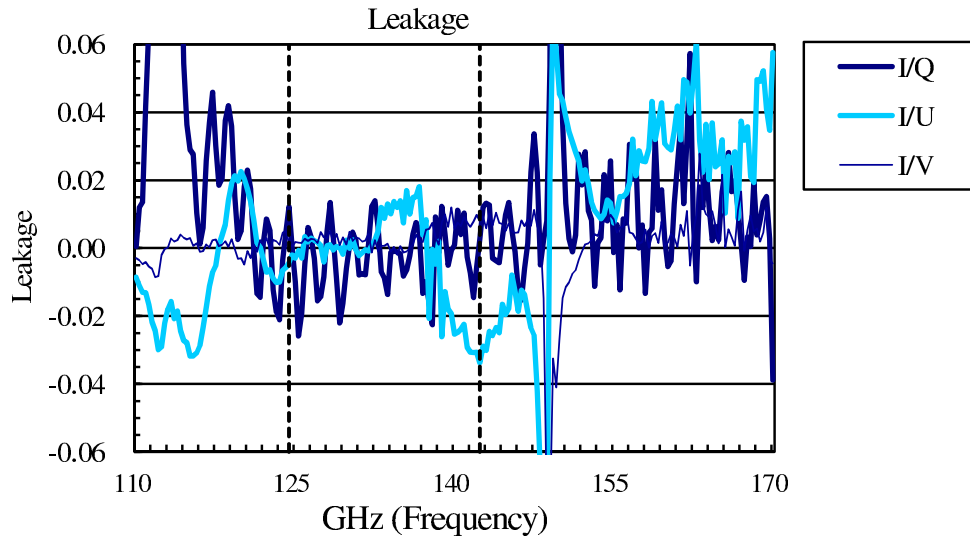


Figure A.3: Leakage of 110-170GHz polarizer.

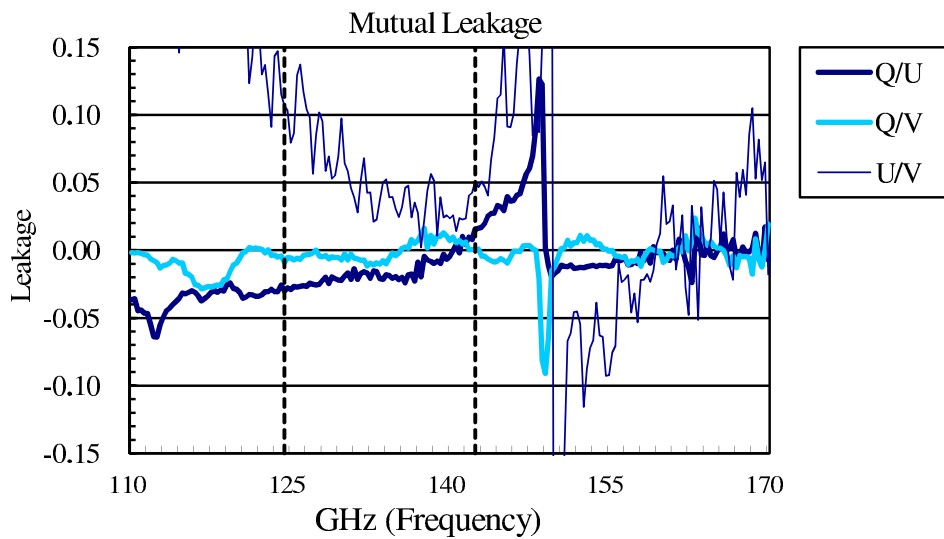


Figure A.4: Mutual leakage of 110-170GHz polarizer.

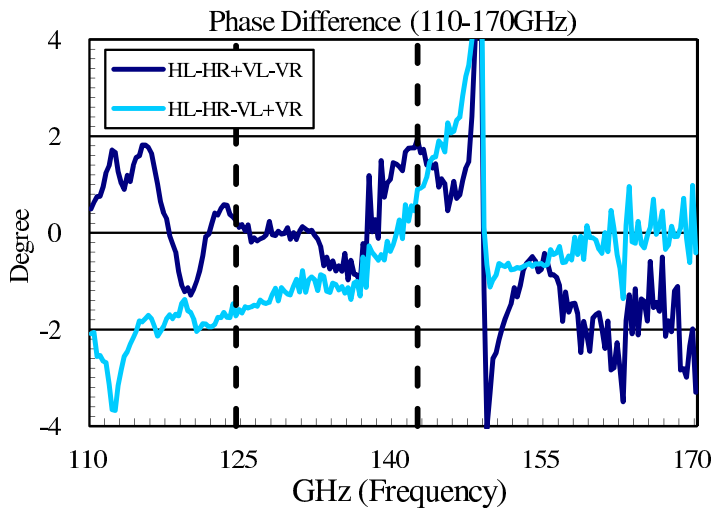


Figure A.5: Phase of 110GHz polarizer.

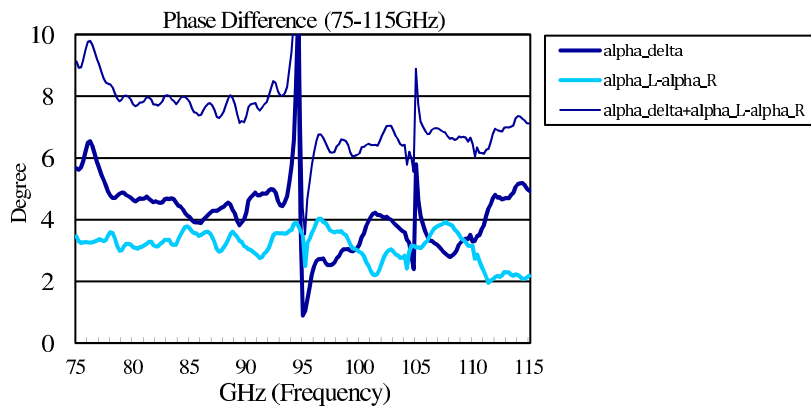


Figure A.6: Phase of 75GHz polarizer.

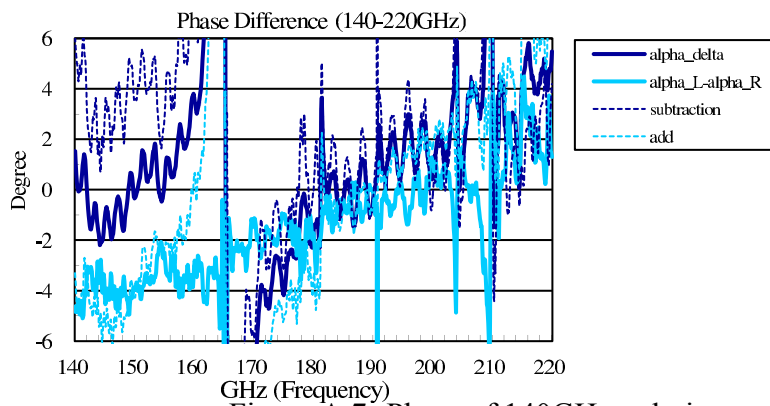


Figure A.7: Phase of 140GHz polarizer.



Appendix B

Adhesives operation

While we attach housing components, silver epoxy provides a grounding for the electronics, and therefore a uniform epoxy layer, not too thin, requires spreading broadly and connected. In the figure we depict adhesives coating steps. First, the datasheet suggested a A/B weight ratio of 1/1 and volume ratio of 3/2, but we just need a few adhesives, which amount is about a small grain for limited number of housings. Therefore, we take approximately the same portion of A/B epoxies by hand, with two different plastic toothpicks, and then mix them by another toothpick. Blending epoxies fast and frequently could produce tiny bubbles, and hence we mix clockwise and anti-clockwise, for 3-5 times.

Second, we put epoxies on the alcohol cleaned metal surface, using a sewing needle. The sharpened tip of a sewing needle is about 0.2mm and suitable for the 0.51mm probe channel width. It is critical to control the adhesives in a small area and components in an accurate position. The epoxy layer requires a particular thickness, where a thin layer will deteriorate electrical and thermal contact. On the contrary, a thick layer results in overflowing to the topside because the probes and chips are only 0.1mm thickness. With proper stress by hand, we measure that the cured epoxy has the thickness of 20-40um, which is the same as an adhesive film of an ordinary tape. We place tiny epoxy drops in a distance, connect them, spread them to the chip area, and leave a space near the edges.

Third, put and locate a small component on epoxies. For commercial, people use the vacuum pick-up system. In our case, the probes and capacitors are tiny (for example, $0.375 \times 0.5\text{mm}$ of 10pF), and hence we use a simple way: a toothpick attached a little

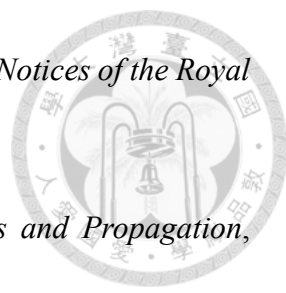
blue tack. The blue tack is a solid adhesive widely applied in home decoration, and the advantages include soft, flexible, and easily removable without any traces. We adjust a component and press it by another toothpick which has a flattened tip. For a die having relatively wide dimension, we press it by a larger plastic toothpick with a buffered PET film.


Finally, heating H20E epoxies at cure temperature. The datasheet reported that the curing exotherm peak is approximately 150 degrees, indicating the cross-linking occurs, and epoxies are fast curing in ten minutes. At the low temperature, such as 80 degrees, there is also a small amount of exotherm starting, but it will take around four hours to cure. From our B2B probe test, if measuring the probe with uncured epoxies at room temperature, we get worse S21 of -2.5dB, but the S21 is getting better very slowly in each integration time. That reveals the uncured epoxy is already conductive, and the curing raises its conductivity. Typically, the silver epoxy cures at a higher temperature will have more electric conductivity. For our housing, we apply the curing temperature of 120 degrees and 15min heating time.

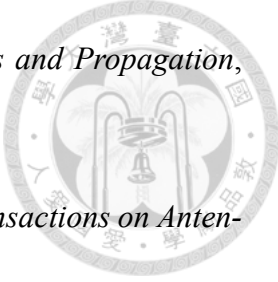


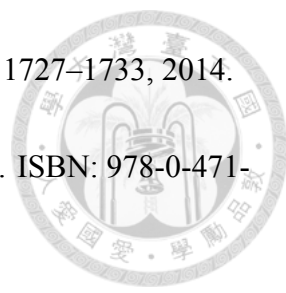
Bibliography


- [1] <https://www.microwaves101.com/encyclopedias/wirebonding>.
- [2] <https://www.phononmeiwa.co.jp/en/products/item/07.html>.
- [3] Appendix I: Cryogenic Reference Tables. <https://www.lakeshore.com/>.
- [4] Technique Documents: Noise Figure Measurement Methods and Formulas, Maxim Integrated Tutorials 2875. <https://www.maximintegrated.com/en/design/technical-documents/tutorials/2/2875.html>.
- [5] Abazajian, K. M., Abitbol, M. H., Ahmed, Z., et al. *arXiv:1706.02464*, 2017.
- [6] Ade, P. A. R., Aikin, R. W., Barkats, D., et al. *Phys. Rev. Lett.*, 112(24):1–25, 2014.
- [7] Ade, P. A. R., Pisano, G., Tucker, C., and Weaverr, S. *Proc. SPIE, Millimeter and Submillimeter Detectors and Instrumentation for Astronomy III*, 6275:248–262, 2006.
- [8] Afsar, M. N. *IEEE Transactions on Microwave Theory and Techniques*, 32(12):1598–1609, 1984.
- [9] Albertsen, N. C. and Skov-Madsen, P. *IEEE Transactions on Microwave Theory and Techniques*, 31(8):654–660, 1983.
- [10] Barkats, D., Dierickx, M. I., Kovac, J. M., et al. *Proc. SPIE, Millimeter, Submillimeter, and Far-Infrared Detectors and Instrumentation for Astronomy IX*, 10708:355–368, 2018.

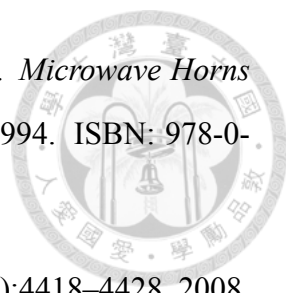
- 
- [11] Bayet, E., Gerin, M., Phillips, T. G., and Contursi, A. *Monthly Notices of the Royal Astronomical Society*, 399(1):264–272, 2009.
- [12] Behe, R. and Brachet, M. *IEEE Transactions on Antennas and Propagation*, 39(8):1222–1224, 1991.
- [13] Birkinshaw, M. *Physics Reports*, 310(2):97–195, 1999.
- [14] Bornemann, J. and Labay, V. A. *IEEE Transactions on Microwave Theory and Techniques*, 43(8):1782–1787, 1995.
- [15] Bornmann, J., Amari, S., Uher, J., and Vahldieck, R. *IEEE Transactions on Microwave Theory and Techniques*, 47(3):330–335, 1999.
- [16] Britton, J. W., Nibarger, J. P., Yoon, K. W., et al. *Proc. SPIE, Millimeter, Submillimeter, and Far-Infrared Detectors and Instrumentation for Astronomy V*, 7741:229–239, 2010.
- [17] Bryerton, E., Mei, X. B., Kim, Y., et al. *IEEE MTT-S International Microwave Symposium Digest*, pages 681–684, 2009.
- [18] Chen, M. H. and Tsandoulas, G. N. *IEEE Transactions on Antennas and Propagation*, 21(3):389–391, 1973.
- [19] Chen, M. T. *AMiBA Receiver Lab Report*, 2003.
- [20] Chen, Y. L., Chiueh, T. H., and Teng, H. F. *The Astrophysical Journal Supplement Series*, 211(1):11, 2014.
- [21] Ciccognani, W., Giannini, F., Limiti, E., and Longhi, P. E. *European Microwave Integrated Circuit Conference*, pages 314–317, 2008.
- [22] Condon, J. J. and Ransom, S. M. *Essential Radio Astronomy*. Princeton University Press, 2016. ISBN: 978-0-691-13779-7.
- [23] Cremonini, A., Mariotti, S., and Roda, J. *Cryogenics*, 52(10):445–451, 2012.

- 
- [24] Davis, D., Digiondomenico, O. J., and Kempic, J. A. *IEEE Antennas and Propagation Society International Symposium*, pages 26–33, 1967.
- [25] Doo, J., Park, W., Choe, W., and Jeong, J. *Electronics*, 8(523):1–9, 2019.
- [26] Ediss, G. A., Horner, N., Johnson, F., et al. *ALMA Memo*, (536), 2005.
- [27] Ege, T. and McAndrew, P. *Electronics Letters*, 21(24):1166–1168, 1985.
- [28] Ekin, J. W. *Experimental Techniques for Low-Temperature Measurements*. Oxford University Press, 2006. ISBN: 978-0-19-857054-7.
- [29] Emerson, D. *ASP Conference Series: Single-Dish Radio Astronomy: Techniques and Applications*, 278:27–43, 2002.
- [30] Erickson, N. R. *IEEE MTT-S International Microwave Symposium Digest*, 2:1175–1178, 2001.
- [31] Erickson, N. R. and Grosslein, R. M. *IEEE Transactions on Microwave Theory and Techniques*, 55(12):2495–2501, 2007.
- [32] Erickson, N. R., Grosslein, R. M., Erickson, R. B., and Weinreb, S. *IEEE Transactions on Microwave Theory and Techniques*, 47(12):2212–2219, 1999.
- [33] Esteban, J. and Rebollar, J. M. *IEEE Antennas and Propagation Society International Symposium*, 4:2146–2149, 1992.
- [34] Franco, M. J. *IEEE Antennas and Propagation Magazine*, 53(3):142–146, 2011.
- [35] Galuscak, R., Hazdra, P., and Mazanek, M. *International Journal of Antennas and Propagation*, 2012.
- [36] Giovanelli, R., Haynes, M. P., Kent, B. R., et al. *The Astrophysical Journal*, 130(6):2598–2612, 2005.
- [37] Granet, C. *IEEE Antennas and Propagation Magazine*, 40(2):76–82, 1998.
- [38] Granet, C. *IEEE Antennas and Propagation Magazine*, 40(3):82–89, 1998.

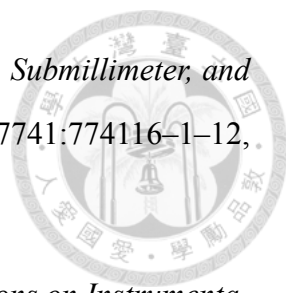
- 
- [39] Granet, C. and James, G. L. *IEEE Transactions on Antennas and Propagation*, 47(2):76–84, 2005.
- [40] Granet, C., James, G. L., Bolton, R., and Moorey, G. *IEEE Transactions on Antennas and Propagation*, 52(3):848–854, 2004.
- [41] Green, J. A., Caswell, J. L., Fuller, G. A., et al. *Monthly Notices of the Royal Astronomical Society*, 392(2):783–794, 2008.
- [42] Gupta, K. C., Garg, R., and Chadha, R. *Computer-aided design of microwave circuits*. Artech House, 1981. ISBN: 978-0-890-06106-0.
- [43] Haiman, Z., Mohr, J. J., and Holder, G. P. *The Astrophysical Journal*, 553(2):545–56, 2001.
- [44] Hogan, C. L. *Rev. Mod. Phys.*, 25(1):253–262, 1953.
- [45] Holland, W. S., Bintley, D., Chapin, E. L., et al. *Monthly Notices of the Royal Astronomical Society*, 430(4):2513–2533, 2013.
- [46] Hu, W., Hedman, M. M., and Zaldarriaga, M. *Phys. Rev. D*, 67:043004–1, 2003.
- [47] Hu, W. and White, M. *New Astronomy*, 2(4):323–344, 1997.
- [48] Hui, H., Ade, P. A. R., Ahmed, Z., et al. *Proc. SPIE, Millimeter, Submillimeter, and Far-Infrared Detectors and Instrumentation for Astronomy IX*, 10708:1–15, 2018.
- [49] Ihmels, R., Papziner, U., and Arndt, F. *IEEE MTT-S International Microwave Symposium Digest*, 2:909–912, 1993.
- [50] Inoue, Y. *The thermal design of the POLARBEAR-2 experiment*. PhD thesis, Graduate University for Advanced Studies, 2013.
- [51] Inoue, Y., Ade, P. A. R., Akiba, Y., et al. *Proc. SPIE, Millimeter, Submillimeter, and Far-Infrared Detectors and Instrumentation for Astronomy VIII*, 9914:372–380, 2016.

- 
- [52] Inoue, Y., Matsumura, T., Hazumi, M., et al. *Appl. Opt.*, 53(9):1727–1733, 2014.
- [53] Jackson, J. D. *Classical Electrodynamics, 3rd ed.* Wiley, 1998. ISBN: 978-0-471-30932-1.
- [54] Jakob, G. and Lizona, J. *SPIE Proceedings, Modern Technologies in Space- and Ground-based Telescopes and Instrumentation*, 7739:1–17, 2010.
- [55] Jennings, M., Kurras, M., and Plettmeier, D. *IEEE International Workshop on Antenna Technology*, pages 1–4, 2010.
- [56] Karwa, R. *Heat and Mass Transfer*. Springer, 2017. ISBN: 978-981-10-1556-4.
- [57] Kingery, W. D., Bowen, H. K., and Uhlmann R. *Introduction to Ceramics, 2nd Edition*. Wiley, 1976. ISBN: 978-0-471-47860-7.
- [58] Kocharyan, K. N., Afsar, M., and Tkachov, I. I. *IEEE Transactions on Microwave Theory and Techniques*, 47(12):2636–264, 1999.
- [59] Koller, D., Kerr, A. R., and Ediss, G. A. *ALMA Memo*, (397), 2001.
- [60] Koller, D., Kerr, A. R., Ediss, G. A., and Boyd, D. *ALMA Memo*, (377), 2001.
- [61] Kovac, J. M., Leitch, E. M., Pryke, C., et al. *Nature*, 420:772–787, 2002.
- [62] Kumar, C., Srinivasan, V. V., Lakshmeesha, V. K., and Pal, S. *IEEE Antennas and Wireless Propagation Letters*, 8:826–829, 2009.
- [63] Labay, V. A. and Bornemann, J. *IEEE Microwave and Guided Wave Letters*, 2(2):49–51, 1992.
- [64] Lah, P., Chengalur, J. M., Briggs, F. H., et al. *Monthly Notices of the Royal Astronomical Society*, 376(3):1357–1366, 2007.
- [65] Lawrence, C. R., Church, S., Gaier, T., et al. *WorkShop: Technology Development For A CMB Probe Of Inflation*, 2008.

- 
- [66] Leal-Sevillano, C. A., Cooper, K. B., Ruiz-Cruz, J. A., et al. *IEEE Transactions on Terahertz Science and Technology*, 3(5):574–583, 2013.
- [67] Leech, J., Tan, B. K., Yassin, G., et al. *IEEE Transactions on Terahertz Science and Technology*, 2(1):61–70, 2012.
- [68] Leitch, E. M., Kovac, J. M., Pryke, C., et al. *Nature*, 420:763–771, 2002.
- [69] Leong, Y. C. and Weinreb, S. *IEEE MTT-S International Microwave Symposium Digest*, 4:1435–1438, 1999.
- [70] Leppanen, K. J., Zensus, J. A., and Diamond, P. J. *The Astrophysical Journal*, 110(5):2749, 1995.
- [71] Li, E. S., Tong, G. X., and Niu, D. C. *IEEE Microwave and Wireless Components Letters*, 22(1):4–6, 2013.
- [72] Liu, A. S., Wu, R. B., and Lin, Y. C. *IEICE Transactions on Electronics*, E88-C(8):1764–1771, 2005.
- [73] Mennella, A., Bersanelli, M., Seiffert, M., et al. *A&A*, 410(3):1089–1100, 2003.
- [74] Molla, J., Ibarra, A., Margineda, J., et al. *IEEE Transactions on Instrumentation and Measurement*, 42(4):817–821, 1993.
- [75] Montgomery, J. P. *IEEE Transactions on Microwave Theory and Techniques*, 19(6):547–555, 1971.
- [76] Neininger, N., Guélin, M., Ungerechts, H., et al. *Nature*, 395:871–873, 1998.
- [77] Newburgh, L. *The Q-band Receiver Array Instrument and Observations*. PhD thesis, Columbia University, 2010.
- [78] O’Dea, D., Challinor, A., and Johnson, B. R. *Monthly Notices of the Royal Astronomical Society*, 376(4):1767–1783, 2007.

- 
- [79] Olver, A. D., Clarricoats, P. J. B., Kishk, A. A., and Shafai, L. *Microwave Horns and Feeds*. The Institution of Engineering and Technology, 1994. ISBN: 978-0-852-96809-3.
- [80] Padin, S., Staniszewski, S., Keisler, R., et al. *Appl. Opt.*, 47(24):4418–4428, 2008.
- [81] A. Pandey. Waveguide to microstrip line transitions for mm-wave applications. <https://anilkrpandey.wordpress.com/>.
- [82] Parma, V. Cryostat design. *arXiv:1501.07154*, 2013.
- [83] Parris, W. J. *Patent US3475757A*, 1966.
- [84] Patrick, M. K., Raffin, P., Huang, Y. D., et al. *Publications of the Astronomical Society of the Pacific*, 123(900):198–212, 2011.
- [85] Planck Collaboration, Ade, P. A. R., Aghanim, N., et al. *A&A*, 586(A141):1–17, 2016.
- [86] Planck Collaboration, Akrami, Y., Ashdown, M., et al. *A&A*, 641(A4):1–74, 2020.
- [87] Potter, P. D. *Microwave J.*, 6:71–78, 1963. or JPL technical report no.32-354.
- [88] Pozar, D. M. *Microwave engineering, 3rd ed.* Wiley, 2005. ISBN: 978-0-471-44878-5.
- [89] Pérez-Escudero, J. M., Torres-García, A. E., Ramón, G., and Ederra, I. *Electronics*, 7(10):215, 2018.
- [90] QUIET Collaboration, Bischoff, C., Brizius, A., Buder, I., et al. *The Astrophysical Journal*, 768(1):9, 2013.
- [91] Ragan, G. L. *Microwave Transmission Circuits, MIT Rad. lab. Series, vol.9.* McGraw Hill, 1948. chap.6, p.401-403.
- [92] Roshi, D. A., Shillue, W., Simon, B., et al. *The Astrophysical Journal*, 155(5):202, 2018.

- 
- [93] Runyan, M. C., Ade, P. A. R., Bhatia, R. S., et al. *The Astrophysical Journal Supplement Series*, 149(2):265–287, 2003.
- [94] Samoska, L. *IEEE Transactions on Terahertz Science and Technology*, 1(1):9–24, 2011.
- [95] Samoska, L., Deal, W. R., Chattopadhyay, G., et al. *IEEE Transactions on Microwave Theory and Techniques*, 56(6):1380–1388, 2008.
- [96] Schneider, M. V., Glance, B., and Bodtmann, W. F. *The Bell System Technical Journal*, 48(6):1703–1726, 1969.
- [97] Schrank, H. E. *IEEE Antennas and Propagation Society International Symposium*, 20:227–230, 1982.
- [98] Seljak, U. and Zaldarriaga, M. *Phys. Rev. Lett.*, 78(11):2054–2057, 1997.
- [99] Sieth, M., Devaraj, K., Voll, K., et al. *Proc. SPIE, Millimeter, Submillimeter, and Far-Infrared Detectors and Instrumentation for Astronomy VII*, 9153:219–230, 2014.
- [100] Simmons, A. J. *IRE Transactions on Microwave Theory and Techniques*, 3(6):18–21, 1955.
- [101] Siringo, G., Kreysa1, E., Kovács, A., et al. *A&A*, 497(3):945–962, 2009.
- [102] Snitzer, E. *Journal of the Optical Society of America*, 51(5):491–498, 1961.
- [103] Somasundaram, S., Pillai, A. M., Rajendra, A., and Sharma, A. K. *Journal of Alloys and Compounds*, 643:263–269, 2015.
- [104] Su, H. Y., Hu, R., and Wu, C. *IEEE Microwave and Wireless Components Letters*, 21(9):489–491, 2011.
- [105] Takashi, H., Masato, S., and Lin, Y. T. *Publications of the Astronomical Society of Japan*, 72(5):1–23, 2020.

- 
- [106] Teng, H. F., Wu, J. H., Li, H. H., et al. *Proc. SPIE, Millimeter, Submillimeter, and Far-Infrared Detectors and Instrumentation for Astronomy V*, 7741:774116–1–12, 2010.
- [107] Teng, S. F., Zhang, U. H., Chiueh, T. H., et al. *IEEE Transactions on Instrumentation and Measurement*, 64(2):299–307, 2015.
- [108] Thome, F., Leuther, A., Gallego, J. D., et al. *IEEE MTT-S International Microwave Symposium Digest*, pages 1495–1498, 2018.
- [109] Valenziano, L., Zannoni, M., Mariotti, S., et al. *Proc. SPIE, Millimeter, Submillimeter, and Far-Infrared Detectors and Instrumentation for Astronomy VII*, 9153:857–866, 2012.
- [110] Verheijen, M. A. W., Oosterloo, T. A., van Cappellen, W. A., et al. *AIP Conference Proceedings*, 1035:265–271, 2008.
- [111] Voll, P., Samoska, L., Church, S., et al. *International Journal of Microwave and Wireless Technologies*, 4(3):283–289, 2012.
- [112] Wang, L. and Steinhardt, P. L. *The Astrophysical Journal*, 508(2):483–490, 1998.
- [113] Weinreb, S., Lai, R., Erickson, N., et al. *IEEE MTT-S International Microwave Symposium Digest*, 1:101–104, 1999.
- [114] White, G. K. *Experimental techniques in low-temperature physics, 4th ed.* Oxford University Press, 1987. ISBN: 978-0-198-51428-2.
- [115] Wollack, E.J., Grammer, W., and Kingsley, J. *ALMA Memo*, (425), 2002.
- [116] Wong, S. K., Li, H. H., Shiao Jerry, Y. S., et al. *Proc. SPIE, Millimeter, Submillimeter, and Far-Infrared Detectors and Instrumentation for Astronomy V*, 7741:77412T–1–5, 2010.
- [117] Yagoubov, P., Mroczkowski, T., Belitsky, V., et al. *A&A*, 634(3):A46, 2020.

[118] Young, L. and Sobol, H. *Advances in Microwaves, Volume 8*. Academic Press, 1974. ISBN: 978-1-483-21557-0.

[119] Zaman, A. U., Vassilev, V., Zirath, H., and Rorsman, N. *IEEE Microwave and Wireless Components Letters*, 27(12):1098–1100, 2017.

